Dottorato di ricerca in Fisica XXXII Ciclo

Università degli studi di Messina

Dipartimento di Scienze Matematiche ed Informatiche, Scienze Fisiche e Scienze della Terra (MIFT)

Two-dimensional materials for energy storage and generation

Ph.D. Thesis

Valentino Romano

Ph.D. Coordinator

Professor Lorenzo Torrisi

Supervisor

Professor Giovanna D'Angelo

Co-Supervisors

Doctor Francesco Bonaccorso

Professor Giulia Grancini

Settore scientifico disciplinare: FIS/01

Anno accademico 2018-2019

I’ll tell you one thing I have learned:
I don’t think we figure out exactly who we are all at once,
I think it happens over a long period of time, just like piece by piece.
We go through this life slowly but surely,
just collecting these little pieces of ourselves that we can’t really live without
until, eventually, we have enough of them to where we feel whole.

This is us

ACKNOWLEDGEMENTS

From my experience, Ph.D. studies are, so far, the most challenging and intense. I think this is mainly due to the period of our lives involved during these three years, when we grow up and experience many changes as scientists and as human beings as well.

For these reasons, the first acknowledgements go to my parents, for their patience, guidance and endless support, and to all my family encouraging me from the very beginning. Many thanks to my friends and in particular to Alfo, Benny, Davide, Fede and Giusy for all the adventures, laughs, and help throughout these years (especially when I had to move from one city to another, always with some issues and strange things happening). A special thought goes to Giuseppe, the one with whom our Bachelor started in far 2011 and with whom I'm going to defend my Ph.D. thesis after 8 years. Thank you for being there as a colleague (during hours and hours of studying) and mostly as a trusted friend (always there during good and bad times).

When I think about how everything started, I always remember a simple question from my supervisor, Professor Giovanna D'Angelo: "Valentino, which project would you like to carry on during your Ph.D. studies?". My answer was "I would like to work on energy applications" and from the very beginning, she supported my choice and gave me all the help and possibilities she could give me. First of all, she asked to a previous student of the University of Messina, Doctor Francesco Bonaccorso, if he was interested in starting a collaboration with us. Doctor Bonaccorso, P.I. of the Graphene Labs of the Istituto Italiano di Tecnologia (IIT, Genova, Italy), accepted the proposal and the adventure started. In IIT I worked on the production and use of 2D materials (like graphene and transition metal dichalcogenides) mainly in energy storage applications (supercapacitors) and even in electrocatalysis. Then it was the time to fulfil one of the compulsory requirements of my Ph.D. (funded by the *Fondo Sociale Europeo*): spending 6 months of my studies abroad. The opportunity came thanks to Professor Giulia Grancini (Università di Pavia, Italy), that I met at IIT while she was delivering a talk on perovskite solar cells. At that time, Professor Grancini was working at the group of Professor Mohammad Khaja Nazeeruddin: Group for Molecular Engineering of Functional Materials, École Polytechnique Fédérale de Lausanne (EPFL, Sion, Switzerland). Thanks to Professor D'Angelo, Doctor Bonaccorso, Professor Grancini and Professor Nazeeruddin, we started a joint collaboration that gave me the amazing opportunity to study at EPFL, from January 2019 until July 2019. The projects we carried out (and that we are currently finalising) concern the use of 2D materials in perovskite solar cells.

This rather short story involved so many people to whom I owe everything I learned and did in these years.

First of all, I have no words to thank Professor D’Angelo for the endless trust and encouragement that she gave to a very young, inexperienced student that had a small dream that she started to turn in reality. All began thanks to you and I will always remember this. I hope that, one day, I will be able to be for someone the kind of supervisor you have been with me. Many thanks to Professor Giuseppe Carini (my supervisor during my Bachelor and Master degrees), for his wisdom and guidance since my 3rd year of studies, and to Professor Caterina Branca, Doctor Mauro Federico and Emanuele Cosio, the members of our group with whom we are sharing these years of scientific and funny moments.

Many (endless) gratitude goes to my co-supervisors Doctor Bonaccorso and Professor Grancini, for accepting me as their “co”-student and giving me the possibility to work with such huge and important institutions as IIT and EPFL. Special thanks go to Professor Nazeeruddin that accepted me as guest Ph.D. student in his group and for involving me in all the group activities, making me feel like a real member of his laboratory.

Acknowledgments IIT:

My deepest thanks go to Sebastiano Bellani that was (is, and probably will always be) the one teaching, encouraging, helping and motivating me to do my best and work hard.

Thanks to Beatriz Martin-Garcia and Leyla Najafi for being my always-present teachers in the laboratory: from 2D materials production to the assembly of supercapacitors, from electrochemical characterizations to solar cells preparation, your support and motivation were and are special!

Special thanks to Graphene Labs technicians: the amazing Elisa Mantero, Luigi Marasco, Manuel Crugliano and Luca Gagliani. Thank you for always being there making Graphene Labs safe, for teaching me how to handle many experimental techniques, how to improve security in the laboratory and most importantly for your friendship, support and encouragement.

Thanks to all my IIT friends: Antonio Esau, Luca, Reinier, Mohammad, Stefano, Lorenzo, Eleonora, Laura, Arcangelo, Silvia, Sara, Gabriele, Marilena, Nicola, Michele, Alberto, Panda and Sanjay for all the funny moments, scientific discussions and friendships that we shared.

Acknowledgments EPFL:

My first thanks go to the teachers that became my very good friends: Inés and Albert. Thank you for repeating me the same things 4, 5 times until I finally could do it, thank you for sharing with me your "magic", coming with me at the very far away supermarket, providing me with (dirty) magnetic stirrers, purple gloves and thin lab coats. I will always remember the amazing time we spent together and I am sure we will have more ahead of us.

Many thanks to my office-mates and friends Cansu (olmadi), Hobeom (sanzeighim), Nikita (sciroppo) for our valid scientific discussions (about food, languages, strange songs and creepy waitress). Thanks to Cristina Momblona and Cristina Roldan for all their advices and supporting words. Thanks to Javier for teaching me all the very broad Spanish vocabulary that I know. Thanks to Martina and Nadja for all the laughs and funny moments spent together. Thanks to Geraldine for helping me throughout all the administrative part of my stay in EPFL. Thanks to all the other colleagues in EPFL: Valentin, Aron, Hiroyuki, Paek, Xiaoxin, Ruiyuan, Alex, Mousa, Sijo, Vaida, Yi and Riujy for all the scientific and funny moments that we shared.

In the end, I can say that these three years gave me the opportunity to meet and work with many people and friends, that helped me in finding some important pieces of my puzzle. Now I feel more complete, but there is still a lot to do (both professionally and personally) and the end of this journey is just the beginning of a new one.

Thank you

PREFACE

Energy is probably the most important factor influencing our everyday life. In fact, we need energy to power up our houses, vehicles, buildings and electronic devices. Storage and generation are the fundamental factors that influence the ways energy can be deployed and produced, so careful strategies have to be designed for their optimization. In particular, the materials used for these technologies should be earth abundant, environmental friendly and cheap. All these requirements are met by two-dimensional (2D) materials (*i.e.*, graphene, transition metal dichalcogenides, *etc.*), that are currently representing a viable solution to the energy management. In this context, the research works presented in this thesis concern the use of 2D materials in both energy storage and generation devices.

In particular, the thesis is organized as follows:

Chapter 1 describes the discovery, properties, production and some applications of 2D materials (in particular graphene and transition metal dichalcogenides).

Chapter 2 concerns the use of 2D materials in energy storage applications, specifically in electrochemical double layer capacitors. The working principle and main properties of this kind of devices will be thoroughly introduced. Herein, two projects are reported concerning the use of graphene flakes (produced through a wet-jet milling system) as active material for the fabrication of electrodes for electrochemical double layer capacitors. The first project is about the physico-chemical effects raising from the flow of the electrolyte ions on the graphene flakes surface. Our results show that graphene flakes act as “ion sliding” surfaces for the electrolyte ions. The second project, presented in this chapter, shows that the graphene flakes produced by wet-jet milling can be used for the design of high-areal performance electrodes for flexible supercapacitors. These projects are the results of a collaboration with Doctor Francesco Bonaccorso (Istituto Italiano di Tecnologia, Genova, Italy).

Chapter 3 deals with energy generation devices, specifically perovskite solar cells. Perovskite materials are now at the centre of huge research efforts for their application in photovoltaics. In this chapter, the main properties of perovskite materials, their use in solar cells and the limits of the resulting devices will be discussed. Finally, the preliminary results on the use of transition metal dichalcogenides flakes in low-dimensional perovskite solar cells will be reported. The aim of this study is to improve the charge collection and the stability of perovskite-based devices. The reported works are carried out in collaboration with Doctor Francesco Bonaccorso (Istituto Italiano di Tecnologia, Genova, Italy), Professor Mohammad Khaja Nazeeruddin (École Polytechnique Fédérale de Lausanne, Sion, Valais) and Professor Giulia Grancini (Università di Pavia, Italy)

THE LIBRARY OF TWO DIMENSIONAL MATERIALS

INTRODUCTION

Nanoscience and Nanotechnology deal with the synthesis, the characterization and the applications of materials having at least one dimension in the nano-metre scale. From this point of view, materials can be classified in 3, 2, 1 and 0 dimensional (D), where the number indicates the dimensions left in the macro-scale (**figure 1**). The interest in nanotechnology raised because it allows the manipulation of matter at an atomic and molecular level. This “engineering” procedure leads to peculiar properties (like enhanced strength, control of absorption spectra and chemical reactivity) that can be exploited in a plethora of applications ranging from electronics, photonics, automotive industry, biophysics, drug delivery and so on. Among all known materials, the case of carbon is particularly intriguing with graphite (3D), graphene (2D), carbon nanotubes (1D) and fullerenes (0D) being the known dimensional forms of carbon (**figure 1**).[1,2] Until 1991, the experimentally isolated forms of carbon were graphite, carbon nanotubes and fullerenes: graphene (as given by a single layer of graphite) was observed already in the 1970’s, but only preliminary and qualitative studies were reported (*i.e.,* none highlighted the peculiar properties of graphene or provided a clear way for its experimental isolation).[3] Finally, in 2004 at the University of Manchester, Andre Geim, Konstantin Novoselov and co-workers isolated for the first time graphene and conducted the first pioneering studies on it.[4]

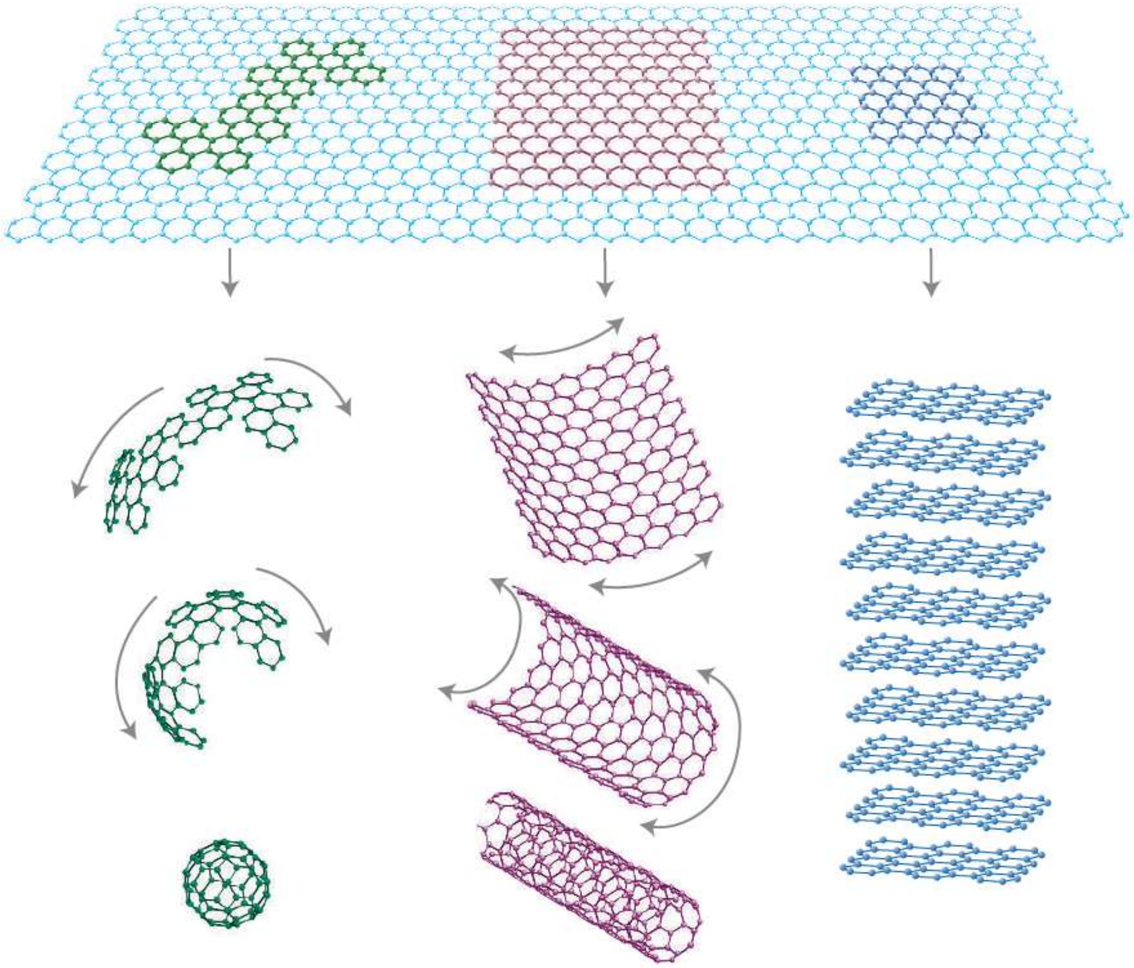

Figure 1: Graphene as the fundamental carbon building block. All the different dimensional forms of graphite can be formed by using as starting material a graphene layer. From left to right: fullerene (0D), carbon nanotube (1D) and graphite (3) (taken from ref.[1]).

For these efforts, Geim and Novoselov were awarded the 2010 Nobel prize in Physics, paving the way for the rise of 2D materials. In fact, after graphene, many other 2D materials were discovered, each with its own peculiar properties. In principle, all the materials that are characterised by strong intra-layer and weak inter-layer bonds can be produced in 2D form by peeling off these planes.[5–7] However, very recently it has been shown that even non-layered materials (*e.g.* galena, goethite and calcite) can be exfoliated in their 2D counterparts, opening a new and intriguing scenario in the science of 2D materials.[8]

In this chapter, a brief description of the most studied 2D materials will be presented, describing their optoelectronic properties, production processes and applications.

TWO DIMENSIONAL MATERIALS LIBRARY

GRAPHENE

The word *graphene* refers explicitly to sp^2 hybridized carbon atoms forming a honey-comb single layer structure (**figure 2a**). However, this term is commonly used to even denote few and multi-layers graphitic arrangements. The huge interest in this material raised mainly because of its physical properties: in a perfect graphene sheet, the interaction between the electrons and the periodic honey-comb potential gives rise to an effective Hamiltonian (for the π electrons, around the K and K' points of the graphene reciprocal lattice (**figure 2b**)) described by the Dirac equation rather than the Schrödinger equation.[1,9,10] This results in a linear dispersion relation for the electrons around K and K', where the conduction and valence bands touch in one single point called Dirac point (**figure 2c**).[1,9–11] The graphene dispersion relation is responsible for many intriguing physical properties, including half-integer quantum Hall effect, Berry's phase and Klein paradox.[1,11,12]

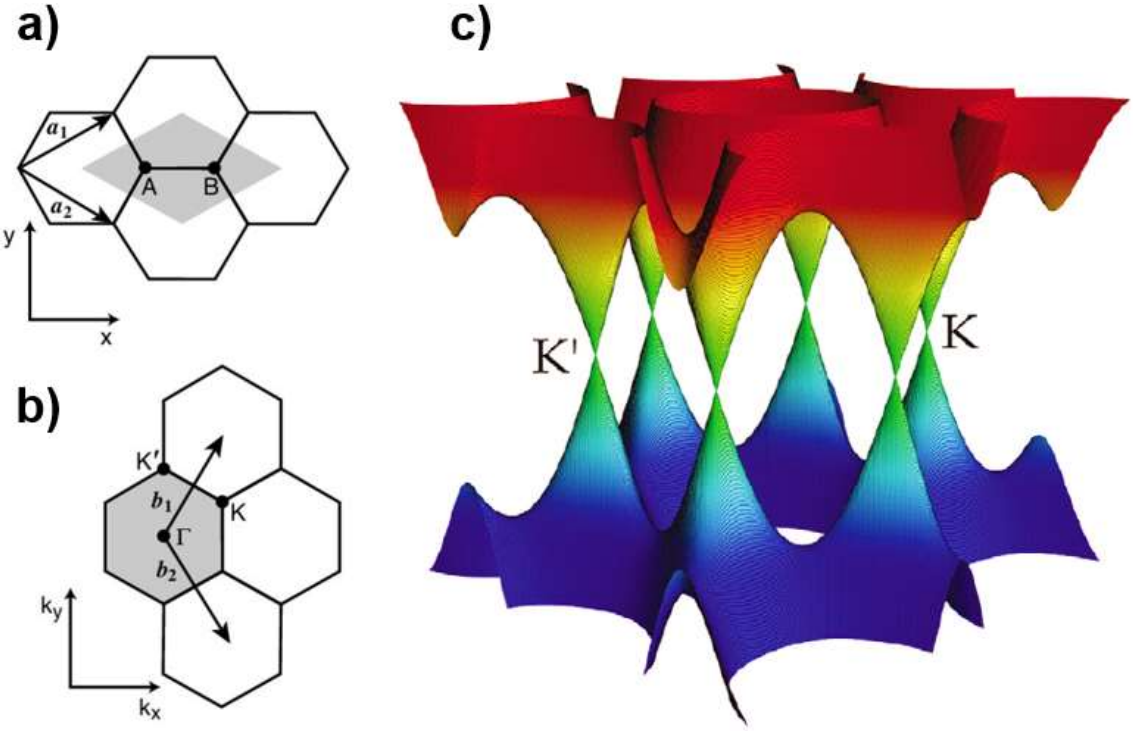

Figure 2: Graphene lattice properties and band structure. (a) Real and (b) reciprocal space structure of graphene. The grey shaded areas indicate the unit cells, a_i and b_i refer to the basis vectors of real and reciprocal space respectively. (c) Band structure of graphene where the insurgence of Dirac points is shown (figure (a)) and (b) are adapted from ref.[13] while (c) is taken from ref.[11]).

Therefore, graphene represents an exceptional experimental tool to probe and study quantum electrodynamics phenomena that have never been observed even in the realm of particle physics: “quantum electrodynamics in a pencil trace”, as stated by Geim and Novoselov.[1,10]

The electronic band structure of graphene leads to an electron mobility as high as 1.5 x 10^4 cm^2 V^{-1} s^{-1} at room temperature (with a temperature independent behaviour between 10 and 100 K).[14–17] Moreover, graphene has a distinctive optical transparency of 97.7% to visible light, exhibiting a linear optical response below a non-linear threshold.[18–20] Graphene also shows a thermal conductivity ranging from 4.84 to 5.3 x 10^3 W m K^{-1} at room temperature (measured by Raman spectroscopy)[21] and 600 W m K^{-1} when measured on suspended flakes, deposited on SiO_2 substrates.[22] These values exceed those of several metals, including copper (Cu).[22] Additionally, graphene exhibits peculiar mechanical properties. On one hand it has Young modulus as high as 1060 GPa and a breaking strength up to 42 N m^{-1}, making graphene stronger than steel.[23,24] At the same time, graphene has an elastic limit of ~ 20%, making it a suitable material for the production of flexible devices.[25,26] Lastly, in ambient conditions graphene is not permeable to any atom, including hydrogen,[27] although thermal protons can pass through it[28] leading to promising applications of graphene-based membranes in hydrogen fuel cells.[28] It is worth noting that graphene's properties can be changed by chemical functionalization, including oxidation and fluorination.[29,30]

For all these reasons, graphene is an optimal candidate for many applications such as photonics,[31,32] energy generation and storage,[33–35] thermal control,[36,37] functional materials,[38] bio-applications[39,40] and many others.[26] However, the lack of an energy bandgap hinders the use of graphene in some electronic applications (*e.g.*, field effect transistors).[41–43] This shortcoming raised the interest for the search of semiconducting 2D materials: a promising solution came with transition metal dichalcogenides (TMDCs), a group of materials showing different electronic properties (*i.e.*, metallic, semiconducting and insulating) according to their chemical composition.

TRANSITION METAL DICHALCOGENIDES

The TMDCs library consists of materials with chemical formula MX_2, where M is a transition metal atom (*e.g.*, Mo, W, Ta, Nb, *etc.*) and X is a chalcogen atom (*i.e.*, S, Se or Te).[5]

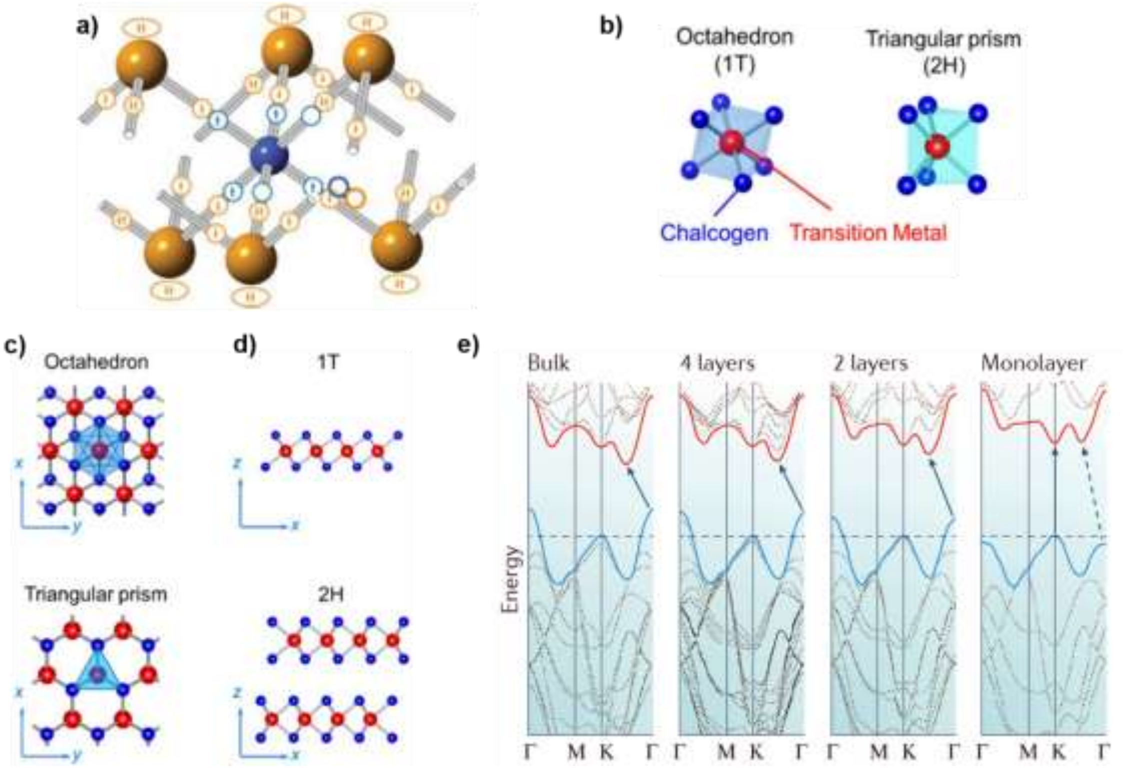

Figure 3: Structural and electronic properties of TMDCs. (a) Structure of a single TMDC layer: the transition metal atom and its electrons are indicated in blue; the chalcogen atoms and their respective electrons are depicted in orange. Single arrows refer to one electron shared in covalent bond, while the double arrows are used for a couple of electrons forming dative bonds. Finally, non-bonding full orbitals are shown with an oval while vacant orbitals are depicted with empty circles. (b) Octahedral (1T) and triangular (2H) prismatic structures of TMDCs. (c) Top and (d) side views of 1T and 2H phases. (e) Band structure calculations of 2H-MoS_2 as a function of number of layers. (figure (a) is taken from ref.[5], figures (b), (c) and (d) are adapted from ref.[44]; figure (e) is taken from ref.[45])

The transition metal provides 4 half-filled and 2 empty orbitals. The covalent and dative bonds that are formed between the metal and the 6 chalcogenide atoms give rise to the arrangement reported in **figure 3a**.[5] In this structure, one TMDC single layer is made up by a plane of metal atoms sandwiched between two planes of chalcogenide atoms. The non-bonding lone pairs at the outer regions of the chalcogenide planes are responsible for the Van der Waals interactions that hold weakly adjacent layers. For this reason, TMDCs can be easily exfoliated in their 2D form.[5]

The structure of 2D TMDCs results from the coordination of the transition metal atom. The most common phases are 2H (referred to 1H in single layer TMDCs) and 1T, corresponding to triangular prismatic and octahedral coordination of the transition metal (as shown in **figure 3b-d**).[5,45,46] In the notation 2H and 1T, the number indicates the number of layers contained in the unit cell while the letter denotes the hexagonal (H) and trigonal (T) symmetries.[5,45,46]

The electronic properties of TMDCs depend on the progressive filling of their orbitals, giving rise to a very broad range of opto-electronic behaviours: insulators (*i.e.*, HfS_2), semiconductors (*i.e.*, MoS_2, WS_2), semimetals (*i.e.*, WTe_2, $TiSe_2$) and metals (*i.e.*, NbS_2, VSe_2).[5,45,46]

Among all TMDCs, those formed by group-VI transition metals (*i.e.*, MoS_2, $MoSe_2$, WS_2 and WSe_2) have attracted huge interest for electronic devices because of both their charge carrier mobilities and bandgaps (ranging from the near-infrared to the visible electromagnetic spectrum).[47–49] Large on/off switching ratios in field effect transistors have been achieved, offering the promises for overcoming the limitations from Si-based technologies shrinking (gate length limit in Si: ~5 nm; gate length achieved in MoS_2: ~1 nm).[50] Moreover, group-VI TMDCs show an evolution of their band structures with the number of layers. For example, MoS_2 (*i.e.*, the most investigated TMDCs) shows an indirect-to-direct optical band gap transition (from 0.88 eV for the bulk case to 1.71 eV for the monolayer material) (**figure 3e**).[45,46]

Another peculiar feature of group-VI TMDCs is that their Brillouin zone shows two or more degenerate inequivalent valleys (*i.e.*, local minimum in the conduction band or local maximum in the valence band).[41] Consequently, electrons are characterised not only by charge and spin, but even by a valley degree of freedom that specifies the valley they are occupying.[41] As a consequence, the manipulation of the valley number can be used to store and carry information, in the same way as electronics and spintronics do by exploiting charge and spin respectively: this idea led to the rise of valleytronics.[41,45,46]

Finally, several bulk TMDCs exhibit intriguing low temperature phenomena, such as the insurgence of charge density wave phases (TaS_2, $TaSe_2$ and $NbSe_2$) and superconductivity (NbS_2 and TiSe2).[5,45,46] In 2D TMDCs charge density waves were observed experimentally in monolayer $NbSe_2$[51,52] and TaS_2[53] while superconductivity was detected only in monolayer $NbSe_2$[52] .

OTHER 2D MATERIALS EXAMPLES

Graphene and TMDCs are just few examples of the plethora of existing 2D materials. In fact, all the layered materials (*i.e.*, solids that are characterised by strong in-plane bonds and weak out-of-plane bonds) can be exfoliated and stabilized in their 2D counterparts by providing the energy needed to break the inter-plane bonds.[7] Graphene, silicene, germanene and black phosphorus are examples of one single atom thick 2D materials of carbon, silicon, germanium and phosphorous respectively.[54,55] Hexagonal boron nitride (h-BN) belongs to same family of atomically thin 2D materials, but in this case there are two different kind of atoms in one single plane (boron and nitrogen).[56] The case of TMDCs can be classified together with transition metal halides (such as PbI_2 and $MgBr_2$),[57] since in both cases their 2D arrangements consist of one plane of transition metal atoms sandwiched between two planes of chalcogenides or halides.[7] Other layered materials are some metal oxides (*e.g.*, MnO_2, MoO_3 and $LaNbO_7$),[58] double hydroxides (*e.g.*, $Mg_6Al_2(OH)_{16}$),[58] layered III-

VIs monochalcogenides (*e.g.*, InSe and GaS),[59] metal trichalcogenides (*e.g.*, $TiTe_3$ and NbS_3),[60] metal trihalides (*e.g.*, $CrCl_3$ and BiI_3)[61] and transition metal carbides and carbonitrides (so called MXenes, *e.g.*, Ti_2AlC, Ti_3CN and Ta_4AlC_3).[62] The 2D materials typically show peculiar physico-chemical properties that are different from those expressed in the bulk parents, making the 2D materials library a formidable platform to carry out fundamental studies and implement novel applications.

MATERIALS PRODUCTION METHODS

In the previous section it has been shown that the physico-chemical properties of 2D materials make them promising candidates for both fundamental and applicative studies. In either cases, samples must be prepared by choosing procedures satisfying the requirements of the field of interest. The processes used for the production of 2D materials are divided in two categories: top-down and bottom-up (**figure 4** shows the most popular among them). As concerns top-down approaches, nanostructures are produced by reducing the size of a large sample. Examples of top-down techniques are exfoliation techniques (such as micromechanical cleavage and liquid phase exfoliation), laser ablation and lithography. On the other hand, bottom-up approaches create nanostructures by exploiting physical or chemical processes that lead to aggregation of atomic or molecular precursors in nanostructures. Chemical vapour deposition, growth on SiC and molecular beam epitaxy are typical bottom-up procedures. In these sections, some of these production processes will be discussed, emphasising pros and cons.

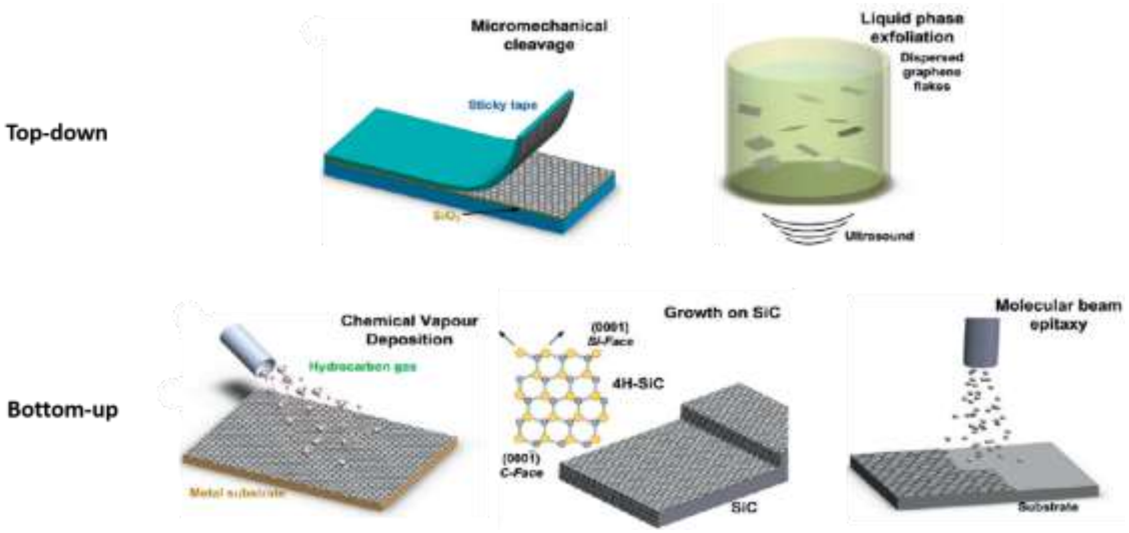

Figure 4: Illustrative representation of some production procedures used for 2D materials. Top-down (micromechanical cleavage, liquid phase exfoliation) and bottom-up (chemical vapour deposition, growth on SiC, molecular beam epitaxy). (adapted from ref.[63])

CHEMICAL VAPOR DEPOSITION

The term chemical vapour deposition (CVD) refers to all those techniques that allow thin films of a material to be formed on a heated substrate, by exploiting chemical reactions between gaseous precursors.[64] Indeed, there is a variety of CVD processes depending on the precursors/substrates features, cost and quality, as well as the thickness of the resulting film: hot wall CVD, plasma-based CVD (*e.g.*, microwave plasma-assisted CVD or plasma-enhanced CVD), atomic layer CVD, *etc*.[63,64] The key advantage of the CVD techniques is that they are suitable for the deposition of almost all the elements of the periodic table and many compounds, as films can be prepared by using temperatures far lower than their corresponding sublimation temperature (as in the case of SiC that sublimates at 2700 °C, but can be prepared at 1000 °C through the reaction between H_2 and CH_3SiCl_3).[64] However, major drawbacks of this approach regard the cost and especially the health hazards of precursors, intermediates and by-products resulting from the chemical reactions.[63,64]

Regarding the specific case of graphene, the first large area (~cm^2) CVD graphene film was successfully grown on a metal surface (Cu) in 2009 (at a temperature of 1000°C).[65] Some years later it was shown that graphene could be grown on nickel too at temperatures lower than those used to the copper substrate (~550°C).[66] However, there are many issues that need to be assessed. First of all, the roughness of the metal substrates leads to variations in the graphene film thickness and in the coating uniformity throughout the whole surface.[67,68] Moreover, many electronic applications require the growth of materials on top of insulating surfaces rather than metallic ones.[63] Promising results have been achieved by using as substrates sapphire,[69] hexagonal boron-nitride[70] and glass[71] but researches are still ongoing to increase the surface coverage. This means that graphene needs to be transferred from one substrate to another,[72] with a reliable and cheap procedure that avoids structural damages and contaminations.[73] Currently some companies provide CVD-graphene deposited on different kind of substrates with variable sizes (*Graphene Square*: 8x8 cm^2 on Cu and then transferred on SiO_2/Si wafer, 100x100 cm^2 on polyethylene terephthalate (PET); *Chongqing Graphene Technology*: annual production of 1000000 m^2 on Cu foil or PET with sizes up to 300x30 cm^2; Graphenea: annual production of 7000 wafers with wafer sizes up to 8 inches), paving the way through the large scale industrialization of CVD grown graphene.[74]

GROWTH ON SiC

The major shortcoming concerning the CVD growth of 2D materials, *i.e.*, deposition on metal substrates and consequent need for a transfer process, can be avoided by exploiting growth on SiC by thermal decomposition (typically known as epitaxial growth).[63,75] This method is based on the annealing of SiC substrates at a temperature >1400°C to induce the evaporation of Si and the rearrangement of the left C network (vapour pressure of C is much lower than that of Si, so only Si atoms are evaporated).[75,76] The carbon film left on the substrate rearranges forming a graphitic lattice made up by small grains (30-200 nm), having different thickness throughout the film surface,[63,75,77] depending on the morphological distortion induced by the sublimation of Si atoms, as well as the lattice mismatch between SiC (3.073 Å) and graphene (2.46 Å). In order to control the resulting graphitic lattice, many approaches have been proposed in the past years, ranging from annealing of the SiC substrates in argon atmosphere (to reduce the Si sublimation rate),[77] confined controlled sublimation of Si from SiC (which allows to regulate the graphene growth)[76] and annealing of SiC in an external Si flux (consenting the control of the Si vapour pressure).[78] Meanwhile, alternative substrates to SiC have been proposed to reduce the lattice mismatch between SiC and graphene. For example, h-BN[79] and hexagonal closed packed Co[80] have been successfully exploited, since for these cases the lattice mismatches are ~1.7% and ~2% respectively.[63] However up to date, SiC technology is preferred since this is an established substrate for many applications such as high frequency electronics, light emitting and radiation devices.[63] The major drawbacks regarding growth on SiC concern the high cost (~130€ for 2'' vs 4€ for the same Si wafer size),[63] small size of SiC wafers with respect to Si and the limited dimension of the graphene grains (up to now, no larger than 50x50 μm^2).[75]

EXFOLIATION TECHNIQUES

Among the top-down approaches, exfoliation techniques of layered crystals are the most used, since some of these methods allow a large-scale production of 2D materials. The basic idea is that layered crystals can be peeled in single-/few-layers by overcoming the Van der Walls interactions between adjacent planes.[6,81] This process can be performed by applying both normal and shear forces to the pristine materials (**figure 5a**): the first scenario pertains micromechanical cleavage and sonication-assisted liquid phase exfoliation, while the second condition is typical of ball milling and fluid dynamics-based systems.[81,82]

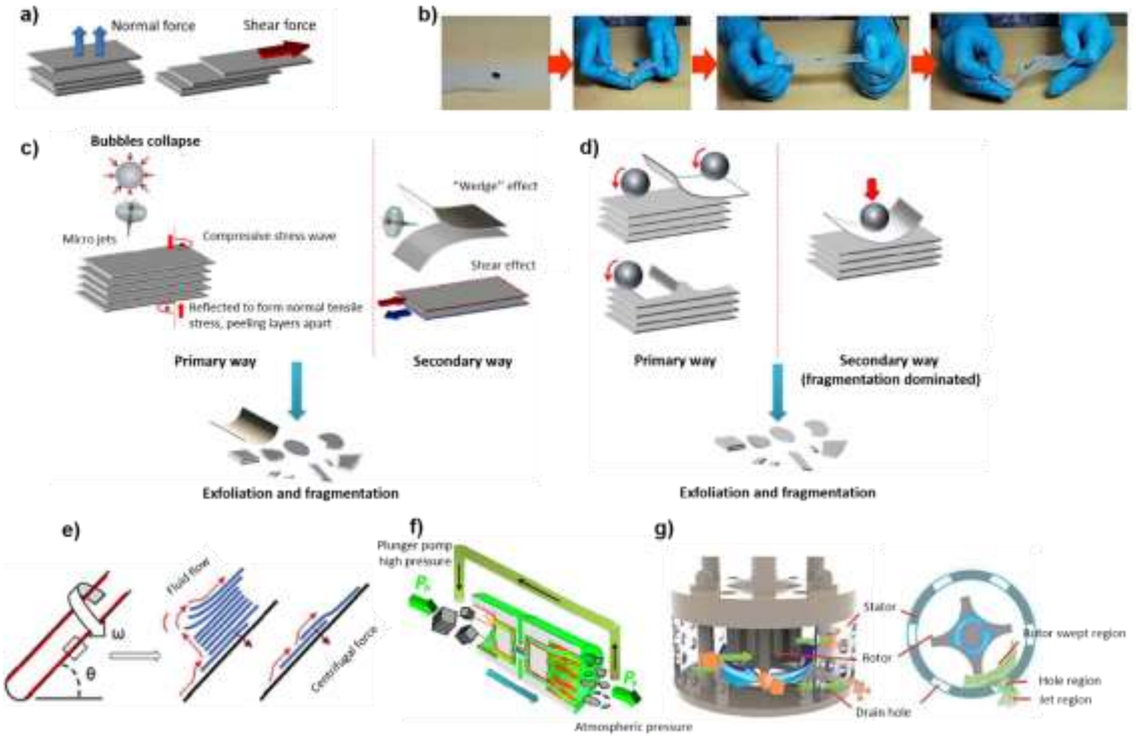

Figure 5: Illustrative representation of some exfoliation techniques for 2D materials. (a) Normal and shear forces responsible for the exfoliation. (b) Illustrative procedure of scotch-tape micromechanical cleavage. (c, d) Sketch of the processes occurring during liquid phase (c) and ball milling (d) exfoliation. (e-g) Schematic representation of vortex fluid (e), pressure driven (f) and mixer driven (g) exfoliation. (adapted from ref.[81])

MICROMECHANICAL EXFOLIATION

In micromechanical exfoliation (**figure 5b**), 2D materials flakes of variable thickness are peeled off from their native bulk crystals by using a cleaving agent. Scotch tape is the most common cleaving agent, but adhesive polymers can be used as well.[81] Micromechanical exfoliation has been used since the 1960s, when Robert Frindt conducted pioneering works on the isolation of thin films of TMDCs.[83] However, the technology available at that time could not provide accurate instruments for the thorough characterization of such kind of materials so the interest in this topic eventually faded. It is worthy of note that the isolation of the first "real" 2D material (*i.e.,* made up by *one* single layer) has been achieved thanks to this rather simple technique, by the group of Andre Geim in 2004.[4] By using scotch tape, they cleaved graphene from highly oriented pyrolytic graphite. This exfoliation process exerts a normal force on the graphite surface that leads to the separation of few-layers graphitic flakes (also referred as few-layers graphene) and, by repeating this procedure, it is eventually possible to isolate graphene. At that time (after almost 50 years from Frindt's work), the technological improvements, *e.g.*, in particular the development of scanning probe microscopies, paved the way for the first studies on graphene, leading to the rise of the 2D materials era. Careful and proper use of micromechanical exfoliation produces high-quality graphene, suitable for fundamental studies and the fabrication of small devices.[6,63] However, this process is not scalable so it still remains one of the first choice for research purposes, but not for large-scale applications.

LIQUID PHASE EXFOLIATION

In 2008 the group of Jonathan Coleman reported for the first time the exfoliation of graphite in liquid solvents, by using ultrasounds.[84] This technique, nowadays known as liquid phase exfoliation (LPE), exploits cavitation-induced bubbles to peel off crystalline layers from a bulk sample.[6,81] When a bubble collapses, a compressive shock wave propagates perpendicular to the layers and induces the exfoliation of the bulk material in a mixture of single-/few-layers (SL/FL) flakes. Some of these shock waves can even induce shear stresses, but the main mechanism for the exfoliation remains the orthogonal process (**figure 5c**).[81] There are many advantages in using LPE, the main one being the possibility to produce and process SL/FL flakes in the liquid phase to obtain functional inks compatible with solution-processed depositions[6] (*e.g*., spray-coating[85], vacuum filtration[86], ink-jet printing[87,88] and drop-casting[89]) for a variety of applications ranging from energy storage and generation to thermal management.[26] However, although LPE allows the production of 2D materials to be scaled-up, there are many major issues that need to be assessed.[74,81] First of all, stable dispersions can be prepared only if the exfoliated material and the liquid solvent have similar surface energies. For the case of graphene, the suitable surface energies range between 70/80 mJ m^{-2}, leading usually to the use of high boiling point, toxic organic solvents (like N,N-dimethylformamide – DMF – and N-methyl-2-pyrrolidone – NMP).[6,81] Moreover, in LPE the resulting dispersion is made up by SL/FL flakes, which means that the morphology (*i.e.*, the thickness and the lateral size of the flakes) is not homogeneous.[6] The sorting of 2D materials flakes is usually performed by means of an ultracentrifugation step in a uniform or density gradient medium.[6] The first method is referred sedimentation based separation (SBS) and is the most used and common strategy for the sorting of 2D materials.[6] In SBS, nanomaterials are separated according to the difference of their sedimentation rate, arising as a result of a centrifugal force acting on them.[90] For the case of a 2D materials dispersion subjected to ultracentrifugation, the sum of the moduli of all the forces acting on the flakes is given by[90]:

$$\mathrm{F_{tot} = F_c - F_b - F_f = m_{2D}\omega^2 r - m_s\omega^2 r - fv} \qquad (1)$$

Where F_c is the centrifugal force (which is proportional to the mass of the 2D flakes m_{2D}, the square of the angular velocity ω and the distance from the rotational axes r), F_b is the buoyant force (related to Archimede's principle, this contribution is proportional to the mass of the displaced solvent m_s and the centrifugal acceleration) and F_f is the frictional force (depending on the velocity of motion of the flakes in the solvent v and the frictional coefficient f between the solvent and the flakes). From this equation, at the equilibrium condition (dv/dt = 0), it can be demonstrated that the sedimentation rate of 2D flakes dispersed in a solvent with homogeneous density is governed by the Svedberg equation:[6,90]

$$\mathrm{s} = \frac{\mathrm{m_{2D}}\left(1 - \frac{\rho_S}{\rho_{2D}}\right)}{\mathrm{f}} \qquad (2)$$

Where ρ_s and ρ_{s2D} are the densities of the solvent and 2D materials respectively, while s is the sedimentation coefficient (which indicates the time needed for the sedimentation of the flakes and is measured in Svedberg – S – where 1S = 10^{-13} s). It is worth emphasising that f is a parameter depending on the morphology of the considered nanomaterial: in general, spherical objects have low f values compared to large and extended ones.[90] Since s depends on both f

and m_{2D}, thick, large and heavy flakes sediment faster with respect to thin, small and light flakes allowing the separation of the 2D materials dispersion according to their morphology.[6] The SBS method has been extensively used for the preparation of graphene[84,91] and other 2D materials[92–94] dispersions with flakes whose dimensions range from few nanometers to few microns.

BALL MILLING

Shear force induced exfoliation is performed, for example, by ball milling.[81] This system is based on the use of a rotating hollow cylinder which is partially filled with abrasion-resistant balls. For this technique, materials are exfoliated and fragmented by means of shear forces arising from the sliding of the balls on the materials surfaces (**figure 5d**), but vertical collisions can occur too, leading to fragmentation of the flakes and the formation of defects in the basal planes. These issues hinder the widespread of ball milling production, but it remains the first choice for the preparation of some composite materials like graphene-sulphur.[81]

FLUID DYNAMICS

In LPE, the cavitation phenomenon depends on the vessel size and the position of the ultrasounds source, leading to a “static exfoliation” that results in partial exfoliation of the dispersed flakes.[95] For these reasons, the need for a more efficient procedure raised, leading to the so-called fluid dynamics-based techniques. In these cases, the exfoliation is caused by different fluid dynamics phenomena, depending on the considered procedure, the main ones being vortex fluidics, pressure and mixer driven fluid dynamics.[95] The common idea is that pristine flakes (for example graphite flakes) move with the liquid and consequently can be exfoliated many times in different positions.[95]

For the vortex fluidic film case, pristine flakes are dispersed in a solvent inside a high-speed rotating tube (**figure 5e**). The exfoliation occurs because the graphite flakes experience lift and slippage forces that shift and take apart the crystalline layers.[95] The major drawback of this technique is that the exfoliation is limited on the edge-adhering dispersion layer, so the whole process is time consuming and yields only small dispersion volumes.[95]

On the other hand, large-scale production of 2D materials can be achieved thanks to pressure-driven fluid dynamics. In this case, the exfoliation is caused by both normal and shear forces, induced by many fluid dynamics phenomena, that occur when the liquid dispersion passes through micro- or milli-meter size channels (**figure 5f**).[95,96] Normal stresses are due to cavitation and pressure release phenomena, while shear forces are caused by velocity gradient and turbulence.[81,95,96] Many studies have shown that the morphology of the produced 2D materials flakes can be tuned by proper choice of pressure and treatment time, allowing the production of good to high quality materials with high concentrations (~10 g L^{-1}).[96–98]

Finally, in 2014 the group of Jonathan Coleman showed that scalable exfoliation of layered crystals can be also achieved by using the so-called mixer-driven fluid dynamics method (**figure 5g**).[99] More in detail, they used a shear mixer made up by closely spaced rotor/stator and managed to exfoliate graphite in NMP. Moreover, they realised that the exfoliation can be achieved even in the absence of turbulent flow (*i.e.*, Reynolds numbers $<10^4$), by adjusting the rotor diameter.[99] The same year, Liu *et al.* qualitatively showed that the exfoliation is caused by shear forces, cavitation and collision effects occurring in proximity of the stator/rotor.[100] It was even shown by Yi *et al.*[101] and Varrla *et al.*[102] that a kitchen blender is a surprisingly good tool for the exfoliation of layered crystals (due to velocity fluctuations and consequent turbulent flow).[103] Mixer driven fluid dynamics is a promising technique through large scale production of 2D materials (by simply using industrial revolving wheels) for many applications, including biology since it was shown that graphene can be exfoliated in bovine serum aqueous solutions.[104]

APPLICATIONS OF 2D MATERIALS

Two dimensional materials are attracting huge interest not only for the understanding of their peculiar physico-chemical properties, but also for their use in practical applications. In fact, as discussed in the previous sections, 2D materials can be produced by using many different techniques (some of them being cost-effective) using earth-abundant and environmental friendly precursors (especially for the case of top-down approaches).[74] However, the 2D nature of these materials, inevitably leads to non-ideal behaviour due to the presence of scattering sources, disorder and trap states.[45] These effects can be minimised by tuning the 2D materials properties thanks to many procedures such as chemical functionalization,[29,30] or doping/strain/interface engineering.[45]

For example, the encapsulation of MoS_2 in HfO_2 led to the first demonstration of a 2D TMDCs-based transistor.[105] Although the resulting performances are still lower than those of commercially available devices, this research area still remains a hot topic because of the mechanical properties of TMDCs that can lead to the fabrication of flexible transistors.[45] Furthermore, the high strength of TMDCs (breaking strength ~10%)[106] allows the use of strain to induce changes in the materials properties. For example, theoretical studies suggest that anisotropic TMDCs like $ReSe_2$ and ReS_2 show strain-direction-dependent carrier mobilities, the highest values corresponding to a strain applied perpendicularly to the layers.[107] These studies suggest that a proper exploitation of these effects can lead to the design of high performance flexible devices.[45]

Other applications of 2D materials span from the field of polymer nanocomposites (leading to enhanced mechanical and peculiar electric properties)[108] to the fabrication of chemical and biological sensors.[6] For the latter case, graphene oxide has been used for the detection of H_2O_2,[109] NO_2 and Cl_2[110] while graphene as even been used for the detection of one single bacterium in tooth enamel.[111]

Graphene has very beneficial effects even as additive in anti-electrochemical-corrosion primers. Currently, zinc-rich epoxy primers (70wt% of zinc) are used, but the production of zinc powders is dangerous for the environment as well as for the health of the workers.[74] Recently, it has been shown that the use of 1wt% of graphene oxide, combined with 20wt% of zinc powder, leads to an anti-corrosion primer that last 4 times longer than the current technology (moreover, the 1wt% of graphene oxide is cheaper than the 50wt% zinc powder that is being substituted, even considering the currently available production procedures).[74] This graphene-based zinc epoxy primer has been already tested on a windmill tower in the East China Sea (in 2014) and led the Jiangsu Toppen Technology Co. Ltd to invest in the large scale production of this kind of anti-corrosion primers.

Moreover, there are already commercially available graphene-based touch panel and thermal heaters. This has been possible thanks to the flexibility and chemical stability of graphene that outperforms state-of-the-art materials like indium tin oxide and silver nanowires.[74]

Very promising results have been achieved in the field of hydrogen evolution reaction (HER).[112,113] The case of TMDCs is the most intriguing because of their electronic properties and the possibility to change their chemical and mechanical properties.[113,114] In particular, for the case of MoS_2, it has been shown that the S-sites edges are responsible for the HER activity[115] and that single-metal atom doping (*i.e.*, Pt, Co and Ni) can enhance the resulting performance.[116]

Lastly, 2D materials are good candidates for their use in energy applications[112] for both storage (*i.e.*, in Li-ion batteries[117,118] and supercapacitors[119–121]) and generation (*i.e.*, in organic[122,123] and perovskite solar cells[124,125]). Indeed, the results presented in this thesis deal with the use of 2D materials in supercapacitors (energy storage devices - chapter 2) and in perovskite solar cells (energy generation devices - chapter 3).

REFERENCES

1. Geim, A. K. & Novoselov, K. S. The rise of graphene. *Nat. Mater.* **6**, 183–191 (2007).
2. Mas-Ballesté, R., Gómez-Navarro, C., Gómez-Herrero, J. & Zamora, F. 2D materials: To graphene and beyond. *Nanoscale* **3**, 20–30 (2011).
3. Geim, A. K. Graphene prehistory. *Phys. Scr.* 014003 (2012). doi:10.1088/0031-8949/2012/T146/014003
4. Novoselov, K. S. *et al.* Electric field in atomically thin carbon films. *Science (80-.).* **306**, 666–669 (2004).
5. Kolobov, A. V. & Tominaga, J. *Two-dimensional transition-metal dichalcogenides*. (Springer International Punlishing Switzerland, 2016). doi:10.1007/978-3-319-31450-1
6. Bonaccorso, F., Bartolotta, A., Coleman, J. N. & Backes, C. 2D-Crystal-Based Functional Inks. *Adv. Mater.* **28**, 6136–6166 (2016).
7. Nicolosi, V., Chhowalla, M., Kanatzidis, M. G., Strano, M. S. & Coleman, J. N. Liquid Exfoliation of Layered Materials. *Science (80-.).* **340**, (2013).
8. Liu, S. *et al.* Facile preparation of novel and active 2D nanosheets from non-layered and traditionally non-exfoliable earth-abundant materials. *J. Mater. Chem. A* (2019).
9. Rao, C. N. R., Sood, A. K., Subrahmanyam, K. S. & Govindaraj, A. Graphene: The new two-dimensional nanomaterial. *Angew. Chemie - Int. Ed.* **48**, 7752–7777 (2009).
10. Geim, A. K. Graphene: Status and prospects. *Science (80-.).* **324**, 1530–1534 (2009).
11. Katsnelson, M. I. Graphene: Carbon in two dimensions. *Mater. Today* **10**, 20–27 (2007).
12. Katsnelson, M. I., Novoselov, K. S. & Geim, a. K. Chirial tunnelling and the Klein paradox in graphene. *Nat. Phys.* **2**, 620–625 (2006).
13. Thune, E. Investigations on carbon nanotubes Title. *Conference proceeding: Workshop report IV of the Windberg Meeting* (2004).
14. Novoselov, K. S. *et al.* Two-dimensional gas of massless Dirac fermions in graphene. *Nature* **438**, 197–200 (2005).

15. Morozov, S. V. *et al.* Giant intrinsic carrier mobilities in graphene and its bilayer. *Phys. Rev. Lett.* **100**, 016602 (2008).

16. Chen, J. H., Jang, C., Xiao, S., Ishigami, M. & Fuhrer, M. S. Intrinsic and extrinsic performance limits of graphene devices on SiO 2. *Nat. Nanotechnol.* **3**, 206–209 (2008).

17. Akturk, A. & Goldsman, N. Electron transport and full-band electron-phonon interactions in graphene. *J. Appl. Phys.* **103**, 053702 (2008).

18. Nair, R. R. *et al.* Fine Structure Constant Defines Visual Transparency of Graphene. *Science (80-.).* **320**, 1308 (2008).

19. Bao, Q. *et al.* Atomic-layer craphene as a saturable absorber for ultrafast pulsed lasers. *Adv. Funct. Mater.* **19**, 3077–3083 (2009).

20. Zheng, Z. *et al.* Microwave and optical saturable absorption in graphene. *Opt. Express* **20**, 23201–23214 (2012).

21. Balandin, A. A. *et al.* Superior thermal conductivity of single-layer graphene. *Nano Lett.* **8**, 902–907 (2008).

22. Seol, J. H. *et al.* Two-dimensional phonon transport in supported graphene. *Science (80-.).* **328**, 213–216 (2010).

23. Lee, C., Wei, X., Kysar, J. W. & Hone, J. Measurement of the elastic properties and intrinsic strength of monolayer graphene. *Science (80-.).* **321**, 385–388 (2008).

24. Frank, I. W., Tanenbaum, D. M., van der Zande, A. M. & McEuen, P. L. Mechanical properties of suspended graphene sheets. *J. Vac. Sci. Technol. B Microelectron. Nanom. Struct.* **25**, 2558–2561 (2007).

25. Pereira, V. M., Castro Neto, A. H. & Peres, N. M. R. Tight-binding approach to uniaxial strain in graphene. *Phys. Rev. B - Condens. Matter Mater. Phys.* **80**, 045401 (2009).

26. Ferrari, A. C. *et al.* Science and technology roadmap for graphene, related two-dimensional crystals, and hybrid systems. *Nanoscale* **7**, 4598–4810 (2015).

27. Berry, V. Impermeability of graphene and its applications. *Carbon N. Y.* **62**, 1–10 (2013).

28. Hu, S. *et al.* Proton transport through one-atom-thick crystals. *Nature* **516**, 227–230 (2014).

29. Georgakilas, V. *et al.* Functionalization of Graphene: Covalent and

Non-Covalent Approaches, Derivatives and Applications. *Chem. Rev.* **112**, 6156–6214 (2012).

30. Bai, H., Li, C. & Shi, G. Functional composite materials based on chemically converted graphene. *Adv. Mater.* **23**, 1089–1115 (2011).
31. Liu, Z., Lau, S. P. & Yan, F. Functionalized graphene and other two-dimensional materials for photovoltaic devices: device design and processing. *Chem. Soc. Rev.* **44**, 5638–5679 (2015).
32. Xia, F., Mueller, T., Lin, Y. M., Valdes-Garcia, A. & Avouris, P. Ultrafast graphene photodetector. *Nat. Nanotechnol.* **4**, 839–843 (2009).
33. Liu, M., Zhang, R. & Chen, W. Graphene-Supported Nanoelectrocatalysts for Fuel Cells: Synthesis, Properties, and Applications. *Chem. Rev.* **114**, 5117–5160 (2014).
34. Wu, Z. S., Feng, X. & Cheng, H. M. Recent advances in graphene-based planar micro-supercapacitors for on-chip energy storage. *Natl. Sci. Rev.* **1**, 277–292 (2014).
35. Zhai, Y. *et al.* Carbon materials for chemical capacitive energy storage. *Adv. Mater.* **23**, 4828–4850 (2011).
36. Shahil, K. M. F. & Balandin, A. A. Thermal properties of graphene and multilayer graphene: Applications in thermal interface materials. *Solid State Commun.* **152**, 1331–1340 (2012).
37. Ghosh, S. *et al.* Extremely high thermal conductivity of graphene: Prospects for thermal management applications in nanoelectronic circuits. *Appl. Phys. Lett.* **92**, 151911 (2008).
38. Huang, X., Qi, X., Boey, F. & Zhang, H. Graphene-based composites. *Chem. Soc. Rev.* **41**, 666–686 (2012).
39. Liu, Y., Dong, X. & Chen, P. Biological and chemical sensors based on graphene materials. *Chem. Soc. Rev.* **41**, 2283–2307 (2012).
40. Mao, H. Y. *et al.* Graphene: Promises, Facts, Opportunities, and Challenges in Nanomedicine. *Chem. Rev.* **113**, 3407–3424 (2013).
41. Schaibley, J. R. *et al.* Valleytronics in 2D materials. *Nat. Rev. Mater.* **1**, 16055 (2016).
42. Wang, Q. H., Kalantar-Zadeh, K., Kis, A., Coleman, J. N. & Strano, M. S. Electronics and optoelectronics of two-dimensional transition metal dichalcogenides. *Nat. Nanotechnol.* **7**, 699–712 (2012).

43. Choi, W. *et al.* Recent development of two-dimensional transition metal dichalcogenides and their applications. *Mater. Today* **20**, 116–130 (2017).

44. Zhang, Y. J., Oshida, M. Y., Suzuki, R. & Iwasa, Y. 2D crystals of transition metal dichalcogenide and their iontronic functionalities. *2D Mater.* **2**, 044004 (2015).

45. Manzeli, S., Ovchinnikov, D., Pasquier, D., Yazyev, O. V. & Kis, A. 2D transition metal dichalcogenides. *Nat. Rev. Mater.* **2**, 17033 (2017).

46. Chhowalla, M. *et al.* The chemistry of two-dimensional layered transition metal dichalcogenide nanosheets. *Nat. Chem.* **5**, 263–275 (2013).

47. Mak, K. F. & Shan, J. Photonics and optoelectronics of 2D semiconductor transition metal dichalcogenides. *Nat. Photonics* **10**, 216 (2016).

48. Jariwala, D., Sangwan, V. K., Lauhon, L. J., Marks, T. J. & Hersam, M. C. Emerging device applications for semiconducting two-dimensional transition metal dichalcogenides. *ACS Nano* **8**, 1102–1120 (2014).

49. Fiori, G. *et al.* Electronics based on two-dimensional materials. *Nat. Nanotechnol.* **9**, 768–779 (2014).

50. Desai, S. B. *et al.* MoS2 transistors with 1-nanometer gate lengths. *Science (80-.).* **354**, 99–102 (2016).

51. Xi, X. *et al.* Strongly enhanced charge-density-wave order in monolayer NbSe 2. *Nat. Nanotechnol.* **10**, 765–769 (2015).

52. Ugeda, M. M. *et al.* Characterization of collective ground states in single-layer NbSe 2. *Nat. Phys.* **12**, 92–97 (2016).

53. Albertini, O. R. *et al.* Zone-center phonons of bulk, few-layer, and monolayer 1T-TaS2: Detection of commensurate charge density wave phase through Raman scattering. *Phys. Rev. B* **93**, 214109 (2016).

54. Balendhran, S., Walia, S., Nili, H., Sriram, S. & Bhaskaran, M. Elemental analogues of graphene: Silicene, germanene, stanene, and phosphorene. *Small* **11**, 640–652 (2015).

55. Ling, X., Wang, H., Huang, S., Xia, F. & Dresselhaus, M. S. The renaissance of black phosphorus. *Proc. Natl. Acad. Sci.* **112**, 4523–4530 (2015).

56. Miró, P., Audiffred, M. & Heine, T. An atlas of two-dimensional materials. *Chem. Soc. Rev.* **43**, 6537 (2014).

57. Coleman, C. C., Goldwhite, H. & Tikkanen, W. A Review of Intercalation in Heavy Metal Iodides. *Chem. Mater.* **10**, 2794–2800 (1998).

58. Ma, R. & Sasaki, T. Nanosheets of oxides and hydroxides: Ultimate 2D charge-bearing functional crystallites. *Adv. Mater.* **22**, 5082–5104 (2010).

59. Demirci, S., Avazll, N., Durgun, E. & Cahangirov, S. Structural and electronic properties of monolayer group III monochalcogenides. *Phys. Rev. B* **95**, 115409 (2017).

60. Dai, J., Li, M. & Zeng, X. C. Group IVB transition metal trichalcogenides: a new class of 2D layered materials beyond graphene. *Wiley Interdiscip. Rev. Comput. Mol. Sci.* **6**, 211–222 (2016).

61. McGuire, M. A. Crystal and magnetic structures in layered, transition metal dihalides and trihalides. *Crystals* **7**, 121 (2017).

62. Anasori, B., Lukatskaya, M. R. & Gogotsi, Y. 2D metal carbides and nitrides (MXenes) for energy storage. *Nat. Rev. Mater.* **2**, 16098 (2017).

63. Bonaccorso, F. *et al.* Production and processing of graphene and 2d crystals. *Mater. Today* **15**, 564–589 (2012).

64. Xu, Y. & Yan, X.-T. *Chemical vapour deposition: an integrated engineering deisgn for advanced materials*. (Springer, 2009).

65. Li, X. *et al.* Large-area synthesis of high-quality and uniform graphene films on copper foils. *Science (80-.).* **324**, 1312–1314 (2009).

66. Addou, R., Dahal, A., Sutter, P. & Batzill, M. Monolayer graphene growth on Ni(111) by low temperature chemical vapor deposition. *Appl. Phys. Lett.* **100**, 021601 (2012).

67. Luo, Z. *et al.* Effect of substrate roughness and feedstock concentration on growth of wafer-scale graphene at atmospheric pressure. *Chem. Mater.* **23**, 1441–1447 (2011).

68. Kim, H. *et al.* Activation energy paths for graphene nucleation and growth on Cu. *ACS Nano* **6**, 3614–3623 (2012).

69. Fanton, M. A. *et al.* Characterization of graphene films and transistors grown on sapphire by metal-free chemical vapor deposition. *ACS Nano* **5**, 8062–8069 (2011).

70. Herron, C. R., Coleman, K. S., Edwards, R. S. & Mendis, B. G. Simple and scalable route for the 'bottom-up' synthesis of few-layer graphene platelets and thin films. *J. Mater. Chem.* **21**, 3378–3383 (2011).

71. Sun, J. *et al.* Graphene Glass from Direct CVD Routes: Production and Applications. *Adv. Mater.* **28**, 10333–10339 (2016).

72. Chen, M., Haddon, R. C., Yan, R. & Bekyarova, E. Advances in transferring chemical vapour deposition graphene: A review. *Mater. Horizons* **4**, 1054 (2017).

73. Qing, F., Hou, Y., Stehle, R. & Li, X. Chemical vapor deposition synthesis of graphene films. *APL Mater.* **7**, 020903 (2019).

74. Zhu, Y., Ji, H., Cheng, H. M. & Ruoff, R. S. Mass production and industrial applications of graphene materials. *Natl. Sci. Rev.* **5**, 90–101 (2018).

75. Mishra, N., Boeckl, J., Motta, N. & Iacopi, F. Graphene growth on silicon carbide: A review. *Phys. Status Solidi Appl. Mater. Sci.* **9**, 2277–2289 (2016).

76. de Heer, W. A. *et al.* Large area and structured epitaxial graphene produced by confinement controlled sublimation of silicon carbide. *Proc. Natl. Acad. Sci.* **108**, 16900–16905 (2011).

77. Emtsev, K. V. *et al.* Towards wafer-size graphene layers by atmospheric pressure graphitization of silicon carbide. *Nat. Mater.* **8**, 203 (2009).

78. Tromp, R. M. & Hannon, J. B. Thermodynamics and kinetics of graphene growth on SiC(0001). *Phys. Rev. Lett.* **102**, 106104 (2009).

79. Yang, W. *et al.* Epitaxial growth of single-domain graphene on hexagonal boron nitride. *Nat. Mater.* **12**, 792–797 (2013).

80. Ago, H. *et al.* Epitaxial chemical vapor deposition growth of single-layer graphene over cobalt film crystallized on sapphire. *ACS Nano* **4**, 7407–7414 (2010).

81. Yi, M. & Shen, Z. A review on mechanical exfoliation for the scalable production of graphene. *J. Mater. Chem. A* **22**, 11700–11715 (2015).

82. Sinclair, R., Suter, J. & Coveney, P. Micromechanical exfoliation of graphene on the atomistic scale. *Phys. Chem. Chem. Phys.* **21**, 5716 (2019).

83. Frindt, R. F. The optical properties of single crystals of WSe2and MoTe2. *J. Phys. Chem. Solids* **24**, 1107–1112 (1963).

84. Hernandez, Y. *et al.* High-yield production of graphene by liquid-phase exfoliation of graphite. *Nat. Nanotechnol.* **3**, 563–568 (2008).

85. Moridi, A., Hassani-Gangaraj, S. M., Guagliano, M. & Dao, M. Cold spray coating: review of material systems and future perspectives. *Surf. Eng.* **30**, 369–395 (2014).

86. Najafi, L. *et al.* Engineered MoSe2-Based Heterostructures for Efficient Electrochemical Hydrogen Evolution Reaction. *Adv. Energy Mater.* **8**, 1703212 (2018).

87. de Gans, B. J., Duineveld, P. C. & Schubert, U. S. Inkjet Printing of Polymers: State of the Art and Future Developments. *Adv. Mater.* **16**, 203–213 (2004).

88. Eom, S. H. *et al.* High efficiency polymer solar cells via sequential inkjet-printing of PEDOT:PSS and P3HT:PCBM inks with additives. *Org. Electron. physics, Mater. Appl.* **11**, 1516–1522 (2010).

89. Withers, F. *et al.* Heterostructures produced from nanosheet-based inks. *Nano Lett.* **14**, 3987–3992 (2014).

90. Svedberg, T. & Perdersen, K. O. *The ultracentrifuge*. (Oxford Univ. Press, 1940).

91. Lotya, M. *et al.* Liquid Phase Production of Graphene by Exfoliation of Graphite in Surfactant/Water Solutions. *J. Am. Chem. Soc.* **131**, 3611–3620 (2009).

92. Backes, C. *et al.* Edge and confinement effects allow in situ measurement of size and thickness of liquid-exfoliated nanosheets. *Nat. Commun.* **5**, 4576 (2014).

93. Kang, J. *et al.* Stable aqueous dispersions of optically and electronically active phosphorene. *Proc. Natl. Acad. Sci.* **113**, 11688–11693 (2016).

94. Capasso, A. *et al.* Few-Layer MoS2 Flakes as Active Buffer Layer for Stable Perovskite Solar Cells. *Adv. Energy Mater.* **6**, 1600920 (2016).

95. Yi, M. & Shen, Z. Fluid dynamics: An emerging route for the scalable production of graphene in the last five years. *RSC Adv.* **6**, 72525–72536 (2016).

96. Del Rio Castillo, A. E. *et al.* High-yield production of 2D crystals by wet-jet milling. *Mater. Horizons* **5**, 890 (2018).

97. Liang, S. *et al.* Effects of processing parameters on massive production of graphene by jet cavitation. *J. Nanosci. Nanotechnol.* **15**, 2686–2694 (2015).

98. Nacken, T. J., Damm, C., Walter, J., Rüger, A. & Peukert, W. Delamination of graphite in a high pressure homogenizer. *RSC Adv.* **5**, 57328–57338 (2015).

99. Paton, K. R. *et al.* Scalable production of large quantities of defect-free few-layer graphene by shear exfoliation in liquids. *Nat. Mater.* **13**, 624 (2014).

100. Liu, L., Shen, Z., Yi, M., Zhang, X. & Ma, S. A green, rapid and size-controlled production of high-quality graphene sheets by hydrodynamic forces. *RSC Adv.* **4**, 36464–36470 (2014).

101. Yi, M. & Shen, Z. Kitchen blender for producing high-quality few-layer graphene. *Carbon N. Y.* **78**, 622–626 (2014).

102. Varrla, E. *et al.* Turbulence-assisted shear exfoliation of graphene using household detergent and a kitchen blender. *Nanoscale* **6**, 11810–11819 (2014).

103. Akinwande, D. *et al.* A review on mechanics and mechanical properties of 2D materials—Graphene and beyond. *Extrem. Mech. Lett.* **13**, 42–77 (2017).

104. Pattammattel, A. & Kumar, C. V. Kitchen Chemistry 101: Multigram Production of High Quality Biographene in a Blender with Edible Proteins. *Adv. Funct. Mater.* **25**, 7088–7098 (2015).

105. Radisavljevic, B., Radenovic, A., Brivio, J., Giacometti, V. & Kis, A. Single-layer MoS2 transistors. *Nat. Nanotechnol.* **10**, 1271–1275 (2011).

106. Bertolazzi, S., Brivio, J. & Kis, A. Stretching and breaking of ultrathin MoS 2. *ACS Nano* **5**, 9703–9709 (2011).

107. Yu, S. *et al.* Strain-engineering the anisotropic electrical conductance in ReS2 monolayer. *Appl. Phys. Lett.* **108**, 191901 (2016).

108. Potts, J. R., Dreyer, D. R., Bielawski, C. W. & Ruoff, R. S. Graphene-based polymer nanocomposites. *Polymer (Guildf).* **52**, 5–25 (2011).

109. Huang, L., Huang, Y., Liang, J., Wan, X. & Chen, Y. Graphene-based conducting inks for direct inkjet printing of flexible conductive patterns and their applications in electric circuits and chemical sensors. *Nano Res.* **4**, 675–684 (2011).

110. Dua, V. *et al.* All-organic vapor sensor using inkjet-printed reduced graphene oxide. *Angew. Chemie - Int. Ed.* **49**, 2154–2157 (2010).

111. Mannoor, M. S. *et al.* Graphene-based wireless bacteria detection on tooth enamel. *Nat. Commun.* **3**, 763 (2012).

112. Bonaccorso, F. *et al.* Graphene, related two-dimensional crystals, and hybrid systems for energy conversion and storage. *Science (80-.).* **347**, 1246501 (2015).

113. Deng, D. *et al.* Catalysis with two-dimensional materials and their heterostructures. *Nat. Nanotechnol.* **11**, 218 (2016).

114. Wang, H., Yuan, H., Sae Hong, S., Li, Y. & Cui, Y. Physical and chemical tuning of two-dimensional transition metal dichalcogenides. *Chem. Soc. Rev.* **44**, 2664–2680 (2015).

115. Jaramillo, T. F. *et al.* Identification of active edge sites for electrochemical H2 evolution from MoS2 nanocatalysts. *Science (80-.).* **317**, 100–102 (2007).

116. Deng, J. *et al.* Triggering the electrocatalytic hydrogen evolution activity of the inert two-dimensional MoS<inf>2</inf> surface via single-atom metal doping. *Energy Environ. Sci.* **8**, 1594–1601 (2015).

117. Stephenson, T., Li, Z., Olsen, B. & Mitlin, D. Lithium ion battery applications of molybdenum disulfide (MoS<inf>2</inf>) nanocomposites. *Energy Environ. Sci.* **7**, 209–231 (2014).

118. Sun, H. *et al.* Binder-free graphene as an advanced anode for lithium batteries. *J. Mater. Chem. A* **4**, 6886–6895 (2016).

119. Huang, Y., Liang, J. & Chen, Y. An overview of the applications of graphene-based materials in supercapacitors. *Small* **8**, 1805–1834 (2012).

120. Ansaldo, A. *et al.* High-power graphene–Carbon nanotube hybrid supercapacitors. *ChemNanoMat* **3**, 436–446 (2017).

121. Ke, Q. & Wang, J. Graphene-based materials for supercapacitor electrodes – A review. *J. Mater.* **2**, 37–54 (2016).

122. Gomez De Arco, L. *et al.* Continuous, highly flexible, and transparent graphene films by chemical vapor deposition for organic photovoltaics. *ACS Nano* **4**, 2865–2873 (2010).

123. Wan, X., Long, G., Huang, L. & Chen, Y. Graphene - A promising material for organic photovoltaic cells. *Adv. Mater.* **23**, 5342–5358 (2011).

124. Acik, M. & Darling, S. B. Graphene in perovskite solar cells: Device design, characterization and implementation. *J. Mater. Chem. A* **4**, 6185–6235 (2016).

125. Kakavelakis, G., Kymakis, E. & Petridis, K. 2D Materials Beyond Graphene for Metal Halide Perovskite Solar Cells. *Adv. Mater. Interfaces* **5**, 1800339 (2018).

GRAPHENE BASED SUPERCAPACITORS

SUMMARY

This chapter deals with two research projects, developed during the Ph.D. program, about the use of graphene as active material in electrodes for supercapacitors. Specifically, the obtained results are herein presented and were published in the papers *"Ion sliding" on graphene: novel concept to boost supercapacitor performance (Nanoscale Horizons, 2019)* and *Flexible graphene-carbon nanotubes supercapacitor with ultrahigh areal performance (ChemPlusChem, 2019)*. The first work describes the study of the tribological properties of graphene flakes (*i.e.,* the effects raising from the movement of the electrolyte ions on the graphene surface); the second project is about the facile fabrication of high-areal performance electrodes for flexible supercapacitors. Both these works were conducted in collaboration with Doctor Francesco Bonaccorso (IIT, Genova, Italy).

INTRODUCTION

Energy storage systems (ESSs) basically accumulate energy for its future use and exploitation. Usually, energy is transformed between different “forms” which determine the classification of ESSs in:[1]

- chemical ESSs, consisting of all the chemical fuels such as coal, gasoline, propane, butane and hydrogen;
- mechanical ESSs, including pressurized gas, kinetic- (such as flywheels) and potential- (hydroelectric dam) energy-based systems;
- thermal ESSs, classified in sensible heat, latent heat, absorption and adsorption systems;
- electrical ESSs, which correspond to capacitors and supercapacitors;
- electrochemical ESSs, referring to batteries, fuel cells and electrochemical capacitors.

Each of these systems is suitable for some applications, but not for others (a hydroelectric dam can’t be used to power portable electronics such as cell phones and laptops). In the context of our everyday lives, batteries and capacitors (conventional and electrochemical) represent the most ubiquitous ESSs, but each of them suffer from some limitations. In fact, batteries have slow recharge time (1 – 5 h), low specific power (<1000 W kg^{-1}), and limited cyclability (about 1000)[2,3], while capacitors show high specific power (>10000 W kg^{-1}) and life-cycles stability (almost infinite), but exhibit lower specific energy (<0.1 Wh kg^{-1}) compared to batteries (10 – 100 Wh kg^{-1}).[3] In this scenario, supercapacitors have emerged as a type of EES overwhelming the gap between batteries and capacitors. In fact, supercapacitors show higher charge/discharge rates (from seconds to minutes), life – time (>500000) and specific power (500 – 10000 W kg^{-1}) than batteries and higher specific energy (1 – 10 Wh kg^{-1}) than capacitors.[3] The working principle and the materials used for supercapacitors electrodes are responsible for these performances, as discussed in the following section.

WORKING PRINCIPLES OF SUPERCAPACITORS

Supercapacitors are devices produced by sandwiching two electrodes (soaked in an electrolyte). A separator is placed between them in order avoid their electrical contact, as shown in **figure 1.**[4,5] Accordingly to their working principles, there are three different supercapacitors categories: electrochemical double layer capacitors (EDLCs), pseudocapacitors and hybrid capacitors.

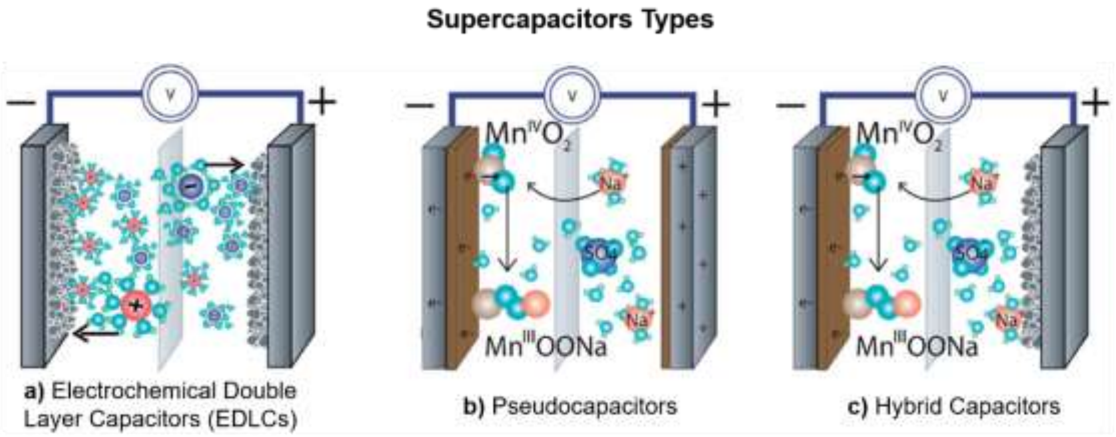

Figure 1: Schematics of supercapacitors types and working principle. (a) electrochemical double layer capacitors (EDLCs); (b) pseudocapacitors; (c) hybrid capacitors (adapted from ref. [6]).

In EDLCs, the electrical energy is stored electrostatically through ions adsorption at the interface between the electrodes and the electrolyte (**figure 1a**).[4,5] This is a purely non-faradaic, electrostatic and surface phenomenon, since no charge is transferred across the electrodes. For this reason, the materials employed for EDLCs electrodes have to exhibit high specific surface area (SSA). Not by chance, nanostructured allotropes of carbon, including activated carbon (AC)[7], carbide-derived carbon[8,9], graphene[10,11] and carbon nanotubes (CNTs)[12–14] are the most investigated active materials for EDLCs.[3–5]

Pseudocapacitance, on the other hand, is due to faradaic electron charge transfer between electrode and electrolyte. This is accomplished through electrosorption, reduction-oxidation reactions (redox reactions) and intercalation processes (**figure 1b**). Transition metal oxides (like RuO_2, Fe_3O_4, MnO_2),[15,16] conducting polymers (such as polyaniline)[17] and oxygen or nitrogen-containing surface functional groups[18] are prototypical pseudo-capacitive materials. Although pseudocapacitors show higher capacitance with respect to EDLCs, the chemical reactions and the low conductivity of the electroactive materials result in devices with low stability and power density.[5,19] For these reasons, EDLCs and pseudocapacitors are sometimes employed synergistically, leading to the fabrication of the so called hybrid capacitors (**figure 1c**). In the present work, researches has been focused on EDLCs.

For the special case of EDLCs, the absence of irreversible and slow chemical reactions (otherwise present in lithium-ion batteries[4,5] suffering intercalation-induced stresses that can cause material swelling[20,21] and subsequent electrode failure[22]) determines the main properties: fast charge rates (from milliseconds to seconds)[3], high specific power ($>10^3$ W kg^{-1})[3] and long life stability (millions of charge/discharge cycles)[23]. Consequently, EDLCs suit for a broad range of applications, including regenerative breaking in electric and hybrid electric vehicles,[24,25] short-term energy storage[26] in consumer electronics[27] and communication systems,[28] or burst-mode power delivery[29–31].

MATERIALS FOR SUPERCAPACITORS ELECTRODES

Commercial EDLCs make use of AC[32] due to their large surface area (1000 – 3500 m^2 g^{-1})[5] and low cost (<30 USD kg^{-1}).[33] AC are produced through heat treatment of carbon-rich organic precursors (such as coconut shells, wood, coal or synthetic polymers) in inert atmosphere with subsequent oxidation.[4] This procedure leads to the formation of porous carbon particles with an optimal distribution of pore sizes, including: micropores (pores whose diameter is <2 nm), mesopores (2 – 50 nm) and, possibly, macropores (>50 nm).[4,5,19] The electrodes are typically produced by depositing an AC-based paste (made up by mixing AC with conductivity enhancers and binders in the form of slurry) on a metallic substrate, acting as current collector resulting in devices showing ~100 F g^{-1}.[33,34] However, the use of AC leads to some major drawbacks. First of all, binders are insulating polymers that reduce the conductivity of the produced electrodes, leading to the use of conductivity enhancer. Furthermore, the deposition of the active material can reach mass loadings limited to ~10 mg cm^{-2} because higher values results in brittle films which undermine the mechanical integrity of the final EDLCs.[35] Moreover, the presence of micropores in the AC structure restricts the accessibility of the solvated electrolyte ions, limiting: 1) the maximum power density;[36,37] 2) the energy density and 3) the weight packaging of the resulting devices.[35]

It is worth noticing that many studies have shown that micropores are responsible for an important capacitive contribution, contradicting the classical theory of solvated ions adsorption.[38–41] It was proposed that this is possible by considering that ions can lose at least part of their solvated shells when accessing micropores.[42–44] The proper exploitation of this phenomenon has paved the way towards the design of nanoporous carbon electrodes with an extraordinary energy density (*e.g.*, >20 Wh kg^{-1} for a "full" device, including active material, current collectors, electrolyte, separator, binder and packaging).[45,46] This result demonstrates that there is still a need for a thorough and deep analysis of the physico-chemical processes occurring during the charge/discharge mechanisms.

In order to extend the application field of EDLCs, major research mainly aimed to increase the energy density of EDLCs (<10 Wh kg^{-1} for commercial EDLCs[47]), in order to reach that of the batteries (30 – 70 Wh kg^{-1} for Ni-Cd,[48] 50 – 120 Wh kg^{-1} for Ni–MH batteries,[49,50] 150 – 270 Wh kg^{-1} for Li-ion batteries[51]).[52,53] With the aim to balance the electrochemical properties, mechanical properties and the processing technologies during EDLCs design, a strong research effort has been focused on carbon-based active materials alternative to AC.[54–59] Among them, graphene is one of the most promising[55,58,60–62], due to its physical and chemical properties *i.e.*, charge carriers mobility (>2000 cm^{2} V^{-1} s^{-1} on SiO_2 substrates),[63,64] theoretical specific surface area (~2600 m^{2} g^{-1}),[65] excellent mechanical properties (Young module of ~1 TPa)[66] and elastic limit (~20%).[67] However, on the one hand, graphene flakes tend to re-stack during film deposition due to van der Waals forces,[68–70] forming piles horizontally oriented with respect to the substrates (current collectors).[71,72] To face this hurdle, CNTs has been used to act as spacers between the flakes,[70,73] as well as to anisotropically orient the latter ones, increasing their electrochemically accessible surface area in vertical (*i.e.*, sandwich-like) EDLCs configurations.[70,73] On the other hand, scalable production of graphene is challenging,[74–76] slowing down the manufacturing of graphene-based EDLCs on an industrial-scale.[77,78]

As discussed in the previous chapter, one of the most promising scalable methods to produce graphene is the liquid phase exfoliation (LPE) method, based on the exfoliation of bulk graphite in liquid solvents.[79] However, for prototypical LPE methods (*i.e.*, ultrasonication[80–82] and shear mixing[74,83]) the time required to obtain 1 g of exfoliated material (t_{1gram}), the volume of solvent required to produce 1 g of exfoliated material, (V_{1gram}), as well as the ratio between the weight of the final graphitic material and the weight of the starting graphite flakes (defined as exfoliation yield –Y_W–), are still insufficient for industrial-scale production rate (in the order of kg/day).[82,84,85] Recently, the Graphene Labs of the Istituto Italiano di Tecnologia (IIT, Genova, Italy) presented a novel approach for the exfoliation of graphite (as well as other layered crystals), based on high-pressure wet-jet-milling (WJM),[76,86,87] resulting in a production rate of 2 L h^{-1} of defect-free and high quality single-/few-layer graphene (SLG/FLG) flakes dispersion in N-methyl-2-pyrrolidone (NMP) with high concentration (10 g L^{-1}),[76,86] making the graphene scaling-up more affordable (material production rate ~0.5 kg/day).

In this chapter, the use of WJM produced graphene dispersions (WJM–G) as well as isolated WJM–G powders are discussed. Firstly, the WJM working principle and the characterization of the WJM–G are reported. Then a project, concerning the use of hybrid WJM–G/AC active material, is presented to study the tribological properties of the electrolyte ions onto AC, WJM–G and the hybrid WJM–G/AC. Lastly, the use of hybrid WJM–G/CNTs active materials is reported to scale-up the production of high areal performance, flexible and self-standing electrodes for EDLCs. These projects were carried out in collaboration with the Graphene Labs of IIT (Genova, Italy).

METHODS

WET-JET MILLING GRAPHENE PRODUCTION AND CHARACTERIZATION

During the research activities of this thesis, SLG/FLG were produced through WJM approach. Experimentally,[76] a starting dispersion containing graphite (200 g, + 100 mesh from Sigma Aldrich®) and NMP (99%, 20 L, Sigma Aldrich®) is mixed with a mechanical stirrer (Eurostar digital Ika-Werke) in a container.

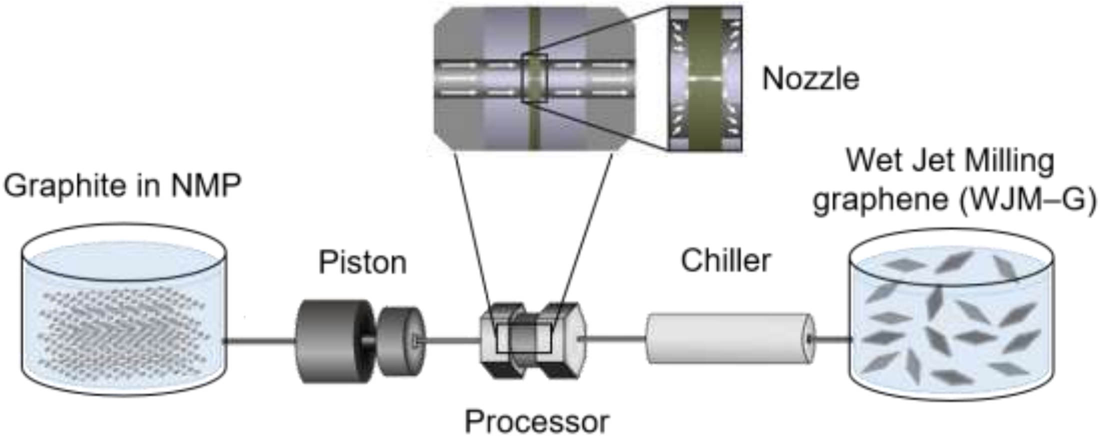

Figure 2: Production of graphene by wet jet milling exfoliation of graphite. Sketch of the WJM exfoliation of graphite in NMP. The starting dispersion of graphite in NMP is pressurised by a piston through the processor, where the exfoliation occurs. The produced SLG/FLG is cooled down to avoid changes in the solvent viscosity due to temperature rise.

As sketched in **figure 2**, a hydraulic piston supplies a pressure of 250 MPa to push the as-prepared mixture into the processor, which is a set of 5 different perforated and interconnected disks. Two jet streams originate at the second disk that consists of two holes with a diameter of 1 mm. Then, the jet streams collide between the second and the third disks, given by a nozzle (*i.e.*, a half-cylinder channel) with 0.3 mm of diameter. The shear force generated by the solvent when the sample passes through such nozzle promotes the graphite exfoliation, as theoretically described in ref.[86] The sample is then separated in two jet streams, which recombine in the last disk before leaving the processor. Immediately after the processor, the sample is cooled down by means of a chiller, to avoid changes in the solvent viscosity due to temperature rise. The processed sample is then collected and consecutively passes through nozzles with different sizes: 0.20 mm nozzle (1 time), 0.15 mm nozzle (1 time) and, finally, the 0.10 mm (5 times). The WJM passed sample in NMP results in the WJM–G dispersion, which refers to a dispersion of SLG/FLG flakes. Following this procedure, by properly selecting a suitable nozzle diameter and size-sequence, it is possible to tailor-make the exfoliation process.[76] In this work, the graphene dispersion was produced with an 8-WJM passes procedure, with the aim to reduce the lateral dimension and thickness of the as-produced flakes, which is pivotal for obtaining high-specific surface active materials to be exploited in EDLCs.[3–5,23]

It is noteworthy that NMP is used as dispersant solvent during the WJM process because its surface tension (40.8 mJ m^{-2})[88] is close to the surface free energy of graphite (~62 mJ m^{-2}).[88,89] Therefore, the choice of NMP reduces the Gibbs free energy of the mixture solvent/graphite (theoretical minimum reached when surface tension of the solvent is equal to surface energies of graphite),[88] which has to be minimized for attaining ideal exfoliation condition.[88,90,91]

Just to give an idea of the resource-savings with the WJM technique, the time required to produce 1 g of SLG/FLG (t_{1gram}) is 4.8 min, the volume of solvent required to produce 1 g of SLG/FLG (V_{1gram}) is 0.1 L and the exfoliation weight yield (Y_W), defined as the ratio between the weight of the final graphitic material and the weight of the starting graphite flakes, is ~100%.[92] These metric values overcome those of the most common exfoliation techniques, often claiming high-scalability,[79,93] reported to now.[74,75,82,83,85,94,95]

The morphology (*i.e.*, lateral size and thickness) of the exfoliated graphitic flakes was evaluated by transmission electron microscopy (TEM) (**figure 3a,b**) and atomic force microscopy (AFM) (**figure 3c,d**), respectively. The as-produced sample consists of irregularly shaped (**figure 3a**) and nm-thick flakes (**figure 3c**). Statistical analysis indicates that the thickness and the lateral size of the flakes approximately follow log-normal distributions, as expected from fragmented systems,[96] peaked at ~470 nm (**figure 3b**) and ~1.67 nm (**figure 3d**), respectively. These results indicate that the WJM–G flakes consist mainly of SLG/FLG flakes (SLG thickness ~0.34 nm[63]).

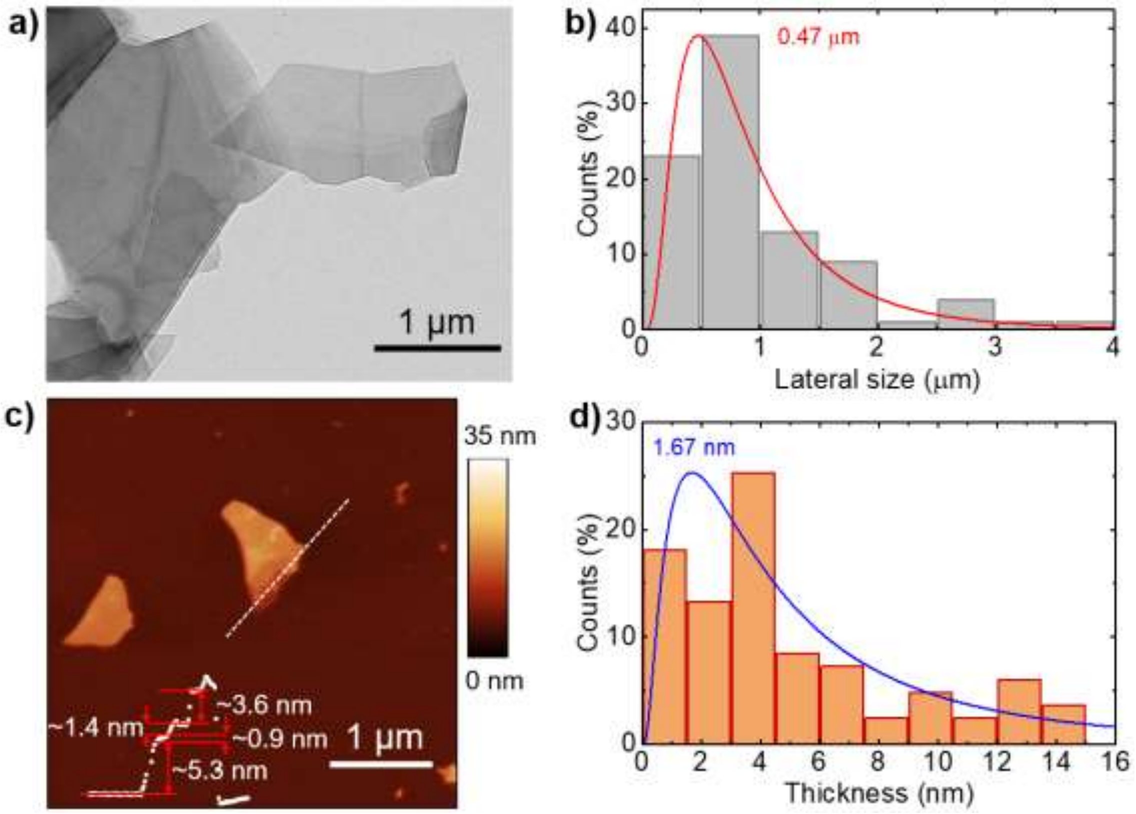

Figure 3: Morphological and structural analysis of WJM–G. (a, b) Representative TEM image of WJM–G flakes (a) together with the corresponding

statistical analysis of the lateral size (b), performed on 90 flakes. (c, d) Representative AFM image of WJM–G flakes (c) with the corresponding statistical analysis of the thickness (d), performed on 90 flakes.

Raman spectroscopy measurements were carried out to assess the structural properties of the WJM–G flakes (**figure 4a-g**). The Raman characterization, performed at an excitation wavelength of 514 nm, focused on the four main contributions of SLG/FLG: D (~1380 cm^{-1})[97], G (~1585 cm^{-1})[98,99], D' (~1620 cm^{-1})[100] and 2D (~2700 cm^{-1})[99] peaks. The D peak is due to breathing modes of sp^2 hybridized carbon atoms and requires a defect for its activation.[97,101] The G peak arises from E_{2g} phonon at the Brillouin zone centre.[98,99] The D' peak originates from a double resonance mode, due to an intra-valley process, and is present in defective graphene.[99] The 2D peak is the second order of the D peak (but it is present even in the absence of the D peak, since no defect is required for the activation of two phonons with the same momentum).[98,99]

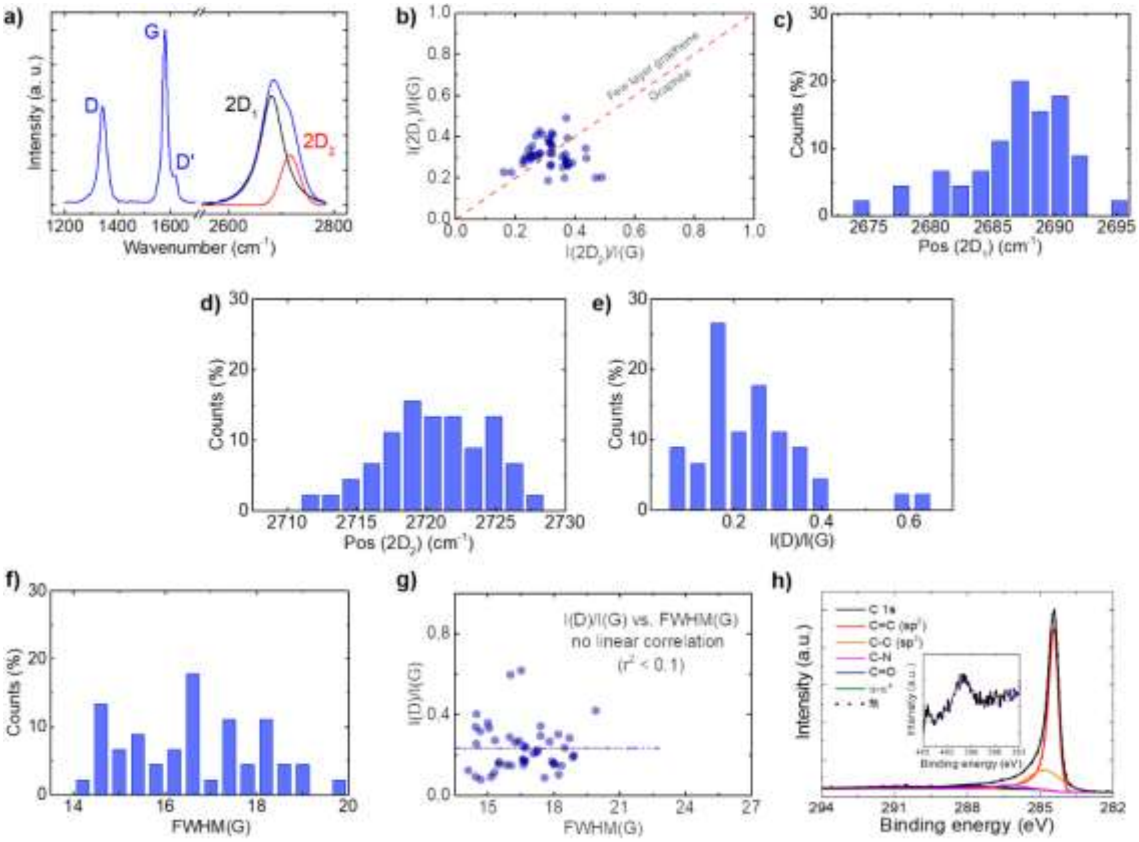

Figure 4: Raman statistical analysis and XPS of WJM–G. (a) Representative Raman spectrum of WJM–G normalized to the intensity of the G peak. The deconvolution of the 2D region is also shown: $2D_1$ peak (black), $2D_2$ peak (red). (b-g) Statistical analysis calculated by Raman spectra from 50 flakes. (b) $I(2D_1)/I(G)$ *vs*. $I(2D_2)/I(G)$. (c) Position of $2D_1$ peak. (d) Position of $2D_2$ peak. (e) I(D)/I(G). (f) FWHM(G). (g) I(D)/I(G) vs FWHM(G). (h) C 1s and N 1s (inset panel) spectra of the SLG/FLG flakes. In the main panel, the C 1s spectrum deconvolution is also shown, evidencing the bands ascribed to C=C, C-C, C-N, C=O and π-π*.

Figure 4a shows a representative Raman spectrum of WJM–G. The analysis of the 2D peak reveals that it is composed of two contributions, namely $2D_1$ and $2D_2$,[101] which provide information about the number of layers.[99,102] Experimentally, the $2D_2$ component intensity in graphite is twice the one of $2D_1$.[99,102] In SLG, just a single sharp peak appears,[101] while for FLG the $2D_1$ band becomes more intense than the $2D_2$ band.[99,102] In contrast, multi-layer graphene (>5 layers) exhibits a 2D band which is almost identical to the graphite one.[103,104] Based on these observations, the Raman spectrum of **figure 4a** can be attributed to FLG. This conclusion is quantitatively corroborated by the data shown in **figure 4b** that reports the I($2D_1$)/I(G) *vs* I($2D_2$)/I(G) plot for WJM–G. The dashed line corresponds to the condition I($2D_1$)/I(G) = I($2D_2$)/I(G). On the basis of the aforementioned considerations, data that fall above that line (I($2D_2$) > I($2D_1$)) corresponds to flakes with less than 5 layers, while below that line the flakes have more than 5 layers and become indistinguishable from graphite.[99,101] The position of $2D_1$ and $2D_2$ also gives information about the thickness,[104] because in graphite the $2D_1$ and $2D_2$ are centred at 2700 and 2725 cm^{-1}, while in SLG the single $2D_1$ component appears at 2685 cm^{-1}.[101] **Figure 4c,d** reports the statistical analysis of these positions, confirming that WJM–G mainly consist of SLG/FLG, in agreement with the AFM analysis. In **figure 4e** the intensity ratio I(D)/I(G) is reported, while in **figure 4f** the full width at half maximum of the G peak –FWHM (G)– is shown.

The crystalline quality of the flakes can be assessed by analysing the D peak.[99] Actually, two types of defects can occur in graphene flakes: edge and basal plane defects (*i.e*., in the sp^2 carbon lattices). For the latter case, I(D)/I(G) positively correlates with the amount of defects[103,105–108] and the plot of I(D)/I(G) *vs*. FWHM(G) can be used to identify their nature. [109,110] The plot of I(D)/I(G) *vs*. FWHM(G) (**figure 4g**) does not show a linear correlation (r^2 <0.1), which means that the WJM process does not induce in-plane defects into the sample.[109,110]

X-ray photoelectron spectroscopy (XPS) measurements (**figure 4h**) were carried out to prove that WJM process produce high-quality SLG/FLG flakes. In fact, the C 1s XPS spectrum of the WJM–G is dominated by a component peaking at 284.4 eV referred to sp^2 structures. These results exclude the formation of graphene oxide during the WJM process, whose functional groups can alter the chemical interaction of ions with pristine graphene.[111–113]

PREPARATION OF ACTIVE MATERIAL DISPERSIONS AND DEVICES

WJM-G/AC

The active materials of the EDLCs were obtained by mixing dried SLG/FLG flakes (as-obtained by removing NMP form WJM–G using a rotary evaporator (Heidolph® mod. HeiVap Presition MLG6) at temperature of 70°C and a pressure of 2 mbar for 2 h) with commercial AC (AB-520, MTI Corp.). SLG/FLG:AC weight ratios of 10:90, 20:80, 50:50 were investigated. Activated carbon and SLG/FLG flakes were also used solely as reference active materials. Subsequently, the active materials were mixed with carbon black (acetylene black, >99.9%, Alfa Aesar) and polyvinylidene fluoride (PVDF, average molecular weight ~534000, Sigma Aldrich) with a 85:10:5 weight ratio in a small volume of NMP (99%, Sigma Aldrich) until a homogenized paste-like consistency is obtained (slurry). The EDLCs electrodes were prepared by depositing such pastes onto Al foil by doctor blade. The corresponding pastes were dried with a hot plate at 60°C and subsequently, in a glass oven vacuum system (B-585 Kugelrohr, Buchi®) at 120°C overnight in order to remove the water absorbed by the AC and residual NMP. The EDLCs were fabricated in symmetric configuration by stacking two identical electrodes within coin cells (CR2032 cases, springs and spacers purchased from MTI Corp.) by using a compact crimper (MSK-PN110-S, MTI Corp.). A PVDF membrane with a pore size of 0.2 μm (Amersham™ Hybond™) was used as separator, while 1 M tetraethylammonium tetrafluoroborate ($TEABF_4$, >99%, Sigma

Aldrich) in propylene carbonate (PC, anhydrous, >99%, Sigma Aldrich) was used as electrolyte. This electrolyte was chosen because is a conventional organic electrolyte used in EDLCs,[114,115] for both commercial and research-prototypes due to its capability to operate without degradation in a wide range of voltages (>3 V) and temperatures (>50 °C).[116–118] The coin cells were assembled into Ar-filled glovebox with concentrations of moisture and O_2 below 0.1 ppm.

WJM-G/SDWCNTs

As discussed previously**,** graphene flakes tend to restack, reducing their available surface area for ion adsorption. For this reason, commercial CNTs have been proposed as spacers between the flakes[70,73], as well as active material for EDLCs.[12,14] Among CNTs, single/double-walled CNTs (SDWCNTs) were specifically selected in this work in order to limit the active material costs compared to that of the single-walled counterpart[119] and to exploit their superior specific surface area (*i.e.*, theoretical specific capacitance) (~ 1315 m^2 g^{-1} for single-walled CNTs,[120–122] ~ 800 m^2 g^{-1} for double wall CNTs[120]) compared to multi-walled CNTs (~50 m^2 g^{-1} for 40-wall CNTs[120]). Experimentally, a commercial mixture of SDWCNTs (outer diameter 1 – 4 nm, length 5 – 30 µm, Cheap Tubes) was dispersed in NMP (99%, Sigma Aldrich®) and de-bundled by means of a sonic tip (Branson®, 3/16' tip), through an ultrasonic bath-assisted method (**figure 5a**).[123] Pulses of 4s on and 2s off were used, with vibration amplitude of 45%. An ice bath under the rosette was used to minimize heating effects during the sonication process.

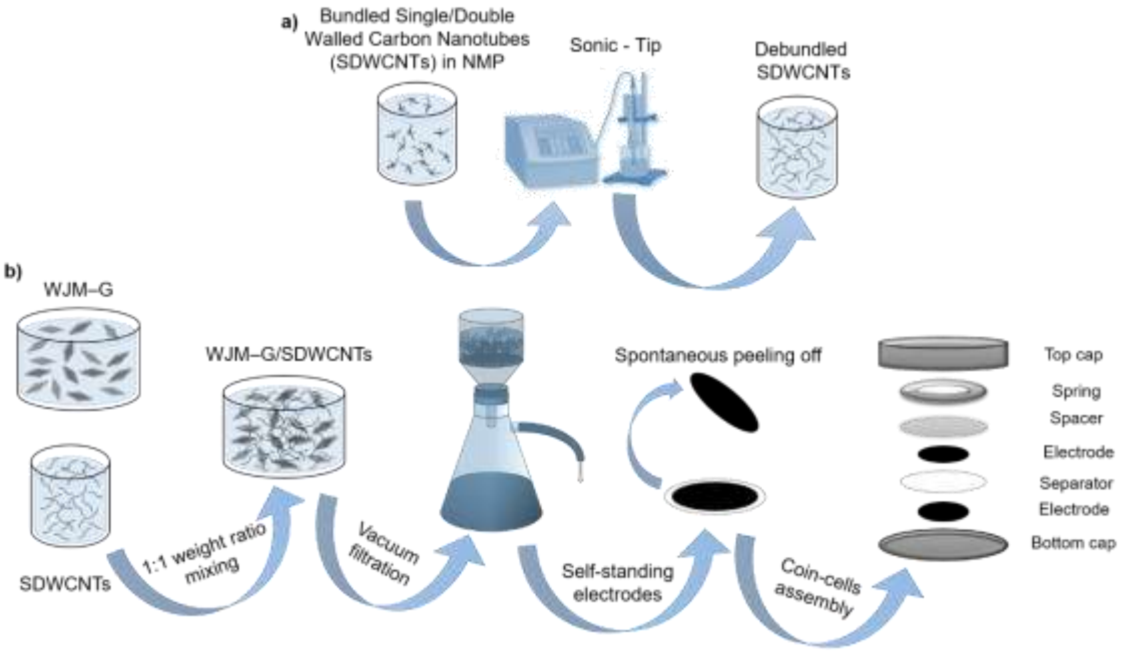

Figure 5: Debundling of SDWCNTs, preparation of electrodes and manufacturing of EDLCs. (a) Ultrasonic de-bundling of single/double walled carbon nanotubes (SDWCNTs) in NMP. (b) Sketch of the manufacturing of electrodes and EDLCs: the hybrid WJM–G/SDWCNTs dispersion prepared by mixing WJM–G and de-bundled SDWCNTs; the as-produced dispersion is deposited by vacuum filtration; the resulting peeled off film is the freestanding electrode; which is cut in pieces that are used for assembling an EDLC in coin-cell architecture.

Subsequently, SDWCNTs dispersion was mixed with WJM–G dispersion with a material weight ratio of 1:1, in agreement with previous optimized hybrid graphene/CNT[73] and graphite/CNT[124] EDLCs. By taking advantage of the dimensional form of both graphene flakes (2D) and SDWCNTs (1D), EDLC electrodes were produced by vacuum filtration (**figure 5b**), through nylon micro-pore membranes (0.2 μm pore size, 25 mm diameter, Sigma Aldrich®), of the as-produced hybrid dispersions. To achieve various mass loadings (ranging from 1.6 mg cm^{-2} to 30.4 mg cm^{-2}), different volumes of the hybrid material were filtrated. Additional washing of the electrodes in IPA was performed to remove NMP residuals from the deposited films. This procedure was carried out by filtrating, after the complete deposition of the film, a volume of IPA which was always larger than the volume of NMP used for the deposition (*e.g.* for 5 mL of NMP, 10 mL of IPA were used). The as-produced films (with 3.14 cm^2 area) spontaneously peeled off from the nylon membrane during the drying at room temperature, resulting in self-standing electrodes, which were cut with a diameter size of 0.4 cm. These electrodes were assembled in CR2032 type coin cells (stainless steel, 20 mm diameter and 3.2 mm thickness, MTI Corporation) using glass fibre separator (GF/D Whatman®). 150 µL of 1 M $TEABF_4$ in PC were used as electrolyte. The coin cells were electrochemically characterised after 2 h from their crimping in order to allow the electrolyte to diffuse throughout the electrodes.

Flexible WJM–G/SDWCNTs EDLCs were assembled by using self-standing active material films as electrode (area of 2.2 cm^2), H_3PO_4 in polyvinyl alcohol (PVA) mixture-soaked PVDF membrane as both electrolyte and separator, and silicon-adhesive Kapton® tape (Dupont®, from Tesa) as encapsulant material.

RESULTS AND DISCUSSION

GRAPHENE FLAKES AS ION-SLIDING SURFACES

INTRODUCTION

As shown in the introduction section, an EDLC is made up by two electrodes, a separator and an electrolyte: the charge/discharge mechanism is based on the adsorption of the electrolyte ions on the surface of the electrodes. This process involves the movement of nano-particles (ions) in a liquid substance (solvent) that forms an interface with the solid electrode. Such working mechanism of EDLCs suggests that a thorough understanding of the frictional behaviour between the electrolyte and the electrodes is needed. In this contest, the field of nanotribology plays an essential role. The word tribology (deriving from the Greek words *tribos* "rubbing" and -*logia* "study of") was coined in 1966 by Peter Jost, a mechanical engineer who published a report highlighting the importance and cost of friction, wear and corrosion in the United Kingdom industries.[125] Tribological studies received more interest thanks to the rise of proximal probe techniques (like scanning tunnelling and atomic force microscopy), that allowed a thorough and meticulous study of nanoscale interface phenomena occurring at the atomic or molecular level.[125] For these reasons, nanotribology led to a better understanding of the physical properties of the electrode/electrolyte interfaces occurring in supercapacitors. In the following chapter, the tribological properties of SLG/FLG (as obtained by WJM) will be discussed, showing that they act as "ion-slides" to enhance the operating power of conventional AC-based EDLCs.[33] These results offer new pathways to manage the frictional property during designing of nanoporous electrodes for EDLCs, as well as novel power-generation devices.

SOLVENT AND ION NANOTRIBOLOGY ON NANOCARBONS

Mechanical friction of graphene-based materials has been intensively studied[126] under vacuum,[127] dry gases,[128,129] or ambient conditions,[113,130,131] for their application as solid lubricant material[130,132] and potential wear resistance coating in mechanical/electrochemical micro/nanosystems.[113,127,133] However, only a few studies investigated the nanoscale interaction of graphene (as well as of other nanocarbons) with liquids, including both polar (*e.g.*, water)[134,135] and nonpolar (*e.g.*, dodecane)[134,135] solvents, for electrochemical applications.

The present work is focused on the nanotribological effects arising at the interfaces between electrodes and electrolyte in a solvent, which is currently an unexplored research area of the existing literature. To fill this shortfall, and to apply the outcomes into EDLCs technology, the interaction between SLG/FLG flake film (obtained by doctor blade deposition of isolated powders from concentrated WJM–G) and 1 M $TEABF_4$ in PC, has been studied by lateral force microscopy (LFM) measurements, as sketched in **figure 6a**.

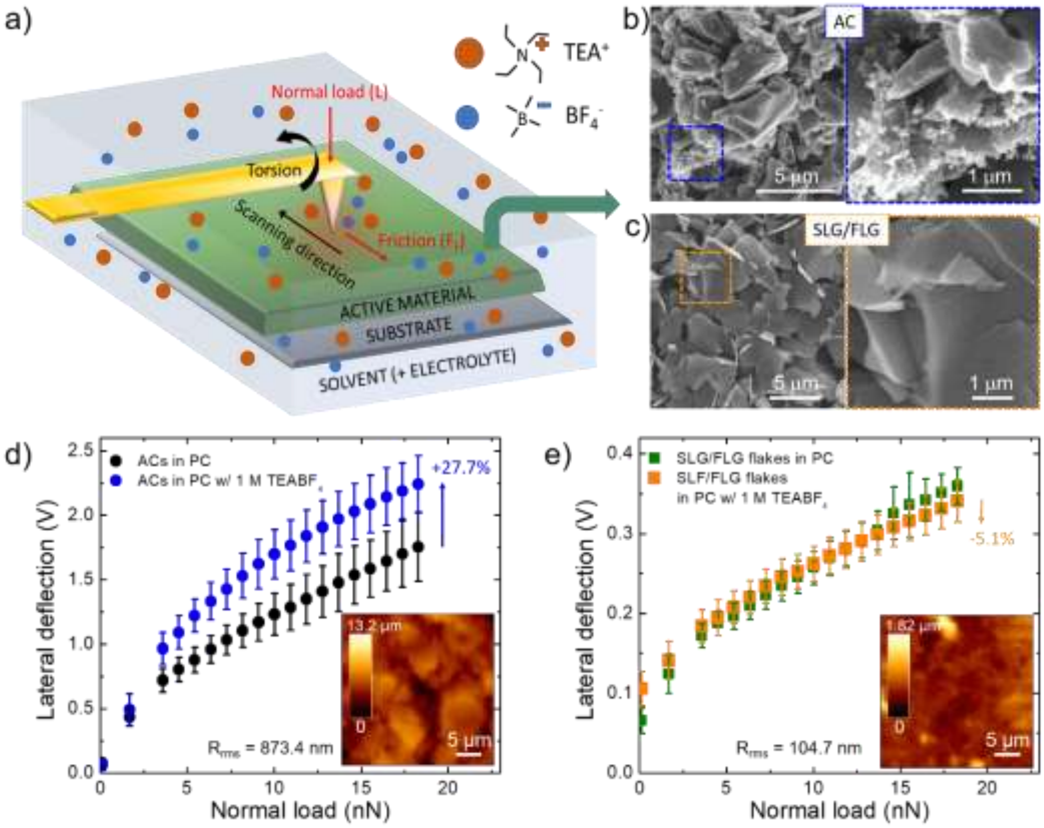

Figure 6: Solvent and ion nanotribology on AC and SLG/FLG flakes. (a) Sketch of the LFM measurement setup. (b, c) Top-view SEM images of AC (b) and SLG/FLG flake (c) films deposited onto Al foil. The corresponding areas delimited by dashed squares are magnified in the right panels. (d, e) Lateral force microscopy measurements of AC (d) and SLG/FLG flake (e) film in PC with and without 1 M $TEABF_4$. The insets in panels (d) and (e) show the AFM topography of the films. The R_{rms} values corresponding to the AFM images are also reported.

The analysis has been performed also on commercial AC (AB-520, MTI Corp.),[136] which was used as benchmark EDLCs material. Lateral force microscopy measurements were performed with an AFM-setup by detecting the cantilever torsional deflection, while scanning across the sample surface in contact mode.[137,138] Actually, the F_F values correlate linearly with the output voltage signal (V_{AFM}) resulting from the measurements of the lateral deflection of the cantilever, in agreement with the equation:[133]

$$\mathrm{F_F} = \frac{\mathrm{G_{TD} \cdot h \cdot K_L \cdot V_{AFM}}}{\mathrm{L \cdot S_{DIF}}} \qquad (3)$$

where G_{TD} is the gain torsion/deflection ratio, h is the height of the tip, K_L is the lateral spring constant, L is the length of the cantilever and S_{DIF} is the normal deflection sensitivity. Experimentally, the F_F between probes and sample surface was measured by scanning perpendicularly to the long axis of the cantilever and increasing the applied load (N) incrementally from 0 to 18 nN. Since our aim was to compare the F_F values between the AFM silicon tip and the two different film surfaces (AC and SLG/FLG) in PC (with and without $TEABF_4$ electrolyte), K_L and S_{DIF} were simply assumed as constant without calculating them. The same tip was then used during LFM measurements to exclude its contribution in the comparative force analysis of the results obtained for different films.[139] The crosstalk between normal and lateral signals was minimized by calculating the lateral deflection as half the difference between the values obtained in the two scan directions (trace and retrace).[139]

The difference between forward and reverse traces of torsion of the tip (“*friction force loop*”) provides insight into the frictional and adhesion properties of the sample,[140–144] as well as on the dynamics of the electrolyte at the interface with solids in solutions.[134,135,145] The F_F between LFM cantilever tip and the sample surface depends on the properties of the tip, the film and the liquid environment.[134,135] The capillary forces, which significantly contribute at ambient atmosphere due to the formation of a water meniscus between the cantilever tip and the film,[146] can be effectively eliminated when the film is immersed in liquid environments.[134,135] The same analysis was performed also on commercial AC (AB-520, MTI Corp.)[136].

The active material films were deposited onto Al foil (current collector) with a mass loading of ~10 mg cm^{-2}, which is compatible with the requirements of industrial EDLCs manufacturing (mass loading at least of 5 mg cm^{-2}, corresponding to an electrode thickness between 50 – 200 μm).[147,148] Such mass loading allows these results to be directly applied in practical EDLCs, without overestimating the experimental performance of the active materials, as often reported by adopting μg cm^{-2}-scale mass loading.[147–149]

Figure 6b,c report top-view scanning electron microscopy (SEM) images of the AC and the SLG/FLG flake films, respectively, evidencing the differences between the corresponding morphologies. The SLG/FLG flake film is composed of stacked graphene flakes adopting a preferential in-plane displacement, while AC film presents a mesoporous structure given by nanoparticles with a variable dimension, ranging from 0.1 μm to 10 μm. Nanoparticles with sub-μm dimensions are also present, sometimes in aggregate form, filling the space between the largest AC particles. Carbon black is considered the main source of these nanoparticles.[34] The root mean square roughness (R_{rms}) calculated by AFM scan is 104.7 nm and 873.4 nm for SLG/FLG flake and AC films, respectively. **Figure 6d,e** show the LFM responses to the lateral deflection of the cantilever tip as a function of *N* (ranging from 0 to 18 nN) at scan rate (*i.e.*, tip velocity) of 25 µm s^{-1} over SLG/FLG flake and AC films, respectively, in PC with and without electrolyte (1M, $TEABF_4$).

Noteworthy, F_F (and therefore the lateral deflection) is proportional to N, in agreement with the Amontons' law:[150,151]

$$\mathrm{F_F = S_C \cdot A + \mu \cdot N} \quad (4)$$

Where S_C is the critical shear stress, A is the contact area and μ is the friction coefficient between the AFM tip and the sample surface (considering the presence of both solvent and electrolyte). The term $S_C \cdot A$ represents the adhesion force at $N = 0$. Although μ is typically considered a material constant, experiments evidenced variation of μ with N and contact time,[152,153] providing phenomenological corrections.[154–156] This variation can cause deviations from the linear regression expressed by the Amontons' law.[152,153]

Taking into account such considerations, the results clearly show that lateral deflection (*i.e.*, the F_F) in PC is significantly higher on AC film compared to the SLG/FLG-based one. This effect arises from the low nanoscale roughness of SLG/FLG flake film compared to the AC film. In fact, as indicated before, AFM analysis (insets to **figure 6d,e**) shows a R_{rms} of 873.5 nm and 104.7 nm for AC and SLG/FLG flake films, respectively. Interestingly, the presence of $TEABF_4$ significantly increases the F_F of the AC film, while no changes of F_F are observed for SLG/FLG flake film. We interpret this observation as arising from the accumulation of electrolyte in proximity of the AFM tip that creates a solid-like interlocking layer which increases F_F.[157] The fluidity of the electrolyte in AC is supposed to be limited by the nano-confinement provided by the roughness, while the flat surface of graphene flakes can effectively squeeze out the interfacial region providing solvent-like conditions.[134] Therefore, the long range 2D-order of the sp^2 lattice of graphene intrinsically acts as “slide” for ions, fastening the electrolyte transport compared to AC films. This behaviour agrees with the ultra-low nanoscale frictional properties of few-layer graphene films,[111,138,158] which behave similarly to super-lubricating highly oriented pyrolytic graphite films (μ <0.01).[159–161]

ELECTRODES CHARACTERIZATION AND SUPERCAPACITORS FABRICATION

The elucidation of the PC and $TEABF_4$ nanotribology on films of SLG/FLG flakes and AC served to formulate hybrid AC:SLG/FLG electrode materials to be used for enhancing the electrochemical performance of AC-based EDLCs, representing the benchmark technology adopted at a massive industrial level.[34,162] Experimentally, the as-produced SLG/FLG flakes were mixed with commercial AB-520 AC at various AC:SLG/FLG weight ratios (90:10, 80:20, 50:50 w/w) to obtain EDLCs active materials (herein named AC:SLG/FLG (90:10), AC:SLG/FLG (80:20), AC:SLG/FLG (50:50)). The EDLCs electrodes were fabricated by mixing the as-produced active materials with carbon black (conductive agent) and PVDF (binder) with an 85:10:5 weight ratio in NMP (1:3 solid/liquid weight content ratio), until homogenized paste-like consistencies (slurry) were obtained. The as-produced pastes were subsequently deposited onto Al foil by doctor blade technique, and dried at 60°C, obtaining the EDLCs electrodes. Electrodes based solely on SLG/FLG flakes or AC as active materials were also produced as references. The mass loading of the electrodes was ~10 mg cm^{-2}, in agreement with requirements of commercially available EDLCs.[147,148] As discussed in the previous section, the selected mass loading avoids the experimental performance of the active materials to be overestimated, as often reported for SLG/FLG-based EDLCs by adopting μg cm^{-2}-scale mass loading.[147–149] Symmetric EDLCs were fabricated by stacking the as-produced electrodes within CR2032 coin cells, using a PVDF membrane (0.2 μm pore size) as separators and 1 M $TEABF_4$ in PC as the electrolyte. Additional details regarding the fabrication of EDLCs are reported in the Experimental section. **Figure 7a-e** show representative cross-sectional SEM images of the EDLC electrodes.

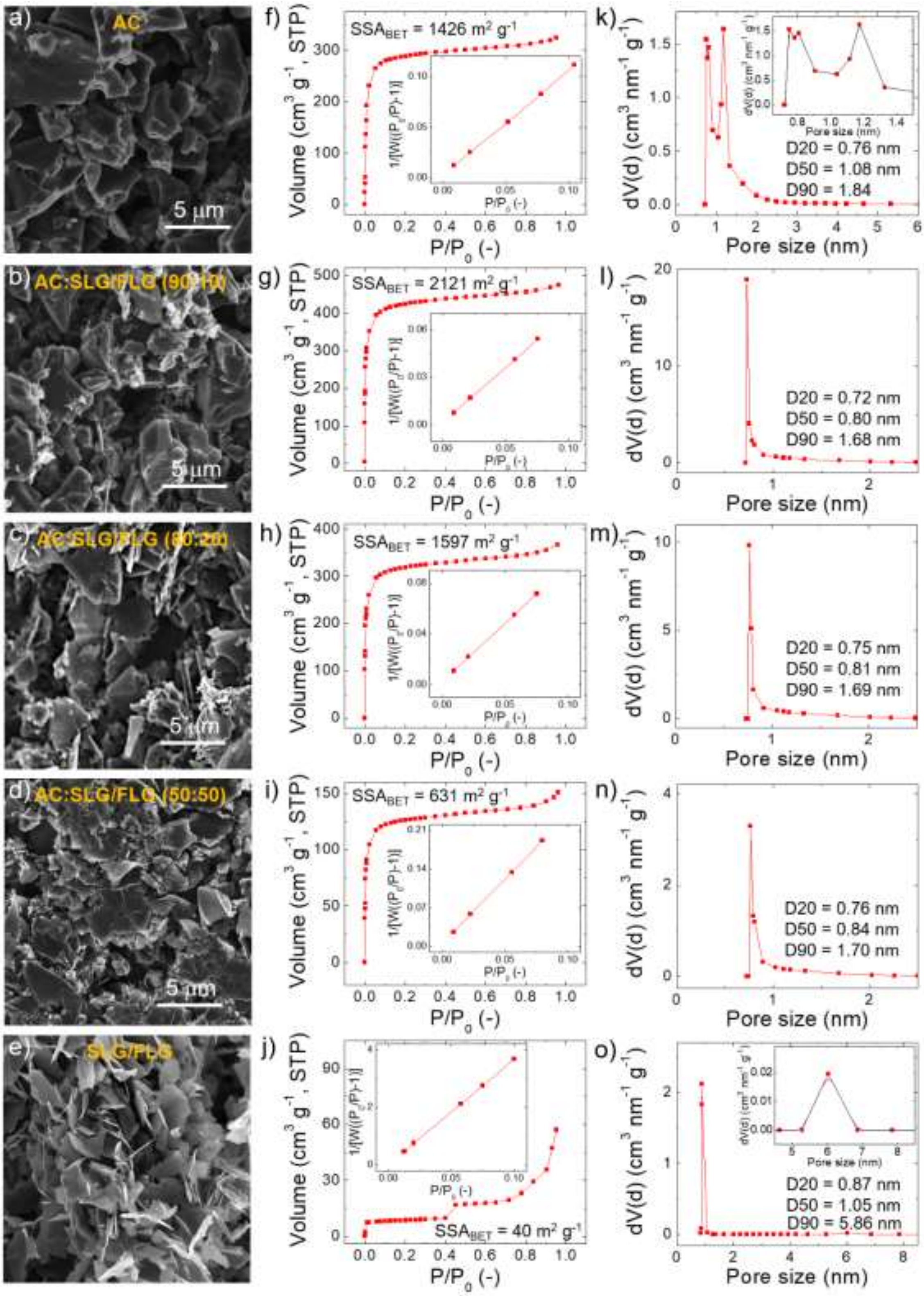

Figure 7: Morphology analysis of the EDLCs electrodes. Cross-sectional SEM images of AC (a), AC:SLG/FLG (90:10) (b), AC:SLG/FLG (80:20) (c), AC:SLG/FLG (50:50) (d) and SLG/FLG electrodes (e). (f-j) Kr physisorption isotherm curves, BET plots (insets) and calculated SSA$_{BET}$ of the electrodes. (k-o) Pore size distributions and D-values (D20, D50 and D90, corresponding to the intercepts for 20%, 50% and 90% of the cumulative mass) of the electrodes. In panel (o), the inset shows an enlargement of the pore size distribution of the

graphene electrode between 4.5 and 8.5 nm. The measurements shown on each line correspond to the same electrodes imaged by SEM.

The reference AC electrode shows a macro/mesoporous network consisting of particles including AC and carbon black, with lateral dimension ranging from sub-μm- to tens of μm-scale (**figure 7a**), in agreement with the material datasheets.[136] The hybrid AC:SLG/FLG (90:10) and AC:SLG/FLG (80:20) electrodes resemble mostly the morphology of AC electrode, suggesting that SLG/FLG flakes are randomly distributed within AC network (**figure 7b,c**). Differently, the structure of AC:SLG/FLG (50:50) electrode displays laminar domains within the AC-based network (**figure 7d**). Lastly, the SLG/FLG electrode shows a laminar structure (**figure 7e**), as expected by a film based on graphene flakes.[68–72] The SSA and the pore size distribution of the electrodes are estimated by Brunauer, Emmett and Teller (BET) analysis[163] of physisorption measurement with Kr at 77 K (**figure 7f-j**).[164–167] It is worth noting that Kr was preferred to N_2 because the quadrupole moment of the N_2 (0.27 $Å^2$)[168,169] limits the access of the gas into the micropores, giving trivial porosity values for pore size <1 nm.[164,166,167] Contrary to N_2, Kr has not a quadrupole moment and can easily access to the micropores up to its cross-sectional area (reported between 0.11 and 0.22 nm^2/atom at 77 K, depending on possible arrangements of adsorbed species on surface, as well as appropriate ranges of relative pressure),[170,171] thus suiting for physisorption characterization of microporous carbons.[167,170,171] The pore size distributions were calculated by Kr physisorption measurements at 87 K using Non-Local Density Functional Theory (NLDFT) (**figure 7k-o**).[172,173] The obtained BET SSAs (SSA_{BET}) D-values (D20, D50 AND D90, corresponding to the intercepts for 20%, 50% and 90% of the cumulative mass) of the electrodes are summarized in **Table 1**.

Electrode	SSA_{BET} (m^2 g^{-1})	D20 (nm)	D50 (nm)	D90 (nm)
AC	1426	0.76	1.08	1.84
AC:SLG/FLG (90:10)	2121	0.72	0.80	1.68
AC:SLG/FLG (80:20)	1597	0.75	0.81	1.69
AC:SLG/FLG (50:50)	631	0.76	0.84	1.70
SLG/FLG	40	0.87	1.05	5.86

Table 1. SSA_{BET} and D-values of the electrodes discussed in the text.

The SSA_{BET} for AC electrode is comparable to that indicated by the material datasheet (1666 ± 100 m^2 g^{-1})[136]. The low SSA_{BET} values measured for AC:SLG/FLG (50:50) and SLG/FLG are ascribed to the restacking of the SLG/FLG flakes during their film deposition.[68–70] Interestingly, for AC:SLG/FLG weight ratios (*i.e.*, AC:SLG/FLG (90:10), AC:SLG/FLG (80:20)), the SSA_{BET} increases compared to the AC. As previously reported, carbon nanoparticles (both AC and carbon black) act as effective spacers avoiding the re-stacking of graphene flakes.[174,175] This allows the use of the native SSA of SLG/FLG to be fully exploited,[176] creating highly packed wrinkled SLG/FLG-incorporated AC structures with SSA_{BET} higher than those of SLG/FLG and AC electrodes. Synergistically, SLG/FLG flakes can enhance the gas access into AC network. Activated carbon electrode has a multimodal pore size distribution peaking at 3.8, 4.0 and 5.9 nm (**figure 7k**). Differently, AC:SLG/FLG and SLG/FLG electrodes have nanoporous structures with size of pores mainly inferior to 1 nm (**figure 7l-o**). The peaks and the FWHMs of the pore size distribution progressively increase with increasing the SLG/FLG content (**figure 7l-o**). However, pore size distribution of SLG/FLG electrode shows also a peak at ~6.1 nm, mesoporous larger than those exhibited by hybrid electrodes.

The close-packed structures of AC:SLG/FLG, as evidenced by morphological characterization (**figure 7**), result in lower sheet resistances (R_{sheet}) (39 ± 2 Ω sq^{-1}, 26 ± 2 Ω sq^{-1}, 15 ± 2 Ω sq^{-1} and 82 ± 14 Ω sq^{-1} for AC:SLG/FLG (90:10), AC:SLG/FLG (80:20), AC:SLG/FLG (50:50), respectively) compared to those of both AC (76 ± 3 Ω sq^{-1}) and SLG/FLG (82 ± 14 Ω sq^{-1}). In fact, the carbon nanoparticles in the hybrid electrodes can act as conductive bridges between SLG/FLG flakes, thus creating highly conductive carbon paste.[177–179] However, in close-packed structures, the presence of pores with sub-nm dimension can be "*closed micropores*",[38,180–182] which can limit the electrochemical accessible surface area during the operation of EDLCs.[183]

ELECTROCHEMICAL CHARACTERIZATION

In order to achieve high electrochemical accessible area of the electrodes, the multimodal pore size distribution of AC (D50 >1 nm), as optimized for commercial active material formulations[136], should be preferred to the monomodal one of hybrid electrodes (D50 <0.85 nm).[184] However, this key-guideline does not consider the tribological properties of the active materials, which could challenge the conventional rules for designing advanced EDLCs. The synergistic effect of the morphological and tribological properties of the active materials on the electrochemical performance of the EDLCs was evaluated by both cyclic voltammetry (CV) and galvanostatic charge/discharge (CD) cycling measurements. The latter was used for calculating the gravimetric capacitance (C_g) of the SC electrodes, as given by equation:[185,186]

$$\mathrm{C_g} = 4\frac{|\mathrm{i}| \cdot \mathrm{t_d}}{\mathrm{m} \cdot \Delta \mathrm{V}} \tag{5}$$

where $|i|$ is the module of the applied current (i), t_d is the discharge time, m is the total mass of the electrodes (mass of active material + mass of carbon black + mass of PVDF + mass of Al collector) and ΔV is the voltage window of the measurement. **Figure 8a,b** shows the CV curves of the produced EDLCs at 10 mV s^{-1} and 100 mV s^{-1} voltage scan rate, respectively.

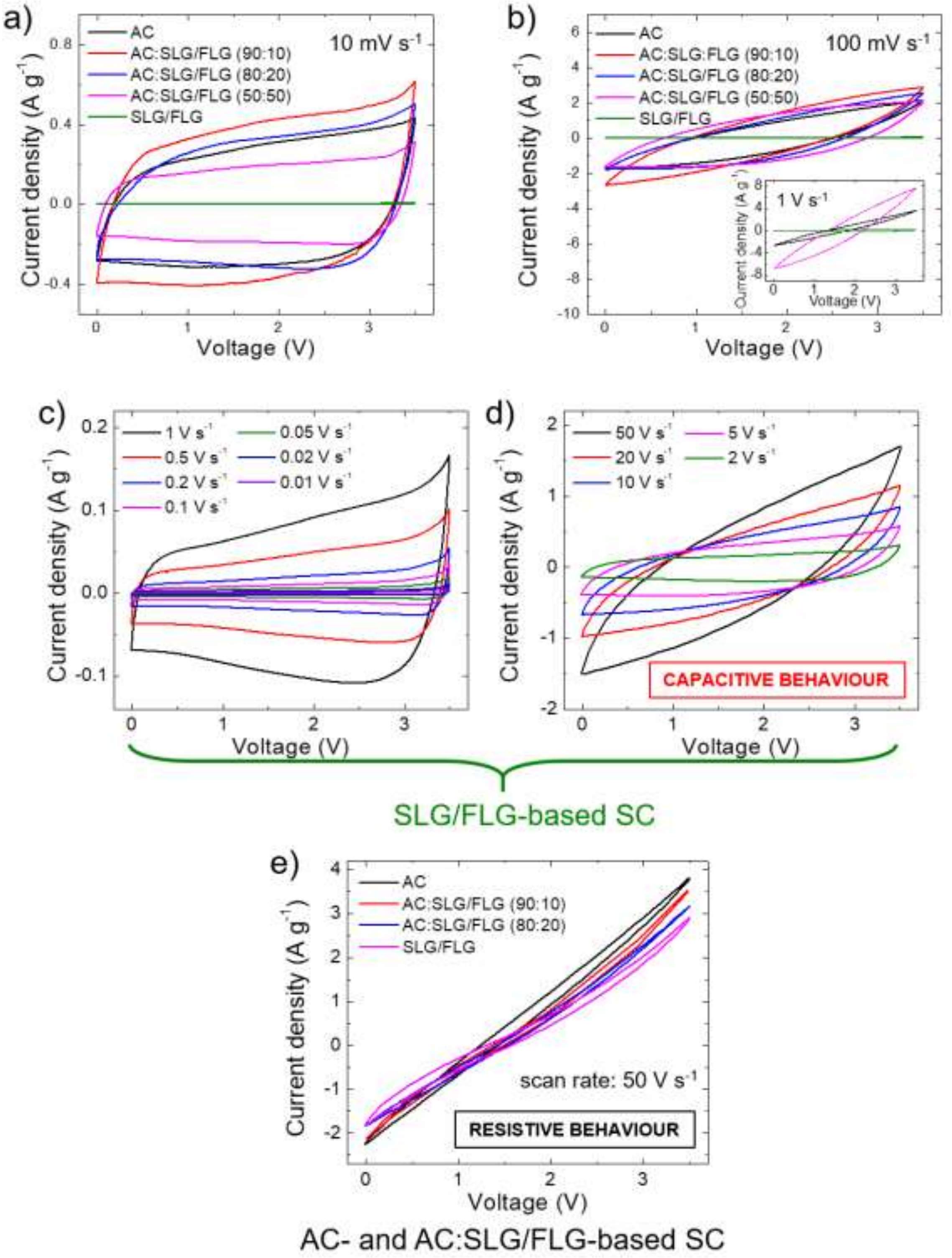

Figure 8: Cyclic voltammograms of the EDLCs. (a,b) CV curves of the produced EDLCs at voltage scan rates of 10 mV s^{-1} (a) and 100 mV s^{-1} (b). The inset to panel (b) shows the CV curves of AC-, AC:SLG/FLG (50:50)- and SLG/FLG-based EDLCs at a voltage scan rate of 1 V s^{-1}. (c, d) CV curves of SLG/FLG-based EDLCs at various voltage scan rates (ranging between 0.01 and 1 V s^{-1} (c), 2 and 50 V s^{-1} (d)). (e) CV curves of AC:SLG/FLG-based EDLCs at a scan rate of 50 V s^{-1}.

The nearly-rectangular CV shapes and the absence of current redox peaks indicate that the electrodes show double-layer capacitive behaviour in the corresponding voltage ranges.[23,185] These data prove the absence of graphene oxide, which typically result in pseudo-capacitance contribution.[187–189,] Although graphene oxide can enhance the capacitance, pseudo-capacitance related reaction can limit the rate capability and cycling life of the EDLCs, hindering practical high-power applications.[190,191] The voltage range of 3.5 V was selected as the upper limit operative voltage (V^+) of PC,[116] at which parasitic redox reaction caused by electrolyte decomposition starts to occur,[114,192] as shown by the whisker-like features in CV curve at voltage scan rate of 10 mV s^{-1} (**figure 8a**). At such voltage scan rate, AC:SLG/FLG (90:10)- and AC:SLG/FLG (80:20)-based EDLCs show current density (0.41 A g^{-1} and 0.33 A g^{-1} at $V^+/2$, respectively) higher than those of AC-based reference (0.29 A g^{-1} at $V^+/2$). In the AC:SLG/FLG-based EDLCs, the current density decreases by increasing the weight content of SLG/FLG in the active materials, reaching the minimum values for the SLG/FLG-based EDLC (<0.01 A g^{-1} at $V^+/2$). This behaviour can be attributed to the restacking[68–70] and the in-plane orientation (perpendicular to the current collector)[71,72] of the SLG/FLG flakes in absence of any spacer components.[174–176] At 100 mV s^{-1}, the shapes of the CV curves become biconvex (lens-shaped), especially for AC and AC:SLG/FLG (90:10)-based EDLCs (**figure 8b**). This means that only a fraction of capacitive states is retained with the applied voltage. In fact, the high mass loading of the electrodes (~10 mg cm^{-2}), as required for effective packaging in commercial-like EDLCs, results in “areal” current density of tens mA cm^{-2}. In particular, at high voltage scan rate (*e.g.*, 1 V s^{-1}, inset panel to **figure 8b**), this causes the emergence of resistive voltage drops originated by the electrolyte resistance across the nano/mesoporous active material films,[185,193–196] as well as the electrical resistance of the metal collectors and active films.[185,193] However, the deviation from the ideal rectangular CV shape is reduced with increasing the weight content of SLG/FLG in the active materials of the EDLCs. Noteworthy, SLG/FLG-based EDLC still exhibits a capacitive behaviour at a voltage scan rate up to 50 V s^{-1} (**figure 8c,d**), where both AC- and AC:SLG/FLG-based EDLCs display resistive performance (**figure 8e**). **Figure 9a,b** display the CD curves obtained for the EDLCs at a current density of 0.1 A g^{-1} and 1 A g^{-1}, respectively. At 0.1 A g^{-1} (**figure 9a**), the CD curves have a triangular-like shape, which is an indication of the double-layer capacitive behaviour of the EDLCs.[187–189] The AC:SLG/FLG- (90:10) and AC:SLG/FLG (80:20)-based EDLCs have shown higher t_d (1735.8 s and 1462.6 s, respectively) compared to AC-based reference (1354.2 s).

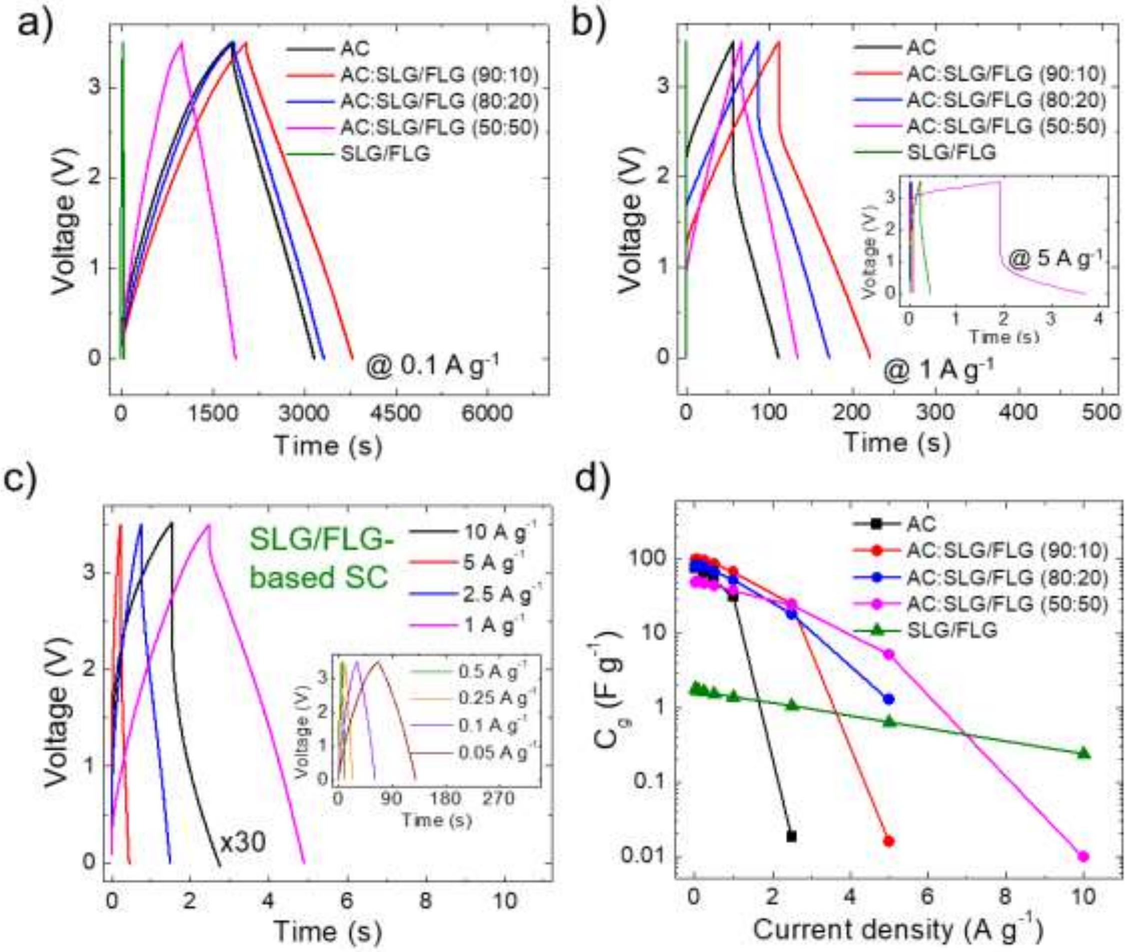

Figure 9: Electrochemical characterization of the EDLCs. (a,b) CD curves of the as-produced EDLCs at current densities of 0.1 A g^{-1} (a) and 1 A g^{-1} (b). The inset panel (b) shows the CD curves of AC:SLG/FLG-, and SLG/FLG-based EDLCs at a current density of 5 A g^{-1}. (c) CD curves of SLG/FLG-based EDLCs at various current densities (ranging between 1 and 10 A g^{-1}). The inset panel (c) shows the CD curves at low current densities (ranging from 0.05 and 0.5 A g^{-1}). (d) Plot of electrode C_g *vs.* current densities, as derived by CD measurements of the EDLCs.

By increasing the weight content of SLG/FLG in the EDLC active material, the t_d decreases to the minimum values recorded for the SLG/FLG-based EDLCs (867.2 s). At 1 A g^{-1} (**figure 9b**), CD curves show a resistive voltage drop at the half-cycle, as originating by both the electrolyte resistance across the nano/mesoporous active material films,[185,193–196] and the electrical resistance of the metal collectors and active films.[185,193] By increasing the current density at 5 A g^{-1} (inset panel to **figure 9b**), the voltage drops increase up to values superior to V^+ for AC-, AC:SLG/FLG (90:10)-, AC:SLG/FLG

(80:20)-based EDLCs, which start to exhibit resistive behaviour. Differently, both AC:SLG/FLG (50:50)- and SLG/FLG -based EDLCs still show a capacitive behaviour. In particular, SLG/FLG-based EDLC exhibits nearly triangular-shaped CD curves at a current density as high as 10 A g^{-1} (**figure 9c**).

Figure 9d shows the C_g of the EDLCs electrodes calculated from the CD curve at current densities ranging from 0.05 to 10 A g^{-1}. These data indicate that the use of SLG/FLG flakes into AC films increase both the maximum C_g (99.2 F g^{-1} for AC:SLG/FLG (90:10)-based SC) and the rate capability of the EDLCs (up to 5 and 10 A g^{-1} for AC:SLG/FLG (50:50)- and SLG/FLG-based EDLCs, respectively) compared to AC-based EDLC (C_g = 76.7 F g^{-1} and rate capability up to 2.5 A g^{-1}). As shown in **figure 10a**, C_g values ($C_{g\ \mathrm{AC:SLG/FLG\ (90:10)}} > C_{g\ \mathrm{AC}} > C_{g\ \mathrm{AC:SLG/FLG\ (80:20)}} > C_{g\ \mathrm{AC:SLG/FLG\ (50:50)}} > C_{g\ \mathrm{SLG/FLG}}$) positively correlate with the electrode SSAs calculated by BET analysis ($\mathrm{SSA}_{\mathrm{AC:SLG/FLG\ (90:10)}} > \mathrm{SSA}_{\mathrm{AC}} > \mathrm{SSA}_{\mathrm{AC/SLG:FLG\ (80:20)}} > \mathrm{SSA}_{\mathrm{AC:SLG/FLG\ (50:50)}} > \mathrm{SSA}_{\mathrm{SLG/FLG}}$). In these conditions, the electrolyte transport kinetics likely affords the ions to access totally into the surface area of the electrodes. The capacitance trend is severely altered with increasing the current density (**figure 10b**) until to be completely overturned at 10 A g^{-1}, at which the SLG/FLG-based EDLC shows the maximum C_g value (0.24 F g^{-1}). At 5 A g^{-1}, the AC:SLG/FLG (50:50)-based electrode exhibits a C_g >5 F g^{-1}, while, on the contrary, the other hybrid EDLCs display resistive behaviour. The large mesoporosity of SLG/FLG-based EDLC (**figure 7o**) can be the origin of its excellent rate capability. However, for the AC:SLG/FLG-based electrodes, the trend shown in **figure 10b** cannot be attributed to porosity (and/or morphology) of EDLC electrodes, since it does not show any correlation between C_g and D90 (**figure 10c**). For hybrid electrode-based EDLCs, **figure 10d** shows that C_g tends to positively correlate with the SLG/FLG weight content in the active materials when high current density is applied (≥ 5 A g^{-1}). Consequently, we first attributed the high-rate capability of the SLG/FLG-based EDLCs to the tribology properties of the SLG/FLG flakes (which positively correlate by their weight content in the active material), which act as "*ion slides*" for the case of 1 M $TEABF_4$ in PC. This agrees with the analysis of the LFM measurements (**figure 6d,e**), showing an almost unchanged F_F on SLG/FLG flakes with and without electrolyte in the solvent.

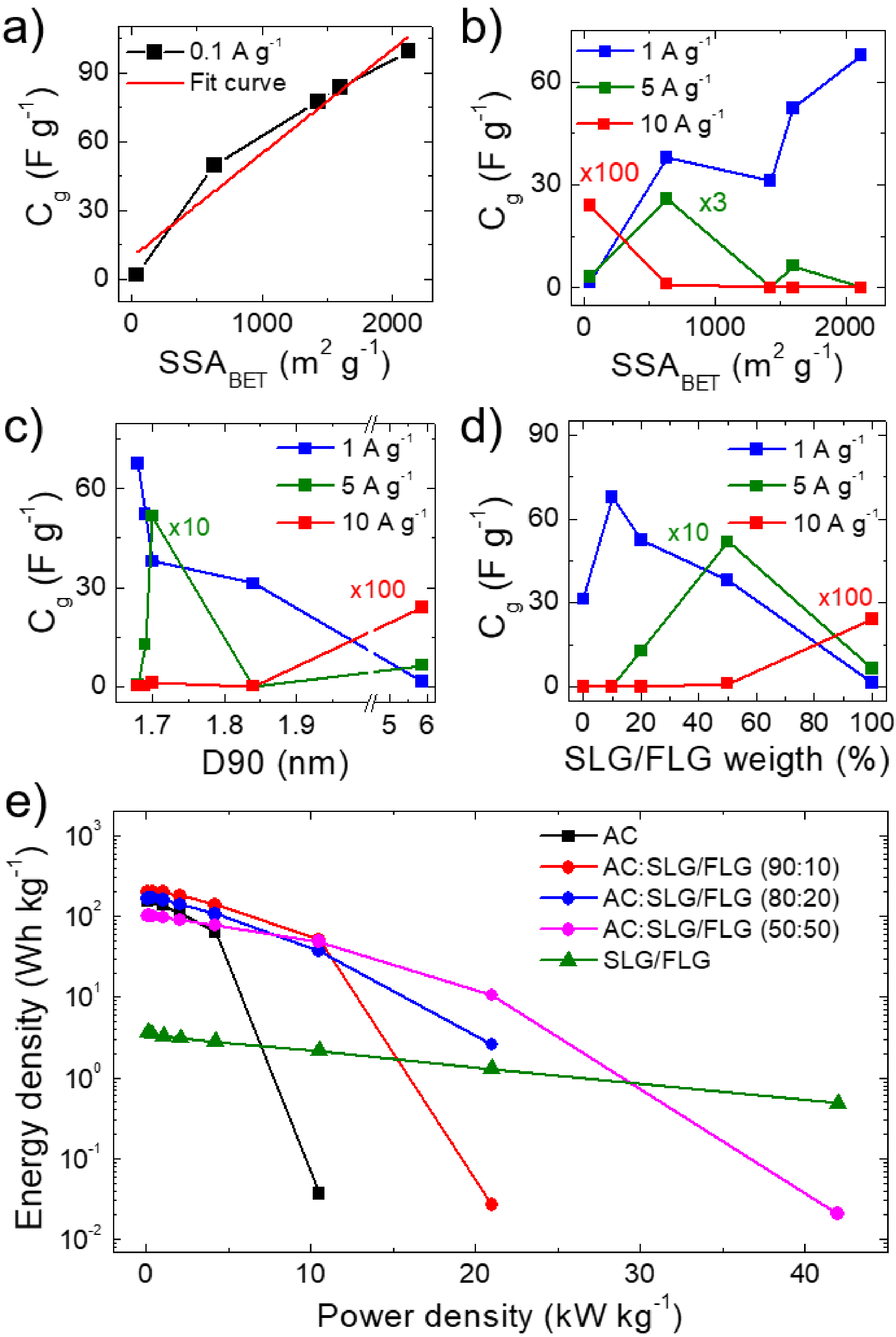

Figure 10: Performance analysis of the EDLCs. (a,b) Dependence of the electrode C_g on the SSA_{BET} of the EDLC electrodes at CD current densities of 0.1 A g^{-1} (a), and 1, 5 and 10 A g^{-1} (b). (c) Dependence of the electrode C_g on the D90 of the EDLCs electrodes at CD current densities of 1, 5, 10 A g^{-1}. (d) Dependence of the electrode C_g on the SLG/FLG weight content in the active

material of the EDLC electrodes at CD current densities of 1, 5, 10 A g^{-1}. (e) Ragone (energy density *vs.* power density) plots of the EDLCs.

The Ragone plots obtained for the EDLC electrodes under study are shown in **figure 10e**, revealing that the use of SLG/FLG enables the EDLCs to operate at high power density (>20 kW kg^{-1}), while retaining their energy density. For example, AC:SLG/FLG (50:50)-based EDLC exhibited an energy density >10 Wh kg^{-1} for power density >20 kW kg^{-1}, while AC-based EDLCs have shown only resistive behaviour. Furthermore, SLG/FLG-based EDLC achieved an energy density of ~0.5 Wh kg^{-1} at power density >40 kW kg^{-1}. Once again, it is important to evidence that these results have been obtained with EDLCs adopting commercial-like active material mass loading of ~10 mg cm^{-2}, which account for about 30% of the total mass of the packaged commercial EC.[148] Therefore, as commented in ref.[148], our data provide a true performance evaluation of EDLCs used for energy storage applications. The comparison of our data with relevant literature on EDLCs is not straightforward since the latter often investigate EDLCs adopting active material mass loadings one or two orders of magnitude lower than 10 mg cm^{-2}, and therefore their gravimetric performance could be strongly overestimated in commercial-like device architectures.[148]

HIGH-AREAL PERFORMANCE FLEXIBLE SUPERCAPACITORS

INTRODUCTION

In the previous sections it was thoroughly shown that AC-based electrodes exhibit valuable and interesting properties in the field of supercapacitors. The use of graphene can improve some of these features (as in the case of the nanotribological properties). However, in some cases AC-based technologies do not fulfil some practical requirements. This is the case for the fabrication of electrodes with high areal capacitance (C_{areal}), along with high power/energy densities, for applications with limited usable area including portable wearable electronics (available space in the human body is ~1.5 m^2)[6,197,198] as well as micro-electronics.[199–201] In fact, the slurry method of AC-based pastes hinders the deposition of active materials mass loadings to ~10 mg cm^{-2}, because for higher values the electrodes become brittle.[35] This drawback limits the energy density and consequently the weight packaging of the resulting devices,[35] which are not intended as flexible energy supply.[59] For this reason, there is the need for alternative active materials for flexible and high performing energy storage systems. In this chapter, the production and performance of WJM–G/SDWCNTs electrodes for EDLCs are discussed.

ELECTRODES CHARACTERIZATION AND SUPERCAPACITORS FABRICATION

By controlling the volume of the deposited dispersion, WJM–G/SDWCNTs electrodes were produced with active material mass loading ranging from ~1.6 to ~30 mg cm^{-2}. Electrodes based on WJM–G (average active mass loading of ~11.4 mg cm^{-2}) were also produced as reference. In **Figure 11a** a picture of a representative WJM–G/SDWCNTs electrode is shown.

X-ray photoemission spectroscopy (XPS) measurements were carried out to ascertain the C atomic network and the chemical quality of the WJM–G films. The C 1s core-level XPS spectrum (**figure 11b**) shows an asymmetric peak-shape centred at 284.5 eV, corresponding to C sp^2, typical of graphitic like compounds, together with the π-π* transition at 290.9 eV. Graphitic carbon accounts for 85.4% of the total carbon content of the sample. Defect- and oxygen-related components, *i.e.*, C-O (at 285.9 eV), C=O (at 287.1 eV) and O-C=O (at 288.9 eV) marginally contribute to the spectrum (percentage content %c = 5.0%, 5.7% and 3.9%, respectively). The N 1s XPS spectrum (inset of **figure 11b**) was acquired to evaluate the NMP residual into electrodes after IPA-based washing procedure. In fact, the band peaking at ~400.0 eV is associated to the amide groups (-N-(C=O)),[138,202] which are signatures of the presence of NMP. However, the elemental analysis shows an overall %c of N ~0.1%, thus indicating that NMP was almost completely removed by IPA-based washing of the electrodes.

The morphology of the electrodes was assessed by performing SEM characterization. **Figure 11c** shows a SEM image of a representative WJM–G electrode, displaying the laminar structure of the WJM–G flakes. **Figure 11d** displays a SEM image of a representative hybrid electrode, where WJM–G flakes are wrapped and linked by SDWCNTs.

Symmetric EDLCs were produced by assembling two WJM–G/SDWCNTs electrodes with the same active material mass loading in coin cells configuration. The latter was chosen since it is a benchmark methodology providing a reliable assembly of EDLCs.[203] Briefly, coin cells were produced using CR2032 cases, a glass fibre separator and 1 M $TEABF_4$ in PC as the electrolyte (see Experimental section for further details).

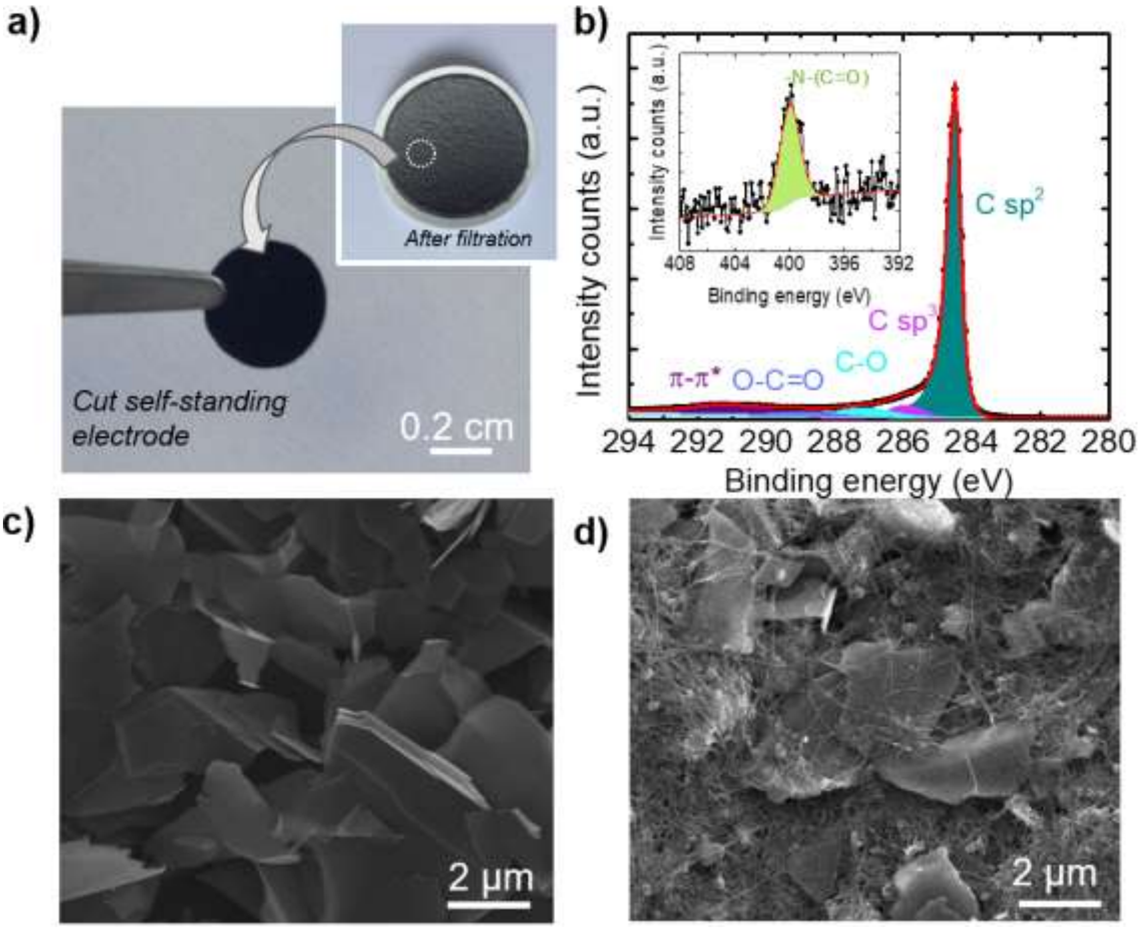

Figure 11 Chemical and morphological characterization of the as-produced EDLCs electrodes. (a) Photograph showing the deposited material on the membrane together with a representative picture of a self-standing WJM–G/SDWCNTs electrode. (b) C 1s and N 1s core-level (inset) XPS spectra of the WJM–G electrode, together with the corresponding deconvolution. (c, d) SEM images of representative WJM–G (c) and WJM–G/SDWCNTs (d) electrodes.

ELECTROCHEMICAL CHARACTERIZATION

The electrochemical performance of WJM–G/SDWCNTs EDLCs were evaluated by CV (**figure 12**) and CD (**figure 13**) measurements. The evaluation of the C_{areal} of EDLCs was carried out from the CD measurements (**figure 13**) by using the equation:[185,204]

$$C_{areal} = \frac{|i| \cdot t_d}{A \cdot \Delta V} \quad (6)$$

In the previous equation, $|i|$ is the module of the applied current (i), t_d is the discharge time, A is the geometrical area of the electrodes and ΔV is the voltage window of the measurements. All the electrochemical characterizations were performed in the voltage window 0 – 3.5 V in order to avoid parasitic chemical reactions (breakdown voltage of $TEABF_4$/PC >3.5 V).[116] **Figure 12a** shows the comparison between the CV curves of a hybrid WJM–G/SDWCNTs EDLC and a reference WJM–G EDLC with similar electrode mass loading (13.5 and 11.4 mg cm^{-2}, respectively). Both the CV curves show a nearly rectangular shape, typical of electrochemical double layer behaviour.[23,185,205] The area of the CV curve can be quantitatively correlated with the C_{areal} of the EDLCs.[204] The area of the CV curve of the hybrid WJM–G/SDWCNTs EDLC increases by 1301% compared to that of WJM–G EDLC. This is attributed to the presence of SDWCNTs as spacers between WJM–G flakes, which tend to restack in WJM–G EDLC [65,70,73,206] causing a decrease of the EDLC capacitance

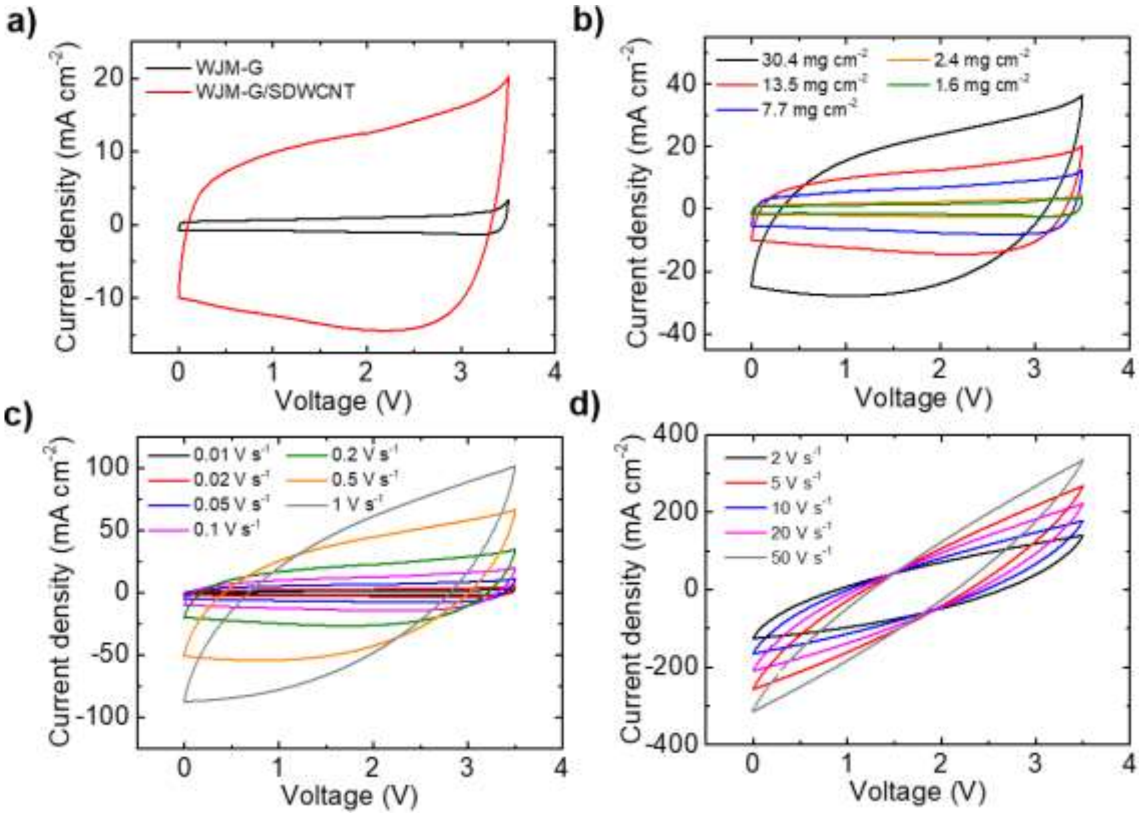

Figure 12: Cyclic voltammetry characterization of the produced EDLCs. (a) Comparison between the CV curves of WJM–G EDLC (electrode active material mass loading of 11.4 mg cm^{-2}) and WJM–G/SDWCNTs EDLC (electrode active material mass loading of 13.5 mg cm^{-2}) at a voltage scan rate of 100 mV s^{-1}. (b) Comparison between the CV curves of WJM–G/SDWCNTs EDLCs with various electrode active material mass loadings (ranging from 1.6 to 30.3 mg cm^{-2}) at a voltage scan rate of 100 mV s^{-1}. (c, d) CV curves of the WJM–G/SDWCNTs EDLC with electrode active material mass loading of 13.5 mg cm^{-2}, at scan rates ranging from 0.01 V s^{-1} to 1 V s^{-1} (c) and from 2 to 50 V s^{-1} (d).

Figure 12b shows the CV curves of WJM–G/SDWCNTs EDLCs with various electrode active material mass loadings (ranging from 1.6 to 30.3 mg cm^{-2}) at a voltage scan rate of 100 mV s^{-1}. The current densities increase with increasing the electrode active material mass loading (so higher active material surface area is available) and, consequently, the C_{areal} which is quantitatively correlated to the area of the CV curves, rises.[204] Cyclic voltammetry measurements at voltage scan rates ranging from 0.01 to 50 V s^{-1} were performed to evaluate the rate capability of the EDLCs. **Figure 12c,d** shows such CV curves for the WJM–G/SDWCNTs EDLC with electrode active material mass loading of 13.5 mg cm^{-2}. Notably, the WJM–G/SDWCNTs EDLC still exhibits a capacitive behaviour even at scan rates as high as 50 V s^{-1}. The biconvex lens-shape of the CV curve for the highest voltage scan rate can be ascribed to the equivalent series resistance of the EDLC at current densities higher than tens of mA cm^{-2}. This contribution is associated to the electrolyte resistance of the ions into the porous active material films,[185,193–196] as well as the electrical resistance of the latter.[185,193] **Figure 13a** shows the comparison between the CD curves of WJM–G and WJM–G/SDWCNTs with similar electrode active material mass loading (11.4 and 13.5 mg cm^{-2} respectively). Both the CD curves display nearly triangular shapes in the considered voltage window, confirming their electrochemical double layer capacitive behaviour,[23,185,205] in agreement with CV analysis. Although the WJM–G/SDWCNTs EDLC was tested at a current density 18% higher than the one used for the WJM–G EDLC, it shows a CD curve that lasts >26-fold time that of the WJM–G-based one. This reflects the superior C_{areal} (129.6 mF cm^{-2}) of the WJM–G/SDWCNTs EDLC compared to that of WJM–G EDLC (4.6 mF cm^{-2}) (see **figure 13b** for the C_{areal} comparison). **Figure 13c** reports the CD curves of the WJM–G/SDWCNTs EDLC with electrode active material mass loading of 13.5 mg cm^{-2} at various current densities applied (ranging from 0.3 to 6.8 mA cm^{-2}). The CD curves of the same electrode at applied current densities ranging from 13.5 to 135.4 mA cm^{-2} are reported in **figure 13d**. **Figure 13e** shows the comparison between the CD curves of the WJM–G/SDWCNTs EDLCs with various electrode active material mass loadings (ranging from 1.6 to 30.4 mg cm^{-2}) at comparable applied current densities. These results demonstrate that the CD curves broaden in time as the mass loading increases, increasing the C_{areal} from 15.6 mF cm^{-2} to

313.5 mF cm^{-2} for the EDLC with electrode active material mass loading of 1.6 mg cm^{-2} and 30.4 mg cm^{-2}, respectively. **Figure 13f** shows the dependence of the C_{areal} of the WJM–G/SDWCNTs EDLCs on the applied current densities. The EDLCs having the electrode with the highest active material mass loading (30.4 mg cm^{-2}) achieve a C_{areal} of 317 mF cm^{-2} (*i.e.*, electrode C_{areal} of 634 mF cm^{-2}) at a current density of 0.8 mA cm^{-2}. Interestingly, at a current density of 304.1 mA cm^{-2}, this EDLC still exhibits a remarkable value of 7.1 mF cm^{-2}. At lower electrode active material mass loading, the rate capability progressively increases, showing a maximum C_{areal} retention of 79% for the EDLC with electrode active material mass loading of 1.6 mg cm^{-2}. As shown in **figure 14a**, the WJM–G/SDWCNTs EDLC shows excellent cycling stability (electrode active material mass loading of 13.5 mg cm^{-2}). In fact, stable electrode C_{areal} of ~124 mF cm^{-2} (EDLC energy density of ~106 μWh cm^{-2}) was measured over 10000 CD cycles at a current density of 7.7 mA cm^{-2}, corresponding to a EDLC power density of 235 mW cm^{-2}. **Figure 14b** shows the Ragone plot obtained for the WJM–G/SDWCNTs EDLCs with various electrode active material mass loadings. Noteworthy, these EDLCs exhibit energy and power densities ranging from 28.8 to 539 μWh cm^{-2} and from 71.4 μW cm^{-2} to 532 mW cm^{-2}, respectively.

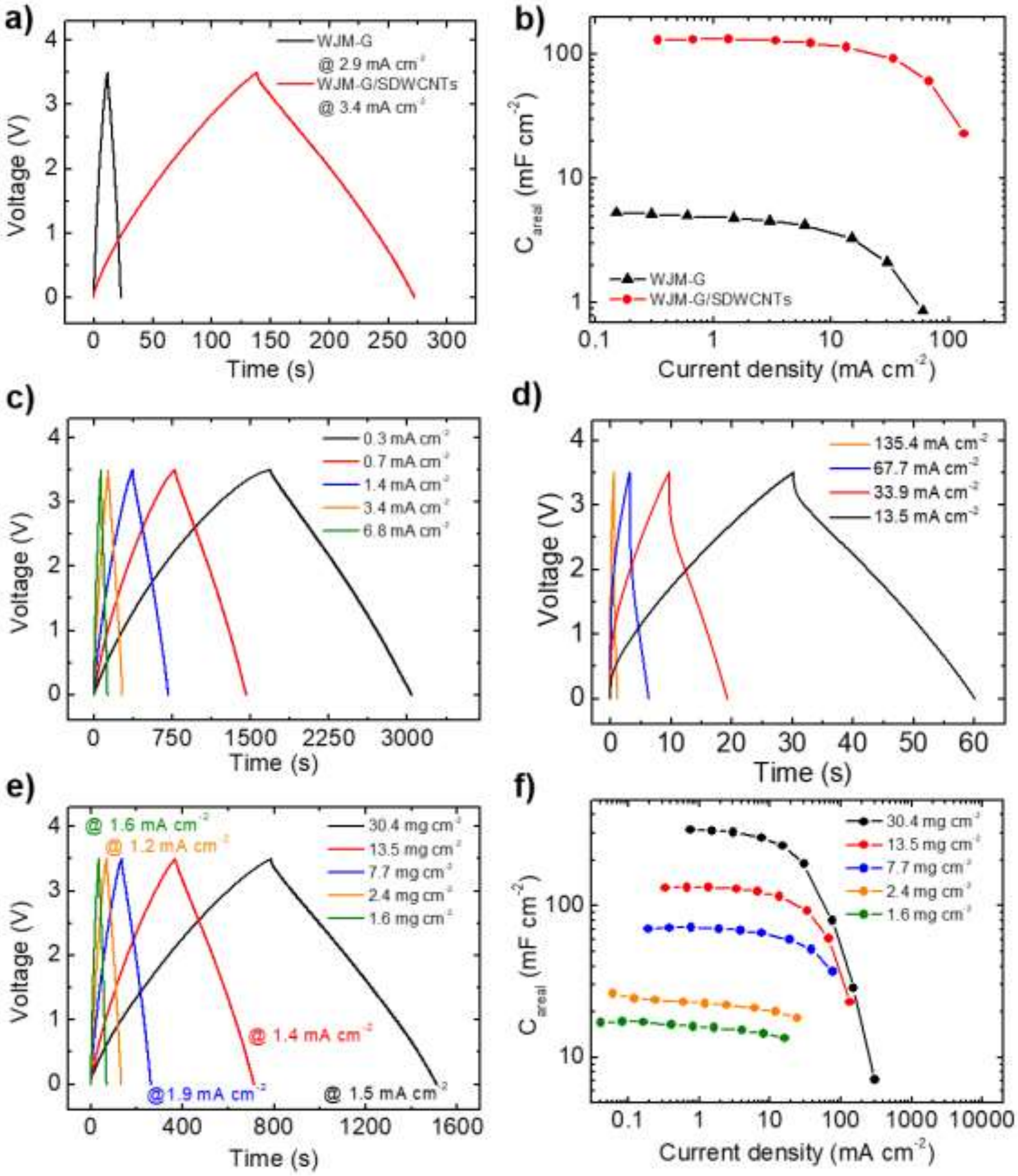

Figure 13: Galvanostatic charge/discharge measurements of the as-produced EDLCs. (a) Comparison between the CD curves of the WJM–G EDLC (electrode active material mass loading of 11.4 mg cm^{-2}) and WJM–G/SDWCNTs EDLC (electrode active material mass loading of 13.5 mg cm^{-2}) at an applied current density of 2.9 mA cm^{-2} and 3.4 mA cm^{-2}. (b) Dependence of C_{areal}, calculated from CD curves, on the applied current density for the WJM–G and WJM–G/SDWCNTs EDLCs. (c) CD curves of the WJM–G/SDWCNTs EDLC (electrode active material mass loading of 13.5 mg cm^{-2}) at current densities ranging from 0.3 mA cm^{-2} to 6.8 mA cm^{-2}. (d) CD curves of WJM–G/SDWCNT EDLC (electrode active material mass loading of 13.5 mg cm^{-2}) at current densities ranging from 13.5 to 135.4 mA cm^{-2}. (e) Comparison between the CD curves of WJM–G/SDWCNTs EDLCs with different electrode active material mass loadings (ranging from 1.6 to 30.4 mg cm^{-2}), at comparable applied current densities. (f) Dependence of the calculated C_{areal} on the applied current density

for all the WJM–G/SDWCNTs EDLCs with different electrode active material mass loadings.

These values are competitive with those reported in relevant literature on EDLCs areal performances, including: aqueous electrolyte-based EDLCs [197,198,207–210], gel electrolyte-based EDLCs[211], porous silicon-based EDLCs [212,213] and graphene-based technologies [214–216]. Porous silicon-based EDLCs exhibit the highest energy densities among the reported results. However, the energy densities fade drastically with increasing the power densities (for example, in ref.[212] the starting energy density of ~1641 μWh cm^{-2} at ~1.3 $μWcm^{-2}$ reduces to ~184.2 μWh cm^{-2} at ~2.5 μW cm^{-2}). Similar trends are also observed in most of the other examples. Differently, WJM–G/SDWCNTs EDLCs show a similar energy density value over more than three orders of magnitude of power densities. For example, the EDLCs with electrode active material mass loading of 30.4 mg cm^{-2} exhibited an energy density of 539 μWh cm^{-2} at 1.3 mW cm^{-2} and 480 μWh cm^{-2} at 13.3 mW cm^{-2}, which correspond to an energy retention of 89%. The EDLC adopting an electrode active material mass loading of 2.4 mg cm^{-2} shows energy retention of 69% throughout power densities ranging from 0.1 to 42.5 mW cm^{-2}. The extraordinary areal performance expressed by WJM–G/SDWCNTs EDLCs can positively influence the EDLC packaging design and weight. In fact, in order to achieve the same areal performance of a single WJM–G/SDWCNTs EDLC presented by our work, many EDLCs reported in the literature have to be connected in parallel, complicating the overall EDLC unit architecture. For example, the WJM–G/SDWCNTs EDLC with electrode active material mass loading of 30.4 mg cm^{-2} exhibits a maximal energy density of 539 μWh cm^{-2}, which means that 2 EDLCs from ref.[215] (367 μWh cm^{-2}), 3 EDLCs from ref.[198] (240 μWh cm^{-2}) and

19 EDLCs from ref.[216] (29 μWh cm^{-2}) are needed to achieve the same performance, thus resulting in complicated and/or bulky architectures. This consideration is of paramount importance when dealing with wearable applications, where the surface available from a human body is limited (~1.5 m^2)[6], and devices should not be too big and/or heavy to prevent adding uncomfortable burdens on the body.

To prove the applicability of WJM–G/SDWCNTs EDLCs for wearable electronics, flexible EDLCs in form of pouch cells were also fabricated. In this case, a hydrogel-polymer electrolyte (*i.e.*, PVA doped with H_3PO_4) was used in order to eliminate the use of bulky and rigid encapsulation material to prevent the hazardous leakage of liquid electrolyte.[217–219] Moreover, among the hydrogel-polymer electrolytes, PVA/H_3PO_4 mixture has been identified as one of the best quasi-solid-state electrolytes for graphene-based EDLCs.[220–222] Silicon-adhesive Kapton® tape and PVA/H_3PO_4-soaked PVDF membrane were used as encapsulant and separator, respectively. Large-area and stacked EDLCs were also fabricated to be exposed as industrial product prototype at Mobile World Congress (2018) held in Barcelona[223] (**figure 14c**, specification in Experimental section). **Figure 14d** shows the CV curve of a quasi-solid-state WJM–G/SDWCNTs EDLC (electrode active material mass loading of 5 mg cm^{-2}) at various voltage scan rate. The cell voltage window was 0 – 0.8 V in order to avoid electrochemical degradation of the electrolyte, in agreement with previous studies.[220–222] The current increases linearly with the voltage scan rate, showing a capacitive behaviour up to 2 V s^{-1} (inset panel), while beyond this value the electrolyte resistance (~5 Ω) causes resistive electrochemical behaviour. **Figure 14e** reports the CD curves at different current density, together with the corresponding C_{areal} values (inset panel). At the lowest current density of 0.3 mA cm^{-2}, the EDLC shows a C_{areal} as high as 67.1 mF cm^{-2} (electrode C_{areal} of 134.2 mF cm^{-2}), corresponding to an energy density of 6 μWh cm^{-2} at power density of 100 μW cm^{-2}. The capacitance behaviour is retained up to current density of 25 mA cm^{-2} (C_{areal} = 15.9 mF cm^{-2}). Beyond this current density, the excessive resistance of the electrolyte causes voltage losses comparable or superior to the operating voltage range of the solid-state EDLCs (0.8 V). **Figure 14f** shows the capacitance retention plots over bending cycles adopting a bending radius (R) of 1 cm. The device shows an outstanding performance stability over more than 500 bending cycles. The devices were also tested at different folding states, corresponding to the folding angles (θ) of 0° (unbent states), 90° and 180° (inset panel). After folding at both these θ values, the device exhibited a 26% increase of the C_{areal}, which can be tentatively attributed to a favourable mesoscopic rearrangement of the active materials in the folded electrodes.[224]

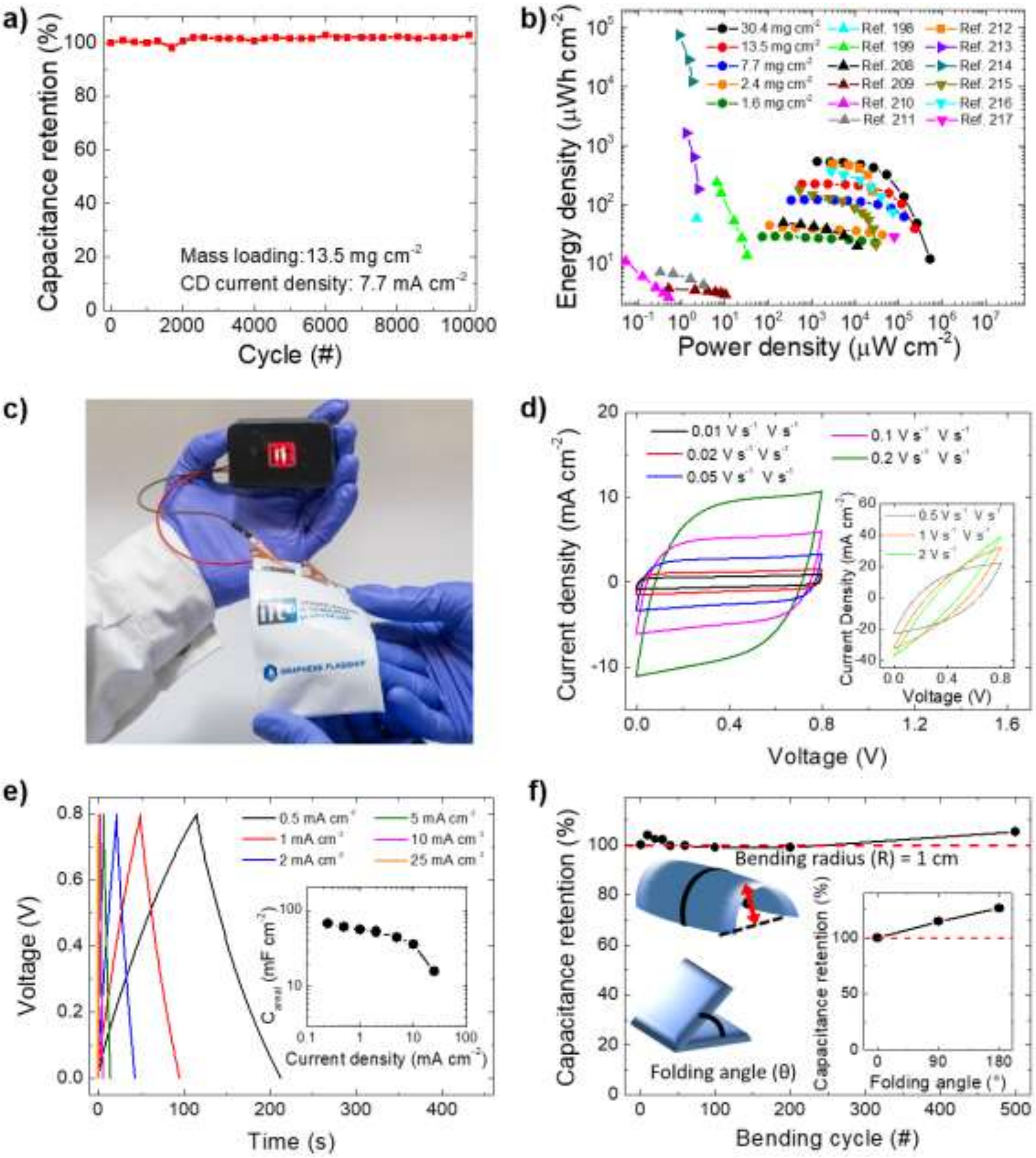

Figure 14: Characterization of flexible quasi-solid-state WJM–G/SDWCNTs EDLCs. (a) Capacitance retention of WJM–G/SDWCNTs EDLC with electrode active material mass loading of 13.5 mg cm^{-2} over 10000 CD cycles at an applied current density of 7.7 mA cm^{-2}. (b) Comparison between the Ragone plot of the WJM–G/SDWCNTs EDLCs (for all investigated electrode active material mass loadings) and some relevant EDLCs reported in literature (▲: ref.[210], data calculated from reported thickness; ref.[197,198,207–210]. ■: ref.[211]. ▶: ref.[212,213]. ▼: ref.[214–216], data calculated from the reported mass loadings/thicknesses). (c) Digital photograph of a flexible solid-state WJM–G/SDWCNTs EDCLs industrial prototype exhibited ad Mobile World Congress 2018 held in Barcelona. The electrodes were manually bended in order to show their mechanical flexibility. (d) CV curves of the WJM–G/SDWCNTs EDLC with electrode active material mass loading of 13.5 mg cm^{-2}, at scan rates ranging from 0.01 V s^{-1} to 2 V s^{-1}. (e) CD curves of the WJM–G/SDWCNTs EDLC with electrode active material mass loading of 13.5 mg cm^{-2} electrode, at current densities ranging from 0.5 mA cm^{-2}

to 25 mA cm^{-2}. The inset panel shows the dependence of the calculated C_{areal} on the applied current density. (f) Capacitance retention of the solid-state WJM–G/SDWCNTs EDLC over 500 bending at R of 1. The inset panel shows the capacitance retention of folded solid-state WJM–G/SDWCNTs EDLC at θ of 0°, 90° and 180°.

EXPERIMENTAL SECTION

ATOMIC FORCE MICROSCOPY

A NanoWizard III AFM system (JPK Instruments, Berlin) in intermittent contact mode was used for the AFM measurements. PPP-NCHR cantilevers (Nanosensors, USA) with a nominal tip diameter of 10 nm and a drive frequency of ~320 kHz were used. AFM images were collected with a working set point above 70% of the free oscillation amplitude and a scan rate of 0.7 Hz. The images were collected on an area of 5×5 μm^2 and have a resolution of 512×512 pixels and the corresponding height profiles were analysed with the JPK Data Processing software (JPK Instruments, Germany). A statistical analysis on 90 flakes was carried out on both sets of measurements and the data fitted with a lognormal distribution, which is an established statistic function used for fragmented systems.[225] The statistical analysis was carried out by using Origin 9.1 software. The AFM characterization was performed on drop-casted 1:30 diluted WJM–Graphene dispersion in NMP onto freshly-cleaved mica sheets (G250-1, Agar Scientific Ltd., Essex, U.K.) and dried under vacuum.

TRANSMISSION ELECTRON MICROSCOPY

Transmission electron microscopy images were taken with a JEM 1011 (JEOL) TEM (thermionic W filament), operating at 100 kV. Morphological and statistical analysis was carried out by using ImageJ software (NIH)[226] and OriginPro 9.1 software (OriginLab)[227], respectively. The samples for the TEM measurements were prepared by drop casting 1:50 diluted WJM-produced SLG/FLG dispersion in NMP onto ultrathin C-film on holey carbon 400 mesh Cu grids (Ted Pella Inc.). The grids were stored under vacuum at room temperature to remove the solvent residues.

SCANNING ELECTRON MICROSCOPY

The as-prepared electrodes were characterized by means of SEM using a Helios Nanolab® 600 DualBeam microscope (FEI Company) and 5kV and 0.2 nA as measurement conditions. For the cross-section imaging, the electrodes were cut with a scalpel.

SPECIFIC SURFACE AREA MEASUREMENTS

Specific surface area and pore size distribution measurements of SC electrodes were carried out in Autosorb-iQ (Quantachrome) by Kr physisorption at temperatures of 77 and 87 K, respectively. The specific surface areas were calculated using the multipoint BET model,[163] considering equally spaced points in the P/P_0 range of 0.009 – 0.075. P_0 is the vapour pressure of Kr at 77 K, corresponding to 2.63 Torr.[164,165, 166,167] The pore size distribution was calculated by Kr(87) Thin Film Pore Size Method using NLDFT.[172,173] Before the measurements, the samples were degassed for 1 h at 60 °C under vacuum conditions to eliminate weakly adsorbed species.

Sheet resistance of the electrodes were measured by four-probe method[228] by using Jandel RM3000 Test Unit.

RAMAN SPECTROSCOPY

Raman characterization was carried out with a Renishaw microRaman invia 1000 using a 50× objective (numerical aperture of 0.75), with an excitation wavelength of 514.5 nm and an incident power on the samples of 5 mW. The samples were prepared by drop casting the 1:30 diluted WJM–Graphene dispersion in NMP onto a Si wafer covered with 300 nm thermally grown SiO_2 (LDB Technologies Ltd.). For each sample, 50 spectra were collected. OriginPro 2016 was used to perform the deconvolution and statistics.

X-RAY PHOTOELECTRON SPECTROSCOPY

The analysis were performed by using a Kratos Axis UltraDLD spectrometer on both WJM–G dispersion in NMP and WJM–G electrodes produced by vacuum filtration of the starting dispersion. For the former case, SLG/FLG dispersion in NMP was drop casted onto Au-coated silicon wafers. The sample was then dried at 200 °C overnight to remove solvent residuals. Both the set of XPS spectra were acquired using a monochromatic Al Kα source operating at 20 mA and 15 kV. High-resolution spectra of C 1s, N 1s and Au 4f peaks were collected at pass energy of 10 eV and energy step of 0.1 eV. Energy calibration was performed setting the Au $4f_{7/2}$ peak at 84.0 eV. Data analysis was carried out with CasaXPS software (version 2.3.17).

PREPARATION OF ELECTROLYTES

For liquid organic electrolyte, tetraethylammonium tetrafluoroborate (>99%, Sigma Aldrich®) (2.17 g) was dispersed into 10 mL of propylene carbonate (anhydrous, 99.7 %, Sigma Aldrich®) in Ar glove-box. The mixture was left under stirring until it becomes clear (ca. 2h), obtaining the electrolyte solution (1 M). The electrolyte was stored in an Ar glove-box for further use. For solid hydrogel-polymer electrolyte, 1 g of H_3PO_4 was added into 10 mL of deionized water, and then 1 g of PVA (molecular weight: 89 000 – 98 000, Sigma-Aldrich) was added. The whole mixture was heated to 80 °C under stirring until the solution became clear, obtaining H_3PO_4-doped PVA-based hydrogel-polymer electrolyte.

NANOTRIBIOLOGICAL MEASUREMENTS

The frictional behaviour of the SLG/FLG flakes and AC films, obtained by doctor blade deposition of concentrated WJM-produced SLG/FLG and AC dispersion in NMP, was evaluated both in PC with and without 1 M $TEABF_4$ by using a Nanowizard III (JPK Instruments, Germany). Lateral force microscopy measurements were performed by using a single beam silicon cantilever (CSC38, Micromasch) with a nominal spring constant of 0.09 N m^{-1} and a tip with typical radius of curvature of 8 nm. The actual spring constant of each cantilever was determined using the thermal noise method. To obtain LFM responses, at least 10 LFM response data were obtained scanning on 5 lines of 50 μm over the entire L range and acquiring 256 points per line at a scan rate of 25 μm s^{-1}. Measurements were repeated at 10 different locations.

ELECTROCHEMICAL CHARACTERIZATION

The electrochemical performance of the EDLCs was evaluated by cyclic voltammetry (CV) and galvanostatic charge-discharge (CD) measurements. Both analyses were performed by using a VMP3 electrochemical workstation (BioLogic Science Instruments) connected to a computer with the ECLab® software. Cyclic voltammetry and CD tests were carried out respectively at voltage scan rates ranging from 0.01 to 50 V s^{-1} and at current densities ranging from ~0.02 to ~152 mA cm^{-2}, depending on the device. The current densities were calculated by using the equation:

$$\mathrm{J} = \frac{|\mathrm{i}|}{\mathrm{A_e}} \tag{7}$$

Where |*i*| is the absolute value of the applied current and A_e is the surface of one electrode. The areal capacitances (C_{areal}) of the EDLCs (comprising two electrodes) were determined by using the equation:

$$C_{areal} = \frac{|i| \cdot t_d}{A_e \cdot \Delta V} \tag{8}$$

Where |*i*| is the absolute value of the applied current, t_d is the discharge time of the CD curve, ΔV is the potential window and A_e is the surface of the electrodes.

Energy density (E_d) and power densities (P_d) were calculated from:

$$E_d = \frac{1}{2} C_{areal} (\Delta V)^2 \tag{9}$$

$$P_d = \frac{E_d}{t_d} \tag{10}$$

COMMERCIAL PRODUCT PROTOTYPE FLEXIBLE EDLC

The prototype flexible EDLC (**figure 14a**) exposed at Mobile World Congress (2018) (Barcelona) was fabricated by using WJM–G/SDWCNTs electrodes (electrode active material mass loading of 20 mg cm^{-2}), a polyvinylidene fluoride (PVDF) membrane as separator, 10 µm-thick pyrolytic graphite paper (PGS, Panasonic) as current collectors and silicon-adhesive Kapton® tape (Dupont®, from Tesa) as encapsulant. The specification of the device are: capacitance of 2.3 F (electrode C_{areal} of 366 mF cm^{-2}), voltage window of 0–2.7 V, equivalent series resistance (*ESR*) <1 Ω, lifetime >10000 cycles.

CONCLUSIONS

This chapter reports the use graphene as active material for electrochemical double layer capacitors (EDLCs). Graphene flakes were produced in form of liquid dispersions by a high-throughput (Y_W ~100%, t_{1g} = 4.8 min, V_{1g} = 0.1 L) wet-jet milling (WJM) exfoliation of graphite in N-methyl-2-pyrrolidone (NMP). The as produced graphene flakes (WJM–G) consisted in single-/few-layer graphene (SLG/FLG) flakes and were used for two different projects.

In the first one, the incorporation of WJM–G into mesoporous activated carbon (AC) film impacts positively the electrochemical performance of commercial-like EDLCs (*i.e.*, EDLCs with high active material mass loading of the electrode, ~10 mg cm^{-2}). The reported results reveal that the nanotribological properties between electrolytes and the nanocarbons are pivotal to provide high-accessibility of the ions to mesoporous electrode films. In particular, it was shown that the ions of an established EDLCs electrolyte (*i.e.*, 1 M tetraethylammonium tetrafluoroborate –TEABF$_4$– in propylene carbonate –PC–) efficiently slide over the SLG/FLG flakes. Consequently, the incorporation of SLG/FLG in high-specific surface area (SSA) AC-based nanoporous structures enables the enhancement of the electrochemical performance of EDLCs. At a charge/discharge (CD) current density of 0.1 A g^{-1}, the EDLC based on AC:SLG/FLG (90:10) has shown a gravimetric capacitance (C_g) of 98.2 F g^{-1}, which is increased by almost 30% compared to that of the AC-based reference (76.8 F g^{-1}). Such SLG/FLG-induced improvements in the EDLCs performance have been explained by the increase of SSA after the SLG/FLG incorporation into the AC film. At higher CD current densities (>1 A g^{-1}), the AC-based reference displayed a resistive behaviour, while the AC:SLG/FLG-based EDLCs continued to exhibit capacitive performance. In particular, AC:SLG/FLG (50:50) still exhibited a C_g of 23.9 and 5.2 F g^{-1} at CD current densities as high as 2.5 and 5 A g^{-1}, respectively. Furthermore, SLG/FLG-based EDLCs have shown an optimal capacitive retention increasing the CD current densities up to 10 A g^{-1}. The optimal capacitive behaviour at high CD current densities (≥1 A g^{-1}) for SLG/FLG and AC:SLG/FLG-based electrodes has been attributed to the peculiar nanotribological properties of the electrolyte ions on the SLG/FLG flakes. The management of the nanotribological properties of both active materials and electrolytes can be a new paradigm to overcome the classic dichotomy of energy density and power density in EDLCs. In fact, the advantage of conceiving an efficient ion transport within high-SSA electrodes allows for ideal access of ions in both meso- and micro-porous, which is mandatory for ideal rate-independent high energy densities. Such rationale allowed the design of commercial-like SLG/FLG-based EDLCs with superior energy/power densities performance compared to the AC-based benchmark. The added-value of “graphene flakes” can readily impact on the market since all the results here shown have been obtained with commercially available AC, scalable production of SLG/FLG flakes (i.e., by using WJM–G), and industrial-like manufacturing of EDLCs.

The second project concerns the fabrication and characterization of hybrid graphene/carbon nanotube EDLCs. The WJM–G dispersion was mixed with that of de-bundled commercial single/double walled carbon nanotubes (SDWCNTs) in a material weight ratio of 1:1. The SDWCNTs effectively acted as spacers between the WJM–G, avoiding the re-stacking of the latter during film deposition. Hybrid

WJM–G/SDWCNTs electrodes were obtained by depositing the as-produced dispersion through vacuum filtration on nylon membranes. 2-propanol-based washing removes NMP residuals, while subsequent drying of the electrode at room temperature causes the peel-off of the WJM–G/SDWCNTs films, resulting in self-standing, binder-free electrodes. By controlling the volume of the deposited dispersion, electrodes with active material mass loading as high as ~30 mg cm^{-2} have been demonstrated. Symmetric WJM–G/SDWCNTs ECDLs were assembled in coin cells by using an organic electrolyte (1 M $TEABF_4$ in PC), exhibiting an areal capacitance (C_{areal}) as high as ~317 mF cm^{-2}, an energy density of 539 µWh cm^{-2} at 1.3 mW cm^{-2} and outstanding rate-capability (power densities up to 532 mW cm^{-2}). By using polymer gel electrolyte, solid-state WJM–G/SDWCNTs EDCLs have been fabricated, showing remarkable mechanical flexibility under bending cycling (500 cycles at bending radius of 1 cm) and folding (folding angle of 90° and 180°). These outcomes are competitive with respect to existing technologies developed for wearable electronics. The combination of industrial-like production of active materials, facile fabrication of solution-processed EDLCs, and ultrahigh-areal performance of the obtained EDLCs are highly promising for novel advanced EDLCs design.

REFERENCES

1. Guney, M. S. & Tepe, Y. Classification and assessment of energy storage systems. *Renew. Sustain. Energy Rev.* **75**, 1187–1197 (2017).
2. Bruce, P. G., Freunberger, S. A., Hardwick, L. J. & Tarascon, J. M. LigO2and LigS batteries with high energy storage. *Nat. Mater.* **11**, 19–29 (2012).
3. González, A., Goikolea, E., Barrena, J. A. & Mysyk, R. Review on supercapacitors: Technologies and materials. *Renew. Sustain. Energy Rev.* **58**, 1189–1206 (2016).
4. Simon, P. & Gogotsi, Y. Materials for electrochemical capacitors. *Nat. Mater.* **7**, 845–854 (2008).
5. Zhang, L. L. & Zhao, X. S. Carbon-based materials as supercapacitor electrodes. *Chem. Soc. Rev.* **38**, 2520–2531 (2009).
6. Jost, K., Dion, G. & Gogotsi, Y. Textile energy storage in perspective. *J. Mater. Chem. A* **2**, 10776–10787 (2014).
7. Gamby, J., Taberna, P. L., Simon, P., Fauvarque, J. F. & Chesneau, M. Studies and characterisations of various activated carbons used for carbon/carbon supercapacitors. *J. Power Sources* **101**, 109–116 (2001).
8. Permann, L., Lätt, M., Leis, J. & Arulepp, M. Electrical double layer characteristics of nanoporous carbon derived from titanium carbide. *Electrochim. Acta* **51**, 1274–1291 (2006).
9. Chmiola, J., Yushin, G., Dash, R. & Gogotsi, Y. Effect of pore size and surface area of carbide derived carbons on specific capacitance. *J. Power Sources* **158**, 765–772 (2006).
10. Liu, C., Yu, Z., Neff, D., Zhamu, A. & Jang, B. Z. Graphene-based supercapacitor with an ultrahigh energy density. *Nano Lett.* **10**, 4863–4868 (2010).
11. Tsai, W. Y. *et al.* Outstanding performance of activated graphene based supercapacitors in ionic liquid electrolyte from -50 to 80°C. *Nano Energy* **2**, 403–411 (2013).

12. Chen, J. H. *et al.* Electrochemical characterization of carbon nanotubes as electrode in electrochemical double-layer capacitors. *Carbon N. Y.* **40**, 1193–1197 (2002).

13. Frackowiak, E. *et al.* Enhanced capacitance of carbon nanotubes through chemical activation. *Chem. Phys. Lett.* **361**, 35–41 (2002).

14. Frackowiak, E., Metenier, K., Bertagna, V. & Beguin, F. Supercapacitor electrodes from multiwalled carbon nanotubes. *Appl. Phys. Lett.* **77**, 2421–2423 (2000).

15. Wu, N. L. Nanocrystalline oxide supercapacitors. *Mater. Chem. Phys.* **75**, 6–11 (2002).

16. Brousse, T. *et al.* Crystalline MnO[sub 2] as Possible Alternatives to Amorphous Compounds in Electrochemical Supercapacitors. *J. Electrochem. Soc.* **153**, A2171–A2180 (2006).

17. Fan, L. Z. *et al.* High electroactivity of polyaniline in supercapacitors by using a hierarchically porous carbon monolith as a support. *Adv. Funct. Mater.* **17**, 3083–3087 (2007).

18. Seredych, M., Hulicova-Jurcakova, D., Lu, G. Q. & Bandosz, T. J. Surface functional groups of carbons and the effects of their chemical character, density and accessibility to ions on electrochemical performance. *Carbon N. Y.* **46**, 1475–1488 (2008).

19. Chen, T. & Dai, L. Carbon nanomaterials for high-performance supercapacitors. *Mater. Today* **16**, 272–280 (2013).

20. Reimers, J. N. & Dahn, J. R. Electrochemical and In Situ X-Ray Diffraction Studies of Lithium Intercalation in Li x CoO2 . *J. Electrochem. Soc.* **139**, 2091–2097 (1992).

21. Ohzuku, T., Iwakoshi, Y. & Sawai, K. Formation of Lithium-Graphite Intercalation Compounds in Nonaqueous Electrolytes and Their Application as a Negative Electrode for a Lithium Ion (Shuttlecock) Cell. *J. Electrochem. Soc.* **140**, 2490–2498 (1993).

22. Peabody, C. & Arnold, C. B. The role of mechanically induced

separator creep in lithium-ion battery capacity fade. *J. Power Sources* **196**, 8147–8153 (2011).

23. Wang, G., Zhang, L. & Zhang, J. A review of electrode materials for electrochemical supercapacitors. *Chem. Soc. Rev.* **41**, 797–828 (2012).

24. Naseri, F., Farjah, E. & Ghanbari, T. An Efficient Regenerative Braking System Based on Battery/Supercapacitor for Electric, Hybrid, and Plug-In Hybrid Electric Vehicles With BLDC Motor. *IEEE Trans. Veh. Technol.* **66**, 3724–3738 (2017).

25. Teymourfar, R., Asaei, B., Iman-Eini, H. & Nejati fard, R. Stationary super-capacitor energy storage system to save regenerative braking energy in a metro line. *Energy Convers. Manag.* **56**, 206–214 (2012).

26. Luo, X., Wang, J., Dooner, M. & Clarke, J. Overview of current development in electrical energy storage technologies and the application potential in power system operation. *Appl. Energy* **137**, 511–536 (2015).

27. Kyeremateng, N. A., Brousse, T. & Pech, D. Microsupercapacitors as miniaturized energy-storage components for on-chip electronics. *Nat. Nanotechnol.* **12**, 7 (2016).

28. Ma, T., Yang, H. & Lu, L. Development of hybrid battery–supercapacitor energy storage for remote area renewable energy systems. *Appl. Energy* **153**, 56–62 (2015).

29. Lee, H.-., Bullard, G. L., Mason, G. E. & Kern, K. Improved pulse power sources with high-energy density capacitor. *IEEE Trans. Magn.* **25**, 324–330 (1989).

30. Gao, L., Dougal, R. A. & Liu, S. Power enhancement of an actively controlled battery/ultracapacitor hybrid. *IEEE Trans. Power Electron.* **20**, 236–243 (2005).

31. Holland, C. E., Weidner, J. W., Dougal, R. A. & White, R. E. Experimental characterization of hybrid power systems under pulse current loads. *J. Power Sources* **109**, 32–37 (2002).

32. Raymundo-Piñero, E., Kierzek, K., Machnikowski, J. & Béguin, F. Relationship between the nanoporous texture of activated carbons and their capacitance properties in different

electrolytes. *Carbon N. Y.* **44**, 2498–2507 (2006).

33. Yassine, M. & Fabris, D. Performance of commercially available supercapacitors. *Energies* **10**, 1340 (2017).

34. Obreja, V. V. N., Dinescu, A. & Obreja, A. C. Activated carbon based electrodes in commercial supercapacitors and their performance. *Int. Rev. Electr. Eng.* **5**, (2010).

35. Aruna, Z. & Bor Z., J. Method of producing supercapacitor electrodes and cells having high active mass loading. (2017).

36. Frackowiak, E. & Béguin, F. Carbon materials for the electrochemical storage of energy in capacitors. *Carbon N. Y.* **39**, 937–950 (2001).

37. Rufford, T. E., Hulicova-Jurcakova, D., Zhu, Z. & Lu, G. Q. Empirical analysis of the contributions of mesopores and micropores to the double-layer capacitance of carbons. *J. Phys. Chem. C* **113**, 19335–19343 (2009).

38. Salitra, G., Soffer, A., Eliad, L., Cohen, Y. & Aurbach, D. Carbon Electrodes for Double-Layer Capacitors I. Relations Between Ion and Pore Dimensions. *J. Electrochem. Soc.* **147**, 2486–2493 (2000).

39. Vix-Guterl, C. *et al.* Electrochemical energy storage in ordered porous carbon materials. *Carbon N. Y.* **43**, 1293–1302 (2005).

40. Eliad, L., Salitra, G., Soffer, A. & Aurbach, D. On the mechanism of selective electroadsorption of protons in the pores of carbon molecular sieves. *Langmuir* **21**, 3198–3202 (2005).

41. Arulepp, M. *et al.* The advanced carbide-derived carbon based supercapacitor. *J. Power Sources* **162**, 1460–1466 (2006).

42. Huang, J., Sumpter, B. G. & Meunier, V. A universal model for nanoporous carbon supercapacitors applicable to diverse pore regimes, carbon materials, and electrolytes. *Chem. - A Eur. J.* **14**, 6614–6626 (2008).

43. Huang, J., Sumpter, B. G. & Meunier, V. Theoretical model for nanoporous carbon supercapacitors. *Angew. Chemie - Int. Ed.* **47**, 520–524 (2008).

44. John, C., Celine, L., Pierre-Louis, T., Patrice, S. & Yury, G. Desolvation of Ions in Subnanometer Pores and Its Effect on Capacitance and Double-Layer Theory. *Angew. Chemie Int. Ed.* **47**, 3392–3395 (2008).

45. Zhu, Y. *et al.* Supporting Material: Carbon-based supercapacitors produced by activation of graphene. *Science (80-.).* **332**, 1537–41 (2011).

46. Yang, X., Cheng, C., Wang, Y., Qiu, L. & Li, D. Liquid-Mediated Dense Integration of Graphene Materials for Compact Capacitive Energy Storage. *Science (80-.).* **341**, 534–537 (2013).

47. Miller, J. R. & Simon, P. Materials science: Electrochemical capacitors for energy management. *Science (80-.).* **321**, 651–652 (2008).

48. Martin, W. & O., B. J. Wiederaufladbare Batterien. *Chemie unserer Zeit* **33**, 252–266 (2004).

49. Fetcenko, M. A. *et al.* Recent advances in NiMH battery technology. *J. Power Sources* **165**, 544–551 (2007).

50. Liu, Y., Pan, H., Gao, M. & Wang, Q. Advanced hydrogen storage alloys for Ni/MH rechargeable batteries. *J. Mater. Chem.* **21**, 4743–4755 (2011).

51. Melot, B. C. & Tarascon, J.-M. Design and Preparation of Materials for Advanced Electrochemical Storage. *Acc. Chem. Res.* **46**, 1226–1238 (2013).

52. Hannan, M. A., Hoque, M. M., Mohamed, A. & Ayob, A. Review of energy storage systems for electric vehicle applications: Issues and challenges. *Renew. Sustain. Energy Rev.* **69**, 771–789 (2017).

53. Dunn, B., Kamath, H. & Tarascon, J.-M. Electrical Energy Storage for the Grid: A Battery of Choices. *Science (80-.).* **334**, 928–935 (2011).

54. Dong, L. *et al.* Flexible electrodes and supercapacitors for wearable energy storage: a review by category. *J. Mater. Chem. A* **4**, 4659–4685 (2016).

55. Chee, W. K. *et al.* Flexible Graphene-Based Supercapacitors:

A Review. *J. Phys. Chem. C* **120**, 4153–4172 (2016).

56. Dong, L. *et al.* High-performance compressible supercapacitors based on functionally synergic multiscale carbon composite textiles. *J. Mater. Chem. A* **3**, 4729–4737 (2015).

57. Huang, Y. *et al.* From Industrially Weavable and Knittable Highly Conductive Yarns to Large Wearable Energy Storage Textiles. *ACS Nano* **9**, 4766–4775 (2015).

58. Shao, Y. *et al.* Graphene-based materials for flexible supercapacitors. *Chem. Soc. Rev.* **44**, 3639–3665 (2015).

59. Xue, Q. *et al.* Recent Progress on Flexible and Wearable Supercapacitors. *Small* **13**, 1701827 (2017).

60. Ke, Q. & Wang, J. Graphene-based materials for supercapacitor electrodes – A review. *J. Mater.* **2**, 37–54 (2016).

61. Brownson, D. A. C., Kampouris, D. K. & Banks, C. E. An overview of graphene in energy production and storage applications. *J. Power Sources* **196**, 4873–4885 (2011).

62. Bonaccorso, F. *et al.* Graphene, related two-dimensional crystals, and hybrid systems for energy conversion and storage. *Science (80-.).* **347**, 1246501 (2015).

63. Geim, A. K. & Novoselov, K. S. The rise of graphene. *Nat. Mater.* **6**, 183–191 (2007).

64. Iannaccone, G., Bonaccorso, F., Colombo, L. & Fiori, G. Quantum engineering of transistors based on 2D materials heterostructures. *Nat. Nanotechnol.* **13**, 183 (2018).

65. Martin, P. Electrochemistry of gaphene: New horizons for sensing and energy storage. *Chem. Rec.* **9**, 211–223 (2009).

66. Lee, C., Wei, X., Kysar, J. W. & Hone, J. Measurement of the elastic properties and intrinsic strength of monolayer graphene. *Science (80-.).* **321**, 385–388 (2008).

67. Pereira, V. M., Castro Neto, A. H. & Peres, N. M. R. Tight-binding approach to uniaxial strain in graphene. *Phys. Rev. B - Condens. Matter Mater. Phys.* **80**, 045401 (2009).

68. Li, J. & Östling, M. Prevention of Graphene Restacking for Performance Boost of Supercapacitors—A Review. *Crystals* **3**, 163–190 (2013).

69. Lee, J. H. *et al.* Restacking-Inhibited 3D Reduced Graphene Oxide for High Performance Supercapacitor Electrodes. *ACS Nano* **7**, 9366–9374 (2013).

70. Wang, Y. *et al.* Preventing graphene sheets from restacking for high-capacitance performance. *J. Phys. Chem. C* **115**, 23192–23197 (2011).

71. Yoo, J. J. *et al.* Ultrathin Planar Graphene Supercapacitors. *Nano Lett.* **11**, 1423–1427 (2011).

72. Wu, Z. S., Parvez, K., Feng, X. & Müllen, K. Graphene-based in-plane micro-supercapacitors with high power and energy densities. *Nat. Commun.* **4**, 2487 (2013).

73. Ansaldo, A. *et al.* High-power graphene–Carbon nanotube hybrid supercapacitors. *ChemNanoMat* **3**, 436–446 (2017).

74. Paton, K. R. *et al.* Scalable production of large quantities of defect-free few-layer graphene by shear exfoliation in liquids. *Nat. Mater.* **13**, 624 (2014).

75. Karagiannidis, P. G. *et al.* Microfluidization of Graphite and Formulation of Graphene-Based Conductive Inks. *ACS Nano* **11**, 2742–2755 (2017).

76. Del Rio Castillo, A. E. High-yield production of 2D crystals by wet-jet milling. *Mater. Today* **5**, 890–904 (2018).

77. Novoselov, K. S. *et al.* A roadmap for graphene. *Nature* **490**, 192 (2012).

78. Segal, M. Selling graphene by the ton. *Nat. Nanotechnol.* **4**, 612 (2009).

79. Bonaccorso, F. *et al.* Production and processing of graphene and 2d crystals. *Mater. Today* **15**, 564–589 (2012).

80. Ciesielski, A. & Samorì, P. Graphene via sonication assisted liquid-phase exfoliation. *Chem. Soc. Rev.* **43**, 381–398 (2014).

81. Mason, T. J. & Lorimer, J. P. *Applied Sonochemistry: The Uses*

Of Power Ultrasound in Chemistry and Processing. *The Uses of Power Ultrasound in Chesmistry and Processing* (Wiley-VCH, 2002). doi:10.1002/352760054X

82. Khan, U. *et al.* Solvent-Exfoliated Graphene at Extremely High Concentration. *Langmuir* **27**, 9077–9082 (2011).

83. Varrla, E. *et al.* Turbulence-assisted shear exfoliation of graphene using household detergent and a kitchen blender. *Nanoscale* **6**, 11810–11819 (2014).

84. Khan, U., O'Neill, A., Lotya, M., De, S. & Coleman, J. N. High-Concentration Solvent Exfoliation of Graphene. *Small* **6**, 864–871 (2010).

85. Lotya, M., King, P. J., Khan, U., De, S. & Coleman, J. N. High-Concentration, Surfactant-Stabilized Graphene Dispersions. *ACS Nano* **4**, 3155–3162 (2010).

86. Del Rio Castillo, A. E., Ansaldo, A., Pellegrini, V. & Bonaccorso, F. Exfoliation materials by wet-jet milling techniques.

87. Bellani, S. *et al.* WS2–Graphite Dual-Ion Batteries. *Nano Lett.* **18**, 7155–7164 (2018).

88. Hernandez, Y. *et al.* High-yield production of graphene by liquid-phase exfoliation of graphite. *Nat. Nanotechnol.* **3**, 563–568 (2008).

89. Capasso, A. *et al.* Ink-jet printing of graphene for flexible electronics: An environmentally-friendly approach. *Solid State Commun.* **224**, 53–63 (2015).

90. N., C. J. Liquid-Phase Exfoliation of Nanotubes and Graphene. *Adv. Funct. Mater.* **19**, 3680–3695 (2009).

91. Hansen, C. M. Summary for Policymakers. in *Climate Change 2013 - The Physical Science Basis* (2013). doi:10.1017/CBO9781107415324.004

92. Del Rio Castillo, A. E. *et al.* High-yield production of 2D crystals by wet-jet milling. *Mater. Horizons* **5**, 890 (2018).

93. Bonaccorso, F., Bartolotta, A., Coleman, J. N. & Backes, C. 2D-Crystal-Based Functional Inks. *Adv. Mater.* **28**, 6136–6166

(2016).

94. Zhao, W. *et al.* Preparation of graphene by exfoliation of graphite using wet ball milling. *J. Mater. Chem.* **20**, 5817–5819 (2010).

95. Nicolosi, V., Chhowalla, M., Kanatzidis, M. G., Strano, M. S. & Coleman, J. N. Liquid Exfoliation of Layered Materials. *Science (80-.).* **340**, 1226419 (2013).

96. Kouroupis-Agalou, K. *et al.* Fragmentation and exfoliation of 2-dimensional materials: a statistical approach. *Nanoscale* **6**, 5926–5933 (2014).

97. Thomsen, C. & Reich, S. Double resonant raman scattering in graphite. *Phys. Rev. Lett.* **85**, 5214–5217 (2000).

98. Yang, L., Deslippe, J., Park, C. H., Cohen, M. L. & Louie, S. G. Excitonic Effects on the Optical Response of Graphene and Bilayer Graphene. *Phys. Rev. Lett.* **103**, 186802 (2009).

99. Ferrari, A. C. & Basko, D. M. Raman spectroscopy as a versatile tool for studying the properties of graphene. *Nat. Nanotechnol.* **8**, 235–246 (2013).

100. Su, C. Y. *et al.* Electrical and spectroscopic characterizations of ultra-large reduced graphene oxide monolayers. *Chem. Mater.* **21**, 5674–5680 (2009).

101. Ferrari, A. C. *et al.* Raman spectrum of graphene and graphene layers. *Phys. Rev. Lett.* **97**, 187401 (2006).

102. Dresselhaus, M. S., Dresselhaus, G. & Hofmann, M. Raman spectroscopy as a probe of graphene and carbon nanotubes. *Philos. Trans. A. Math. Phys. Eng. Sci.* **366**, 231–236 (2008).

103. Lucchese, M. M. *et al.* Quantifying ion-induced defects and Raman relaxation length in graphene. *Carbon N. Y.* **48**, 1592–1597 (2010).

104. Das, A., Chakraborty, B. & Sood, A. K. Raman spectroscopy of graphene on different substrates and influence of defects. *Bull. Mater. Sci.* **31**, 579–584 (2008).

105. Eckmann, A. *et al.* Probing the nature of defects in graphene by Raman spectroscopy. *Nano Lett.* **12**, 3925–3930 (2012).

106. Ferrari, A. C. Raman spectroscopy of graphene and graphite: Disorder, electron-phonon coupling, doping and nonadiabatic effects. *Solid State Commun.* **143**, 47–57 (2007).

107. Lotya, M. *et al.* Liquid Phase Production of Graphene by Exfoliation of Graphite in Surfactant/Water Solutions. *J. Am. Chem. Soc.* **131**, 3611–3620 (2009).

108. Cançado, L. G. *et al.* Quantifying Defects in Graphene via Raman Spectroscopy at Different Excitation Energies. *Nano Lett.* **11**, 3190–3196 (2011).

109. Bracamonte, M. V, Lacconi, G. I., Urreta, S. E. & Foa Torres, L. E. F. On the Nature of Defects in Liquid-Phase Exfoliated Graphene. *J. Phys. Chem. C* **118**, 15455–15459 (2014).

110. Coleman, J. N. Liquid Exfoliation of Defect-Free Graphene. *Acc. Chem. Res.* **46**, 14–22 (2013).

111. Berman, D., Erdemir, A., Zinovev, A. V & Sumant, A. V. Nanoscale friction properties of graphene and graphene oxide. *Diam. Relat. Mater.* **54**, 91–96 (2015).

112. Chen, J., Ratera, I., Park, J. Y. & Salmeron, M. Velocity Dependence of Friction and Hydrogen Bonding Effects. *Phys. Rev. Lett.* **96**, 236102 (2006).

113. Peng, Y., Wang, Z. & Zou, K. Friction and Wear Properties of Different Types of Graphene Nanosheets as Effective Solid Lubricants. *Langmuir* **31**, 7782–7791 (2015).

114. Zhong, C. *et al.* A review of electrolyte materials and compositions for electrochemical supercapacitors. *Chem. Soc. Rev.* **44**, 7484–7539 (2015).

115. Simon, P., Thierry, B. & Frédéric, F. *Supercapacitors Based on Carbon or Pseudocapacitive Materials*. (2017). doi:10.1002/9781119007333.ch2

116. Devarajan, T. *et al.* Novel ionic liquid electrolyte for electrochemical double layer capacitors. *Electrochem. commun.* **11**, 680–683 (2009).

117. Jung, N. *et al.* Synthesis of chemically bonded graphene/carbon nanotube composites and their application in large volumetric capacitance supercapacitors. *Adv. Mater.* **25**,

6854–6858 (2013).

118. Wang, Y., Song, Y. & Xia, Y. Electrochemical capacitors: Mechanism, materials, systems, characterization and applications. *Chem. Soc. Rev.* **45**, 5925–5950 (2016).

119. De Volder, M. F. L., Tawfick, S. H., Baughman, R. H. & Hart, a J. Carbon nanotubes: present and future commercial applications. *Science* **339**, 535–539 (2013).

120. Peigney, A., Laurent, C., Flahaut, E., Bacsa, R. R. & Rousset, A. Specific surface area of carbon nanotubes and bundles of carbon nanotubes. *Carbon N. Y.* **39**, 507–514 (2001).

121. Izadi-Najafabadi, A. *et al.* Extracting the Full Potential of Single-Walled Carbon Nanotubes as Durable Supercapacitor Electrodes Operable at 4 V with High Power and Energy Density. *Adv. Mater.* **22**, E235–E241 (2010).

122. An, K. H. *et al.* Supercapacitors Using Single-Walled Carbon Nanotube Electrodes. *Adv. Mater.* **13**, 497–500 (2001).

123. Kharissova, O. V., Kharisov, B. I. & De Casas Ortiz, E. G. Dispersion of carbon nanotubes in water and non-aqueous solvents. *RSC Adv.* **3**, 24812–24852 (2013).

124. Bondavalli, P., Delfaure, C., Legagneux, P. & Pribat, D. Supercapacitor Electrode Based on Mixtures of Graphite and Carbon Nanotubes Deposited Using a Dynamic Air-Brush Deposition Technique. *J. Electrochem. Soc.* **160**, A601–A606 (2013).

125. Bhushan, B. *Introduction to Tribology, Second Edition*. (John Wiley & Sons, 2013). doi:10.1002/9781118403259

126. Akinwande, D. *et al.* A review on mechanics and mechanical properties of 2D materials—Graphene and beyond. *Extrem. Mech. Lett.* **13**, 42–77 (2017).

127. Filleter, T. *et al.* Friction and Dissipation in Epitaxial Graphene Films. *Phys. Rev. Lett.* **102**, 86102 (2009).

128. Lee, C. *et al.* Elastic and frictional properties of graphene. *Phys. status solidi* **246**, 2562–2567 (2009).

129. Lee, C. *et al.* Frictional Characteristics of Atomically Thin

Sheets. *Science (80-.).* **328**, 76–80 (2010).

130. Berman, D., Erdemir, A. & Sumant, A. V. Few layer graphene to reduce wear and friction on sliding steel surfaces. *Carbon N. Y.* **54**, 454–459 (2013).

131. Lee, H. L. and N. L. and Y. S. and J. E. and S. Comparison of frictional forces on graphene and graphite. *Nanotechnology* **20**, 325701 (2009).

132. Berman, D., Erdemir, A. & Sumant, A. V. Graphene: a new emerging lubricant. *Mater. Today* **17**, 31–42 (2014).

133. Lin, L. Y., Kim, D. E., Kim, W. K. & Jun, S. C. Friction and wear characteristics of multi-layer graphene films investigated by atomic force microscopy. *Surf. Coatings Technol.* **205**, 4864–4869 (2011).

134. Robinson, B. J., Kay, N. D. & Kolosov, O. V. Nanoscale interfacial interactions of graphene with polar and nonpolar liquids. *Langmuir* **29**, 7735–7742 (2013).

135. Akbari, A. *et al.* Solvent Transport Behavior of Shear Aligned Graphene Oxide Membranes and Implications in Organic Solvent Nanofiltration. *ACS Appl. Mater. Interfaces* **10**, 2067–2074 (2018).

136. http://www.mtixtl.com/HighSurfaceActiveCarbonForSuper-CapacitorElectrode200g/Bag-E.aspx.

137. Carpick, R. W. & Salmeron, M. Scratching the Surface: Fundamental Investigations of Tribology with Atomic Force Microscopy. *Chem. Rev.* **97**, 1163–1194 (1997).

138. Buzio, R. *et al.* Ultralow friction of ink-jet printed graphene flakes. *Nanoscale* **9**, 7612–7624 (2017).

139. Tocha, E., Schönherr, H. & Vancso, G. J. Quantitative Nanotribology by AFM: A Novel Universal Calibration Platform. *Langmuir* **22**, 2340–2350 (2006).

140. Schwarz, U. D., Köster, P. & Wiesendanger, R. Quantitative analysis of lateral force microscopy experiments. *Rev. Sci. Instrum.* **67**, 2560–2567 (1996).

141. Lantz, M. A., O'Shea, S. J., Hoole, A. C. F. & Welland, M. E.

Lateral stiffness of the tip and tip-sample contact in frictional force microscopy. *Appl. Phys. Lett.* **70**, 970–972 (1997).

142. Carpick, R. W., Ogletree, D. F. & Salmeron, M. Lateral stiffness: A new nanomechanical measurement for the determination of shear strengths with friction force microscopy. *Appl. Phys. Lett.* **70**, 1548–1550 (1997).

143. Choi, W. S., Heo, J., Chung, I. & Hong, B. The effect of RF power on tribological properties of the diamond-like carbon films. *Thin Solid Films* **475**, 287–290 (2005).

144. Lin, L.-Y., Kim, D.-E., Kim, W.-K. & Jun, S.-C. Friction and wear characteristics of multi-layer graphene films investigated by atomic force microscopy. *Surf. Coatings Technol.* **205**, 4864–4869 (2011).

145. Ricci, M., Trewby, W., Cafolla, C. & Voïtchovsky, K. Direct observation of the dynamics of single metal ions at the interface with solids in aqueous solutions. *Sci. Rep.* **7**, 43234 (2017).

146. Oliver, J. B. P. and W. C. Tip Surface Interactions in STM and AFM. *Phys. Scr.* **1987**, 61 (1987).

147. Stoller, M. D. & Ruoff, R. S. Best practice methods for determining an electrode material’s performance for ultracapacitors. *Energy Environ. Sci.* **3**, 1294–1301 (2010).

148. Gogotsi, Y. & Simon, P. True performance metrics in electrochemical energy storage. *Science (80-.).* **334**, 917–918 (2011).

149. Sanliang, Z. & Ning, P. Supercapacitors Performance Evaluation. *Adv. Energy Mater.* **5**, 1401401 (2014).

150. Bowden, F. P., Tabor, D. & Palmer, F. *The Friction and Lubrication of Solids*. (Oxford University Press, 1951). doi:10.1119/1.1933017

151. Popov, V. L. *Contact mechanics and friction*. (Springer-Verlag, 2013). doi:10.1016/b978-0-08-052402-3.50015-0

152. Popov, V. L., Starcevic, J. & Filippov, A. E. Influence of Ultrasonic In-Plane Oscillations on Static and Sliding Friction and Intrinsic Length Scale of Dry Friction Processes. *Tribol.*

Lett. **39**, 25–30 (2010).

153. Ben-David, O. & Fineberg, J. Static Friction Coefficient Is Not a Material Constant. *Phys. Rev. Lett.* **106**, 254301 (2011).

154. Scholz, C. H. Earthquakes and friction laws. *Nature* **391**, 37 (1998).

155. Berthoud, P., Baumberger, T., G'Sell, C. & Hiver, J.-M. Physical analysis of the state- and rate-dependent friction law: Static friction. *Phys. Rev. B* **59**, 14313–14327 (1999).

156. Ben-David, O., Rubinstein, S. M. & Fineberg, J. Slip-stick and the evolution of frictional strength. *Nature* **463**, 76 (2010).

157. Raviv, U., Laurat, P. & Klein, J. Fluidity of water confined to subnanometre films. *Nature* **413**, 51 (2001).

158. Marchetto, D. *et al.* Friction and Wear on Single-Layer Epitaxial Graphene in Multi-Asperity Contacts. *Tribol. Lett.* **48**, 77–82 (2012).

159. Jinjin, L., Tianyang, G. & Jianbin, L. Superlubricity of Graphite Induced by Multiple Transferred Graphene Nanoflakes. *Adv. Sci.* **5**, 1700616 (2018).

160. Deng, Z., Smolyanitsky, A., Li, Q., Feng, X.-Q. & Cannara, R. J. Adhesion-dependent negative friction coefficient on chemically modified graphite at the nanoscale. *Nat. Mater.* **11**, 1032 (2012).

161. Ruan, J. & Bhushan, B. Frictional behavior of highly oriented pyrolytic graphite. *J. Appl. Phys.* **76**, 8117–8120 (1994).

162. https://www.idtechex.com/research/reports/supercapacitor-technologies-and-markets-2018-2028-000568.asp.

163. Brunauer, S., Emmett, P. H. & Teller, E. Adsorption of Gases in Multimolecular Layers. *J. Am. Chem. Soc.* **60**, 309–319 (1938).

164. Walton, K. S. & Snurr, R. Q. Applicability of the BET Method for Determining Surface Areas of Microporous Metal−Organic Frameworks. *J. Am. Chem. Soc.* **129**, 8552–8556 (2007).

165. Fagerlund, G. Determination of specific surface by the BET method. *Matériaux Constr.* **6**, 239–245 (1973).

166. Wang, S., Minami, D. & Kaneko, K. Comparative pore structure analysis of highly porous graphene monoliths treated at different temperatures with adsorption of N<inf>2</inf> at 77.4 K and of Ar at 87.3 K and 77.4 K. *Microporous Mesoporous Mater.* **209**, 72–78 (2015).

167. Physisorption of gases, with special reference to the evaluation of surface area and pore size distribution (IUPAC Technical Report) . *Pure and Applied Chemistry* **87**, 1051 (2015).

168. Greenhow, C. & Smith, W. V. Molecular Quadrupole Moments of N2 and O2. *J. Chem. Phys.* **19**, 1298–1300 (1951).

169. Drain, L. E. Permanent electric quadrupole moments of molecules and heats of adsorption. *Trans. Faraday Soc.* **49**, 650–654 (1953).

170. Ismail, I. M. K. Cross-sectional areas of adsorbed nitrogen, argon, krypton, and oxygen on carbons and fumed silicas at liquid nitrogen temperature. *Langmuir* **8**, 360–365 (1992).

171. Sing, K. S. W. Physisorption of gases by carbon blacks. *Carbon N. Y.* **32**, 1311–1317 (1994).

172. Ravikovitch, P. I., Vishnyakov, A., Russo, R. & Neimark, A. V. Unified Approach to Pore Size Characterization of Microporous Carbonaceous Materials from N2, Ar, and CO2 Adsorption Isotherms. *Langmuir* **16**, 2311–2320 (2000).

173. Ravikovitch, P. I. & Neimark, A. V. Density Functional Theory Model of Adsorption on Amorphous and Microporous Silica Materials. *Langmuir* **22**, 11171–11179 (2006).

174. Lei, Z., Christov, N. & Zhao, X. S. Intercalation of mesoporous carbon spheres between reduced graphene oxide sheets for preparing high-rate supercapacitor electrodes. *Energy Environ. Sci.* **4**, 1866–1873 (2011).

175. Guo, C. X. & Li, C. M. A self-assembled hierarchical nanostructure comprising carbon spheres and graphene nanosheets for enhanced supercapacitor performance. *Energy Environ. Sci.* **4**, 4504–4507 (2011).

176. Zheng, C., Zhou, X., Cao, H., Wang, G. & Liu, Z. Synthesis of porous graphene/activated carbon composite with high packing density and large specific surface area for supercapacitor

electrode material. *J. Power Sources* **258**, 290–296 (2014).

177. Phillips, C., Al-Ahmadi, A., Potts, S.-J., Claypole, T. & Deganello, D. The effect of graphite and carbon black ratios on conductive ink performance. *J. Mater. Sci.* **52**, 9520–9530 (2017).

178. https://www.tedpella.com/semmisc_html/sempaint.htm#anchor16050.

179. https://dyenamo.se/dyenamo_electrode_pastes.php.

180. Pandolfo, A. G. & Hollenkamp, A. F. Carbon properties and their role in supercapacitors. *J. Power Sources* **157**, 11–27 (2006).

181. Kierzek, K., Frackowiak, E., Lota, G., Gryglewicz, G. & Machnikowski, J. Electrochemical capacitors based on highly porous carbons prepared by KOH activation. *Electrochim. Acta* **49**, 515–523 (2004).

182. Gryglewicz, G., Machnikowski, J., Lorenc-Grabowska, E., Lota, G. & Frackowiak, E. Effect of pore size distribution of coal-based activated carbons on double layer capacitance. *Electrochim. Acta* **50**, 1197–1206 (2005).

183. Yang, Z. *et al.* Recent Advancement of Nanostructured Carbon for Energy Applications. *Chem. Rev.* **115**, 5159–5223 (2015).

184. Kondrat, S., Pérez, C. R., Presser, V., Gogotsi, Y. & Kornyshev, A. A. Effect of pore size and its dispersity on the energy storage in nanoporous supercapacitors. *Energy Environ. Sci.* **5**, 6474–6479 (2012).

185. Devillers, N., Jemei, S., Péra, M.-C., Bienaimé, D. & Gustin, F. Review of characterization methods for supercapacitor modelling. *J. Power Sources* **246**, 596–608 (2014).

186. Kötz, R. & Carlen, M. Principles and applications of electrochemical capacitors. *Electrochim. Acta* **45**, 2483–2498 (2000).

187. Xu, B. *et al.* What is the choice for supercapacitors: graphene or graphene oxide? *Energy Environ. Sci.* **4**, 2826–2830 (2011).

188. Lee, Y.-H., Chang, K.-H. & Hu, C.-C. Differentiate the pseudocapacitance and double-layer capacitance contributions for nitrogen-doped reduced graphene oxide in acidic and alkaline electrolytes. *J. Power Sources* **227**, 300–308 (2013).

189. Lin, Z. *et al.* Superior Capacitance of Functionalized Graphene. *J. Phys. Chem. C* **115**, 7120–7125 (2011).

190. Raccichini, R., Varzi, A., Passerini, S. & Scrosati, B. The role of graphene for electrochemical energy storage. *Nat. Mater.* **14**, 271 (2014).

191. Yan, F. *et al.* Renewing Functionalized Graphene as Electrodes for High-Performance Supercapacitors. *Adv. Mater.* **24**, 6348–6355 (2012).

192. Pohlmann, S., Ramirez-Castro, C. & Balducci, A. The Influence of Conductive Salt Ion Selection on EDLC Electrolyte Characteristics and Carbon-Electrolyte Interaction. *J. Electrochem. Soc.* **162**, A5020–A5030 (2015).

193. Fletcher, S., Black, V. J. & Kirkpatrick, I. A universal equivalent circuit for carbon-based supercapacitors. *J. Solid State Electrochem.* **18**, 1377–1387 (2014).

194. Fletcher, S. *et al.* The modelling of carbon-based supercapacitors: Distributions of time constants and Pascal Equivalent Circuits. *J. Power Sources* **345**, 247–253 (2017).

195. Liu, X. *et al.* Experimental and theoretical studies of nonlinear dependence of the internal resistance and electrode thickness for high performance supercapacitor. *Sci. Rep.* **7**, 45934 (2017).

196. Yoon, S., Jang, J. H., Ka, B. H. & Oh, S. M. Complex capacitance analysis on rate capability of electric-double layer capacitor (EDLC) electrodes of different thickness. *Electrochim. Acta* **50**, 2255–2262 (2005).

197. Jost, K. *et al.* Knitted and screen printed carbon-fiber supercapacitors for applications in wearable electronics. *Energy Environ. Sci.* **6**, 2698–2705 (2013).

198. Yang, Y. *et al.* Waterproof, Ultrahigh Areal-Capacitance, Wearable Supercapacitor Fabrics. *Adv. Mater.* **29**, 1606679 (2017).

199. Beidaghi, M. & Gogotsi, Y. Capacitive energy storage in micro-scale devices: recent advances in design and fabrication of micro-supercapacitors. *Energy Environ. Sci.* **7**, 867–884 (2014).

200. Shen, C. *et al.* A Review of On-Chip Micro Supercapacitors for Integrated Self-Powering Systems. *J. Microelectromechanical Syst.* **26**, 949–965 (2017).

201. Wu, Z. S., Feng, X. & Cheng, H. M. Recent advances in graphene-based planar micro-supercapacitors for on-chip energy storage. *Natl. Sci. Rev.* **1**, 277–292 (2014).

202. Yang, D. *et al.* Chemical analysis of graphene oxide films after heat and chemical treatments by X-ray photoelectron and Micro-Raman spectroscopy. *Carbon N. Y.* **47**, 145–152 (2009).

203. Talaie, E. *et al.* Methods and protocols for electrochemical energy storage materials research. *Chem. Mater.* **29**, 90–105 (2017).

204. Conway, B. E. *Electrochemical Capacitors: Scientific Fundamentals and Technological Applications*. (Kluwer Academic/Plenum, 1999). doi:10.1007/978-1-4757-3058-6

205. Zhang, Y. *et al.* Progress of electrochemical capacitor electrode materials: A review. *Int. J. Hydrogen Energy* **34**, 4889–4899 (2009).

206. Pumera, M. The electrochemistry of carbon nanotubes: Fundamentals and applications. *Chem. - A Eur. J.* **15**, 4970–4978 (2009).

207. Wang, G. *et al.* Solid-state supercapacitor based on activated carbon cloths exhibits excellent rate capability. *Adv. Mater.* **26**, 2676–2682 (2014).

208. Ramadoss, A., Saravanakumar, B. & Kim, S. J. Thermally reduced graphene oxide-coated fabrics for flexible supercapacitors and self-powered systems. *Nano Energy* **15**, 587–597 (2015).

209. Jung, S., Lee, J., Hyeon, T., Lee, M. & Kim, D. H. Fabric-based integrated energy devices for wearable activity monitors. *Adv. Mater.* **26**, 6329–6334 (2014).

210. Song, Y. *et al.* Ostwald Ripening Improves Rate Capability of High Mass Loading Manganese Oxide for Supercapacitors. *ACS Energy Lett.* **2**, 1752–1759 (2017).

211. Li, X. *et al.* High energy flexible supercapacitors formed via bottom-up infilling of gel electrolytes into thick porous electrodes. *Nat. Commun.* **9**, 2578 (2018).

212. Oakes, L. *et al.* Surface engineered porous silicon for stable, high performance electrochemical supercapacitors. *Sci Rep* **3**, 3020 (2013).

213. Grigoras, K. *et al.* Conformal titanium nitride in a porous silicon matrix: A nanomaterial for in-chip supercapacitors. *Nano Energy* **26**, 340–345 (2016).

214. Lei, Z. *et al.* A high-energy-density supercapacitor with graphene-CMK-5 as the electrode and ionic liquid as the electrolyte. *J. Mater. Chem. A* **1**, 2313–2321 (2013).

215. Xu, Y. *et al.* Holey graphene frameworks for highly efficient capacitive energy storage. *Nat. Commun.* **5**, 4554 (2014).

216. Cheng, Q. *et al.* Graphene and carbon nanotube composite electrodes for supercapacitors with ultra-high energy density. *Phys. Chem. Chem. Phys.* **13**, 17615–17624 (2011).

217. Dubal, D. P., Chodankar, N. R., Kim, D.-H. & Gomez-Romero, P. Towards flexible solid-state supercapacitors for smart and wearable electronics. *Chem. Soc. Rev.* **47**, 2065–2129 (2018).

218. Yang, P. & Mai, W. Flexible solid-state electrochemical supercapacitors. *Nano Energy* **8**, 274–290 (2014).

219. Cheng, X., Pan, J., Zhao, Y., Liao, M. & Peng, H. Gel Polymer Electrolytes for Electrochemical Energy Storage. *Adv. Energy Mater.* **8**, 1702184 (2017).

220. Li, J., Mishukova, V. & Östling, M. All-solid-state micro-supercapacitors based on inkjet printed graphene electrodes. *Appl. Phys. Lett.* **109**, 123901 (2016).

221. Chen, Q. *et al.* Effect of different gel electrolytes on graphene-based solid-state supercapacitors. *RSC Adv.* **4**, 36253–36256 (2014).

222. Bellani, S. *et al.* Scalable Production of Graphene Inks via Wet-Jet Milling Exfoliation for Screen-Printed Micro-Supercapacitors. *Adv. Funct. Mater.* **29**, 1807659 (2019).

223. MWC. Available at: https://www.mwcbarcelona.com.

224. Bellani, S. *et al.* ITO nanoparticles break optical transparency/high-areal capacitance trade-off for advanced aqueous supercapacitors. *J. Mater. Chem. A* **5**, 25177–25186 (2017).

225. Kouroupis-Agalou, K. *et al.* Fragmentation and exfoliation of 2-dimensional materials: A statistical approach. *Nanoscale* **6**, 5926–5933 (2014).

226. Schneider, C. A., Rasband, W. S. & Eliceiri, K. W. NIH Image to ImageJ: 25 years of image analysis. *Nat. Methods* **9**, 671 (2012).

227. Seifert, E. OriginPro 9.1: Scientific Data Analysis and Graphing Software—Software Review. *J. Chem. Inf. Model.* **54**, 1552 (2014).

228. M., S. F. Measurement of Sheet Resistivities with the Four-Point Probe. *Bell Syst. Tech. J.* **37**, 711–718 (2018).

TWO-DIMENSIONAL MATERIALS IN PEROVSKITE SOLAR CELLS

SUMMARY

This chapter deals with one of the most promising photovoltaic technologies: perovskite solar cells. The interest in perovskite materials is due to their tunable physical properties (making them optimal candidates for photovoltaics), their abundance and the ease of processing for the production of perovskite solar cells. However, perovskites suffer from low stability and degrade easily in ambient atmosphere (*i.e.,* in the presence of oxygen and/or moisture). For this reason, dimensional-tailoring of these materials was proposed as a strategy to mitigate the instability issues, but their lower efficiencies than their 3D counterparts, make challenging their commercialization. In this chapter, two projects concerning the use of 2D materials (specifically MoS_2 and WS_2 flakes dispersions) in low dimensional perovskites are discussed. To the best of our knowledge, this is the first time that low dimensional perovskites and 2D materials are used together in photovoltaic devices.

These projects have been conducted in collaboration with Doctor Francesco Bonaccorso (IIT, Genova, Italy), developed during an abroad research program (from January 2019 until July 2019) held in the group of Professor Mohammad Khaja Nazeeruddin (EPFL, Sion, Switzerland) and supervised by Professor Giulia Grancini (University of Pavia, Italy). These works are still in progress at the time of this thesis submission (end of July 2019).

INTRODUCTION

Nowadays we live in a capitalistic/consumerist era, which encourages the mass production of any kind of goods and products (from automotive industries to clothing, from intensive breeding to luxury goods) for private ownership and accumulation. This socio-political trend led industries and companies to focus on relentless mass production, paving the way for a huge increase in our society energy demands: 18.5 TeraWatt year per year (TWy/y) in 2015 (**figure 1**), with an estimation of 27 TWy/y in 2050.[1]

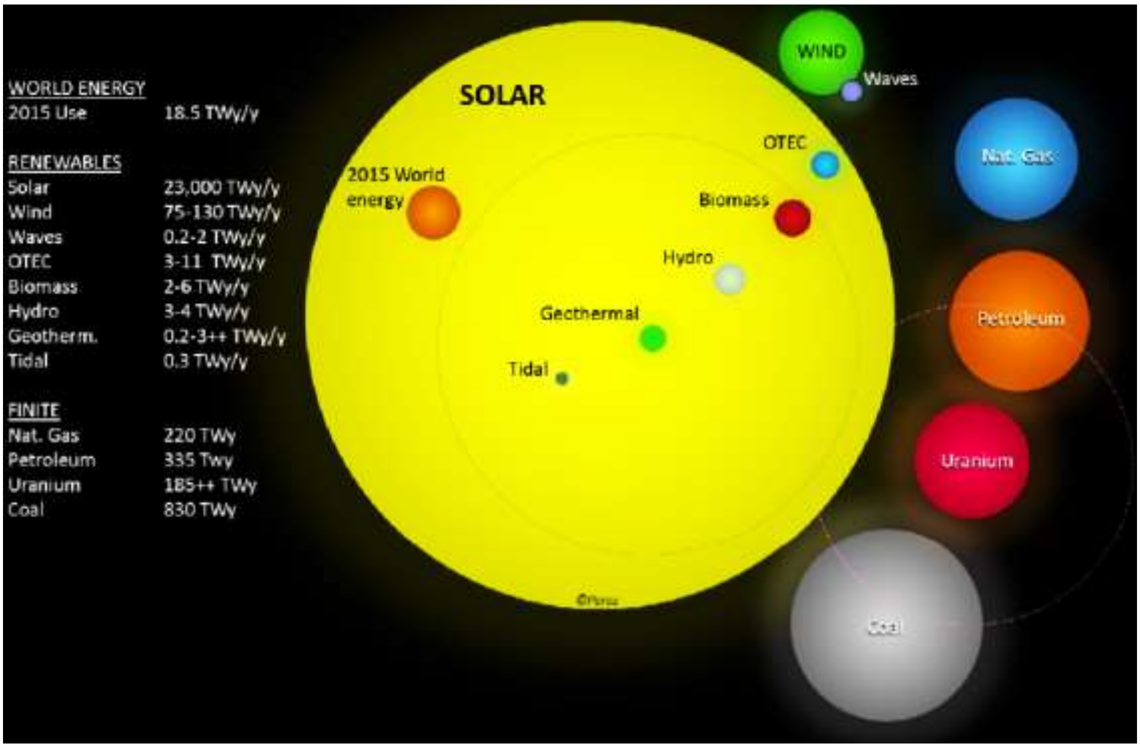

Figure 1: Estimation of global energy demand, finite and renewable energy sources in 2015. Comparison between the world energy demand, the energy that renewable resources can provide every year and the total reserves from finite resources (data referring to 2015). The dotted line, around the uranium circle, indicates the value that would be achieved if 100% of the fission by-products could be reprocessed. The dotted line, around the geothermal circle, refers to the scenario where deep hydro-fracking based technologies would be used (these technologies were considered environmentally detrimental and not demonstrated by 2015). OTEC: ocean thermal energy conversion (figure and data taken from ref.[1]).

Currently, coal, petroleum, natural gas and uranium are the most exploited energy sources. However, not only these energy fuels are pollutant (*i.e.,* their use releases greenhouse gases or nuclear wastes as by-products) but also their reserves are finite, which means they are exhaustible and non-renewable.[1,2] Conversely, there are many alternative energy fuels that are both environmentally friendly and renewable. This is the case of hydropower, biofuels, geothermal, ocean thermal and solar energies (just to name few). Nevertheless, these renewable fuels are not all equivalent, because they can supply a finite amount of energy per year, sometimes too few (such as 2 – 6 TWy/y from biomass) to cover the overall mankind energy demands.[1,2] There are only two renewable energy fuels that can completely fulfil this request: wind (75 – 130 TWy/y) and solar energy (23000 TWy/y), the last one being orders of magnitude higher than the sum of all of the other environmental-friendly fuels.[1,2]

On the basis of the above consideration, the exploitation of solar power through solar cells (SCs or photovoltaic devices) technology is the most pursued viable path to meet the global energy demand. In SCs, solar energy is converted into electricity by means of the photovoltaic effect in semiconductors (*i.e.,* the formation of electron-hole pairs upon the absorption of a photon with energy higher than the semiconductors band gaps). In the last 60 years, different photovoltaic technologies have been proposed and studied, with the aim to increase both the SCs performances and to decrease the production costs.[3] In particular, in less than 10 years, photovoltaics experienced a 75% cost reduction, that led to a huge increment of global photovoltaic installations (from 178 GW in 2014 to 540 GW in 2019).[4,5] In this context, perovskite semiconductor materials are now playing a major role in photovoltaics thanks to their abundance, stunning properties for SCs applications, low cost and higher availability to the global population.[4]

This chapter is devoted to perovskite solar cells (PSCs). After introducing these photovoltaic devices from an historical perspective, the physico-chemical properties of perovskite materials will be discussed and, finally, preliminary results concerning two different projects on PSCs will be presented.

SOLAR CELLS TECHNOLOGIES

The first SC, presented in 1954, was developed by David Chapin, Calvin Fuller and Gerald Pearson (at the Bell Labs) by using a Si p-n junction and achieving a power conversion efficiency (PCE) of 6%.[6] This success paved the way for further research in the 1960s on solar cells fabricated with Si (mono- or poly-crystalline) that are nowadays referred to *first generation photovoltaics*.[7] Currently, these are the most used devices for many reasons: Si is an earth-abundant, non-toxic element, the use of Si in SCs is compatible with already existing Si-based technologies[7] and Si-based SCs deliver high efficiencies ($PCE_{mono\text{-}Si}$: 26.7%).[8]

However, the mono-Si SCs presents other disadvantages, *i.e.,* the need for thick Si absorbers (~300 µm, because Si absorption coefficient is low, due to its indirect band-gap);[3,7,8] the release of some hazardous by-products (like CO) during the purification process of SiO_2 into Si[3] and the high cost of high-temperatures and chemical treatments needed for the production of mono-Si.[3] For these reasons, alternative materials and technologies have been proposed, based on the use of thin-film materials, nowadays referred to *second-generation photovoltaics*.[3,7,8] This group includes SCs made up by amorphous-Si, micro-crystalline-Si, Copper Indium Gallium Selenide

(CIGS), Cadmium Telluride (CdTe) and Gallium Arsenide (GaAs).[3,7,8] The fabrication costs of some of this kind of SCs is cheaper than mono-Si technologies and requires a smaller amount of materials, because the absorption coefficient of the absorbing layers is high (which is the reason why these devices are also referred to thin-film photovoltaics).[3,7] Unlike Si technologies, thin-film SCs are not self-supporting, leading to the use of a substrate for the deposition of the films: glass, stainless steel and polymer foils being the main ones (in the last case, flexible SCs can be realized).[3] However, second-generation photovoltaics use, in some cases, rare elements (such as selenium, indium and tellurium)[3] and the efficiencies are lower than mono-Si (the maximum value being PCE_{CIGS}: 22.9%),[8] the only exception is GaAs that provides the highest PCE for thin-film, single-junction SCs (PCE_{GaAs}: 29.1%, **figure 2**).[3,8]

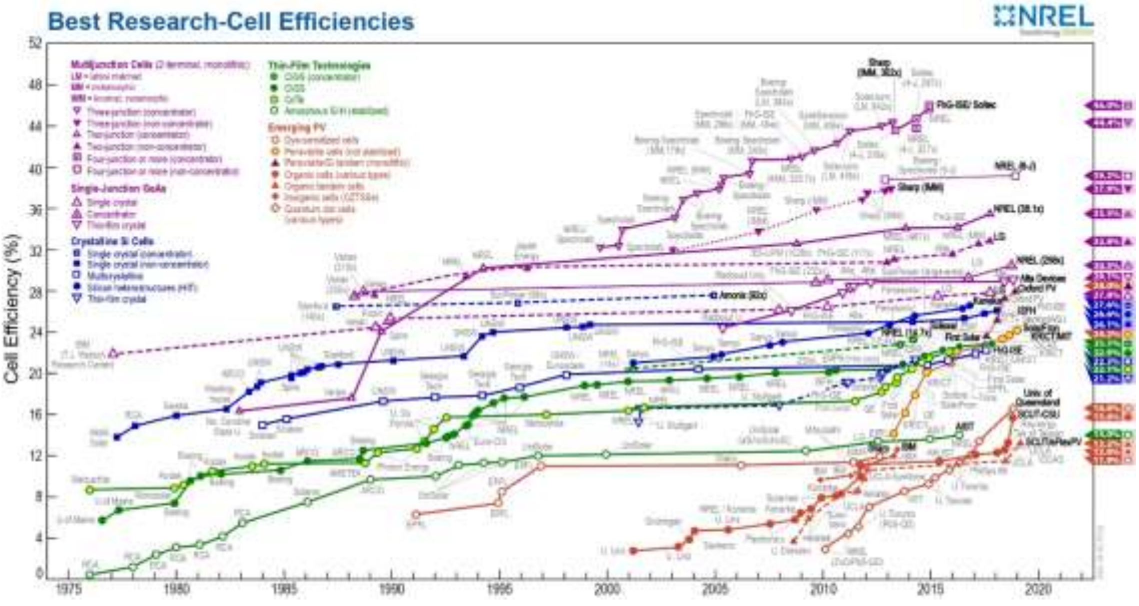

Figure 2: Best research-cell efficiency chart. The National Renewable Energy Laboratory (NREL) keeps track of the highest efficiencies of photovoltaic devices, since 1976 (taken from ref.[9]).

Another advantage of GaAs is its tolerance to radiation, making this material the benchmark for space applications,[7,8] but the expensive cost of Ga (abundance of 14 ppm in Earth's crust)[10] and the suggested carcinogenic nature of GaAs[11] hinder its use on a large scale. While research on the first- and second-generations SCs is still ongoing, a *third-generation photovoltaics* raised, aiming for high efficiency/low-cost SCs by introducing both new designs and materials.[3,7] In fact, in single-junction SCs, the maximum efficiency is limited to 33% (according to the Shockley-Queisser limit, that considers SCs with band-gaps ranging from 1.0 to 1.8 eV, at a temperature of 300 K, under AM1.5 illumination – a reference solar spectral distribution, defined in the International Standard IEC 60904-3).[3,12] To overcome this limit, in third-generation photovoltaics new designs were proposed, like multi-junctions (MJ) solar cells (where semiconductors, with different band-gaps, are stacked together to increase the amount of absorbed photons) and concentrator photovoltaics (in which lenses and mirrors are used to focus the solar radiation on SCs).[3,7] Currently, concentrated multi-junctions SCs provide the highest efficiency reported to date (PCE: 46%) while for non-concentrated multi-junctions SCs the highest efficiency is 39.2% (**figure 2**). However, these technologies are affected by the added cost of lenses, mirrors and the non-trivial technology for the extraction of current from multi-junctions solar cells. Third-generation photovoltaics introduced even new materials for solar harnessing technologies, leading to the realization of dye-sensitized solar cells (DSSCs) and PSCs.[7] A DSSC is made up by a mechanical support (*e.g.*, glass) coated with a transparent conductive oxide (acting as electrode) which is covered by a mesoporous semiconducting film (*i.e.,* TiO_2, SnO_2 or ZnO).[13,14] A sensitizing dye is adsorbed on the mesoporous layer and acts as light-harvester: when a photon (with equal or bigger energy than the dye band-gap) is absorbed, an electron/hole pair is created.[13,14] The electron transfers to the conduction band (CB) of the mesoporous layer, while the dye is neutralized by a redox couple (usually I^-/I_3^-) by transferring the positive charge to a counter electrode.[13,14] The use of cheap materials and the ease of fabrication of DSSCs have made them extremely interesting in the scientific community since their discovery.[13] However, these devices suffer from several limitations such as the loss-in-potential for both electron injection to TiO_2 and redox reactions, posing an upper limit to the efficiencies of DSSCs.[13] For example, in the case of ruthenium metal complex dye with the I^-/I_3^- redox couple, the maximum PCE is only 13.8%.[13] One way to increase the efficiencies of DSSCs is the use of light-harvesters absorbing in the near-infrared region, such as inorganic quantum dots or thin semiconducting films.[13,15,16] It is in this context that, in 2009, Miyasaka and co-workers published the first peer-reviewed article concerning the use of perovskites as sensitizers in DSSCs.[17]

ARCHITECTURE FOR PEROVSKITE SOLAR CELLS

In the 2009 paper, Myiasaka group described a DSSC made up by a $CH_3NH_3PbI_3$ ($MAPbI_3$) perovskite sensitizer and the I^-/I_3^- redox couple, showing a PCE: 3.5%.[17] Two years later, Park *et al.* achieved PCE of 6.5%, always in a liquid electrolyte, by optimising the TiO_2 and perovskite depositions.[18] However, these polar liquid-electrolyte-based devices cause the fast degradation (within few minutes) of the perovskite.[15,19,20] In attempting to solve this hurdle, in 2012 Park, Gratzel *et al.* developed all-solid-state devices by using $MAPbI_3$ and the organic molecule (2,2(7,7)-tetrakis-(N,N-dipmethoxyphenylamine)9,9(-spirobifluorene)) (spiro-OMeTAD) as hole transporting material (HTM), achieving PCE up to 8%.[21] In the same year, Miyasaka, Snaith *et al.* fabricated all-solid-state PSCs with a mixed halide perovskite ($MAPbI_{3-x}Cl_x$) absorber and spiro-OMeTAD as HTM, reaching a PCE of 10%.[22] These all-solid-state solar cells solved the problem of the perovskite degradation (leading to a device stability up to 500 h)[20] and opened up the field of perovskite applications in photovoltaics.[23,24] The all-solid-state architecture, proposed by these two pioneering works, has remained ever since almost the same. In fact, nowadays PSCs are being prepared by using three main configurations: planar n-i-p (**figure 3a**), mesoporous n-i-p (**figure 3b**) and planar p-i-n (**figure 3c**).

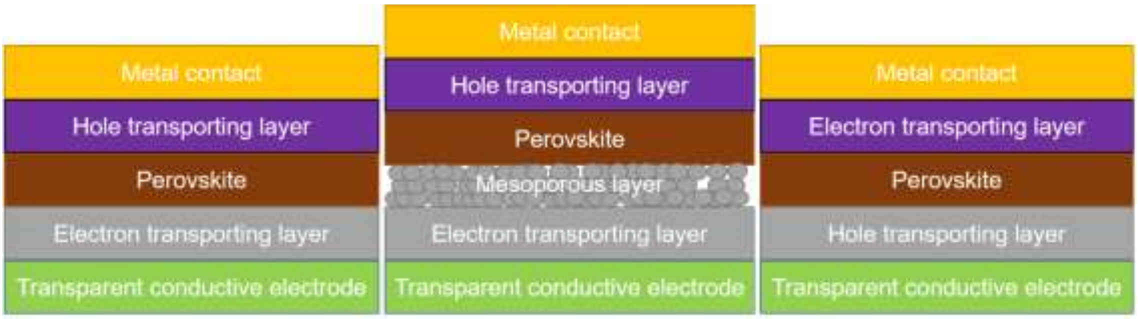

a) Planar n-i-p **b)** Mesoporous n-i-p **c)** Planar p-i-n

Figure 3: Devices architectures. Representative illustration of the most used devices architectures: (a) planar p-i-n, (b) mesoporous n-i-p and (c) planar p-i-n.

In the first architecture, a transparent conductive electrode (like fluorine-doped tin oxide – FTO – or indium tin oxide – ITO –) is covered by a compact electron selective layer (*i.e.,* c-TiO_2 or c-SnO_2), the perovskite layer, a hole selective layer (*i.e.,* spiro-OMe-TAD or poly[bis(4-phenil) (2,4,6,-trimethylphenyl) amine] poly (triarylamine) – PTAA –) and a metal contact.[24,25] The difference between the planar and mesoporous n-i-p configurations is due to the presence of a mesoporous layer (usually m-TiO_2) between the compact layer and the perovskite.[24,25] Lastly, in the planar p-i-n structure, the deposition of the charge selective layers is “inverted”, *i.e.,* the ITO is covered by the hole transport material (*e.g.*, PTAA), the perovskite layer, the electron selective layer (*i.e.*, C60 fullerene or [6,6]-phenyl-c61-butyric acid methyl ester – PCBM –) and the metal contact (Cu).[24,25] The optimization of the layers deposition, as well as a careful tuning of the perovskite properties, has allowed a raising of the PCE from 10% in 2012[21] to the current 24.2% record (**figure 2**, data not published yet, but certificated and registered at the NREL chart).[26,27]

PEROVSKITE MATERIALS

The word perovskite was used for the first time to designate calcium titanate oxide ($CaTiO_3$), a mineral found in the Ural Mountains of Russia in 1839 and studied by the mineralogist Lev Perovski (from whom the name perovskite was taken).[19,28] Nowadays, the word perovskite refers to all those materials that show the same crystal structure of $CaTiO_3$, which is represented in **figure 4a,b**.

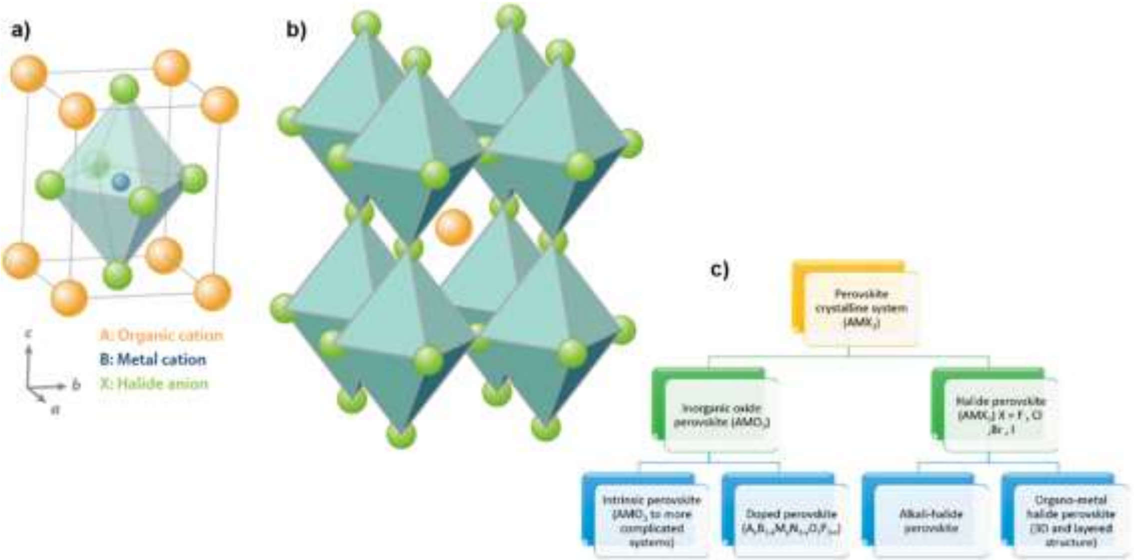

Figure 4: Perovskites crystalline structure and types. (a, b) The unit cell (a) and the resulting crystalline structure (b) of perovskite materials. (c) The family of perovskite materials (figures (a) and (b) are adapted from ref.[29] while figure (c) is taken from ref.[19]).

The generic chemical formula for perovskites is ABX_3, where “A” and “B” are cations while “X” is an anion (which forms chemical bonds with both A and B).[19,29] As shown in **figure 4c**, the perovskite family includes intrinsic oxide materials (where the X anion is O^-) to doped ones or pure halide systems (where X is an halide anion *i.e.*, F^-, Cl^-, Br^- and I^-).[19] In any case, the ideal perovskite unit cell is simple cubic, with A cations in the corners and BX_6 octahedrons at the centre (**figure 4a**); the resulting lattice is shown in **figure 4b**. This kind of structure can be formed only if the ions radii satisfy precise size requirements, that are quantitatively expressed by the Goldschmidt tolerance factor *t*:[30]

$$t = \frac{R_A + R_X}{\sqrt{2}(R_B + R_X)} \tag{1}$$

Where R_A, R_B and R_X are the ionic radii of the A, B and X ions respectively. According to this definition, a perovskite cubic structure is formed only when *t* has a value ranging between 0.8 and 1. Amongst all the existing perovskite materials, the most promising ones for photovoltaic applications are metal halide perovskites, in which A is a monovalent specie, B is a divalent metal cation and X is a halide anion.[19,29] The A anion can further be an inorganic alkali metal (*i.e.*, Li^+, K^+, Na^+, Rb^+, Cs^+) or an organic cation, the most used being methylammonium (MA – $CH_3NH_3^+$) and formamidinium (FA – $H_2NCHNH_2^+$).[29] The former class of materials is referred to *alkali-halide perovskites* while the latter is called *organo-metal halide perovskites*.[19]

PHYSICAL PROPERTIES OF PEROVSKITES

The previous sections made clear the interest that the scientific community has for PSCs. The main reason can be identified to the ionic nature and the good solubility of the precursors materials, that allow the fabrication of SCs with low temperature solution processes (*i.e.,* spin coating, spray coating, doctor blading, *etc.*) that are even compatible with large scale manufacturing.[31] However, many factors can limit the PCE and stability of PSCs (see discussion in the next sections), so there is still the need for further studies and analysis of the physical properties of these class of materials, as hereafter discussed.

FROM LIGHT ABSORPTION TO CHARGE SEPARATION

First of all, it is well known that an ideal absorber material for SCs must have a high absorption coefficient.[31] This feature influences the light harvesting properties of SCs, as well as the resulting V_{oc}.[31] In fact, according to the Shockley-Queisser model, V_{oc} is given by[32]:

$$V_{OC} = \frac{k_B T}{q} \ln\left(\frac{J_{SC} N_D \tau_{eff}}{q n_i^2 d}\right) \quad (2)$$

where k_B is the Boltzmann constant, T is the absolute temperature, q is the elemental charge, J_{SC} is the short-circuit current, N_D is the doping concentration, τ_{eff} is the effective carrier recombination lifetime, n_i is the intrinsic carrier concentration and d is the thickness of the light absorber. From this equation, it is clear that the lower the thickness of the absorber, the higher the V_{OC}. Consequently, materials with high absorption coefficient (> $3 \cdot 10^4$ cm^{-1} in the visible light region for the case of $MAPbI_3$) require thin films to harvest light (perovskites films thickness usually range between 0.3 and 0.6 µm),[33] show higher V_{OC} and benefit from the fact that a smaller quantity of photo-active material is needed (reducing the cost of the SCs).[31]

Moreover, a major loss of V_{OC} is the energy required to separate Frenkel excitons (*i.e.,* electron-hole pair quasi-particles, characterised by specific binding energies – E_b – in the range of 0.2 – 1 eV).[31,34] Obviously, in photovoltaic applications it is pivotal that E_b is as small as possible, as in the case of GaAs and Si where E_b are, respectively, ~4[35] and ~15[36] meV, which are lower than the ambient thermal energy, *i.e.*, ~23 meV (excitons are dissociated without any further loss of energy).[31] For the case of $MAPbI_3$, E_b values range between 2 and 75 meV, depending on the kind of measurement technique.[31] Even if different E_b values have been measured, it has been demonstrated that the generation of free charges in PSCs is the main process occurring in operational conditions (even for the highest E_b value).[37] It is worth mentioning that, in $MAPbI_3$, E_b is influenced by grains dimensions (the highest E_b values being measured for single crystals)[38] and that excitons are usually formed in crystalline domains, while free charges are generated in domains with small grains.[39]

CHARGE CARRIER DYNAMICS

Once charges are generated in a photo-active material, they must travel through it before to be collected at the electrodes. High V_{OC} values can be obtained only if the charge carrier recombination lifetime is long.[31] The charge carrier recombination dynamics is usually described by the following rate equation:[40]

$$\frac{dn}{dt} = G - k_1 n - k_2 n^2 - k_3 n^3 \quad (3$$

where n is the free-charge density, G is the charge-density generation rate, and k_1, k_2 and k_3 are the mono-molecular, bi-molecular and Auger recombination rates, respectively, (these processes are depicted schematically in **figure 5**).[29,40]

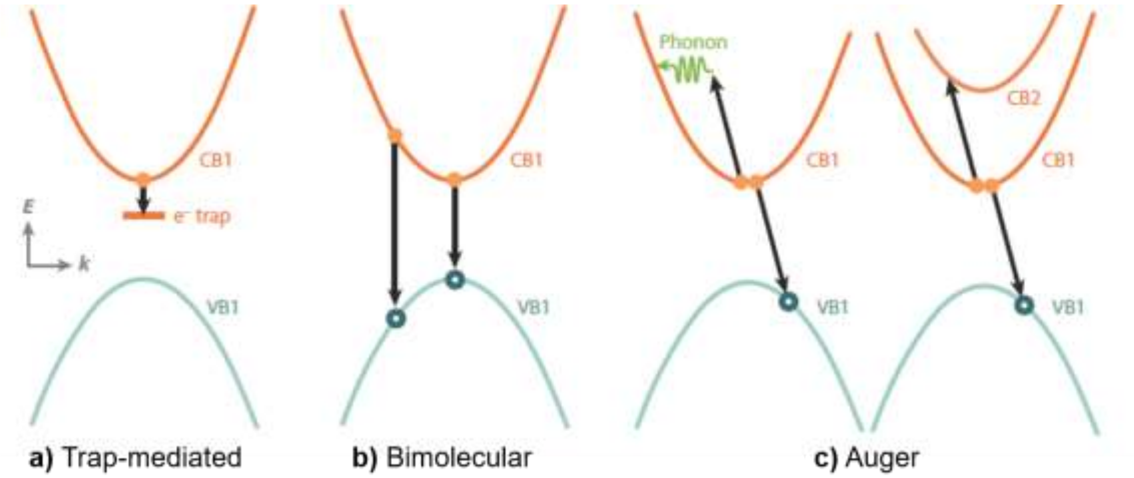

Figure 5: Charge-carrier recombination pathways. E *vs*. k illustrative representation of the main charge-carrier recombination processes: (a) Mono-molecular (or trap-assisted), (b) bi-molecular and (c) Auger recombination (taken from ref.[29]).

The mono-molecular process can be due to two mechanisms: exciton recombination (if formed) or trap-assisted recombination of a charge carrier (either electron or hole).[29] The bi-molecular case refers to electron-hole recombination, while the Auger process describes electron-hole recombination, in which energy and momentum are transferred to either another charge carrier (electron or hole) or used to create or annihilate a phonon.[29] In standard operational conditions (*i.e.,* at 1 sun illumination – 1000 Wm^{-2}), the Auger recombination process is very weak, compared to the other two processes.

In mono-molecular recombination, the nature of the traps (*i.e.,* energetics, densities, *etc*.) strongly depends on the perovskites processing conditions (*e.g*., solution or dual vapour source depositions).[29] Indeed, trap density in $MAPbI_3$ and $MAPbI_{3-x}Cl_x$ have been reported in the range of $10^{15} - 10^{17}$ cm^{-3} in solution-processed films, while lower values have been measured for single crystals ($10^9 - 10^{10}$ cm^{-3}).[29,40] Moreover, trap-densities seem to be more localized at grain boundaries, which is in agreement with the values measured for polycrystalline films.[29] For this reason, reported values of k_1 for $MAPbI_3$ and $MAPbI_{3-x}Cl_x$ range between $1 - 250 \cdot 10^6$ s^{-1}.[29] As concerns other perovskites compositions, it has been shown that trap-assisted recombination channels depend from the specific chemical formulation, since peculiar processes can arise according to the precursors choice.[29] For example, in $MASnI_3$, k_1 values as high as $8 \cdot 10^9$ s^{-1} have been reported and associated to a high density of p-type charge carriers due to the presence of Sn^{4+}.[29,40]

Bimolecular charge-carrier recombination of electrons and holes, being the inverse process of absorption, results in photons emission. In perovskites, measured k_2 values range between $0.6 - 14 \cdot 10^{-10}$ cm^{-3} s^{-1} (comparable to the value for GaAs of $\sim 4 \cdot 10^{-10}$ cm^{-3} s^{-1}).[29,40] The recombination mechanism can be described by the Langevin model, which suggests that this process takes place when an electron and a hole find each other within their Coulombic joint capture radius.[29,40,41] On the basis of this model, the bi-molecular recombination rate is given by:[29,40,41]

$$k_2 = \mu \frac{e}{\varepsilon_0 \varepsilon_r} \tag{4}$$

Where μ is the charge-carrier mobility, e is the elemental electrical charge, ε_0 is the vacuum permittivity and ε_r is the medium relative permittivity. Materials for photovoltaics need high charge-carrier mobility, long carrier diffusion length (L_D) and low recombination rates.[42] Equation 4 sets a fundamental limit to these quantities, since k_2 is related to μ and L_D is given by:[29]

$$L_D = \sqrt{\frac{\mu k_b T}{e(k_1 + n k_2 + n^2 k_3)}} \tag{5}$$

According to this model, $MAPbI_{3-x}Cl_x$ should show L_D ~100 nm but actually a value of 3 µm has been measured[42] and the k_2/μ ratio is 4 orders of magnitude higher than what expected from the Langevin model.[29,40,42,43] These results suggest that non-Langevin recombination occurs in $MAPbI_{3-x}Cl_x$ perovskite and, since the same conclusion has been drawn even for $MAPbI_3$, $MASnI_3$ and $FAPbBr_yI_{3-y}$, it seems to be a universal feature of the perovskite family.[29,40] Perovskites are not the only materials for photovoltaics showing this behaviour. For example, in demixed blends of conjugated polymers with fullerene derivatives[44] and amorphous silicon[45] non-Langevin recombination was also recognized. In both these materials, it was proposed that spatial separation of electrons and holes decreases the probability of recombination.[29] The same idea was used to explain the non-Langevin behaviour of perovskites, since density functional theory calculations of the electronic structures of lead-iodide perovskites showed that the CB minimum consists of 6p orbitals from lead, while the valence band (VB) maximum is due to 6s and 5p orbitals of lead and iodine, respectively.[29,40,42,43] This implies that when an electron and a hole are formed, they are localized on different sites of the unit cells, with a consequent decrease in the overlap of their respective wave-functions (and chance for recombination).[29,40,42,43]

Auger recombination in perovskites is a process that becomes relevant only at high charge carrier densities (*i.e.,* at high illumination fluences), since the values of k_3 range between $0.2 - 10 \cdot 10^{-28}\ \mathrm{cm^6 s^{-1}}$.[29] Being a many-body process, this mechanism strictly depends on the electronic and phononic properties of the considered material.[29] In fact, it was shown that k_3 depends on the exhibited structural phase in $MAPbI_3$, while it increases monotonically in $FAPb(Br_yI_{1-y})_3$ when *y* raises from 0 to 1.[29,40] It is worth mentioning that in concentrator photovoltaics and light emitting applications (*i.e.,* lasers), Auger recombination must be taken into account because of the high charge carrier densities so, for these applications, a proper engineering of perovskites composition and structural phases is needed.[29]

DEFECT PHYSICS OF HYBRID PEROVSKITES

According to the Schockley-Queisser model, the calculation of the maximum V_{oc} in SCs is based on an abrupt and step absorption coefficient at the band gap.[31] However, in realistic conditions, materials always absorb below their band gaps because of many reasons (such as defects or excitonic resonances).[31] The deviation from the ideal behaviour is measured with the Urbach energy parameter, defined as the slope of the exponential part of the absorption coefficient below the band gap,.[31] In $MAPbI_3$, the Urbach energy at room temperature is ~15 meV, which is comparable to that of single crystalline silicon (~11 meV) and GaAs (~7.5 meV).[31] Therefore, $MAPbI_3$ is characterised by a good crystalline structure and a low density of shallow defects (*i.e.,* defects whose energy is just few tens of meV lower than the CB minimum).[29] This is a remarkable result since perovskite materials can be produced from solution processing methods (which are far cheaper than the single-crystal growth of silicon) and yet yield low trap density thin films (10^{15} – 10^{17} cm^{-3} for polycrystalline perovskite, 10^{10} cm^{-3} for single crystals, the latter being comparable to high quality single crystalline silicon).[31] The nature and characteristics of defects make perovskite materials highly tolerant to their presence. Indeed, defects with deep trap energies have high formation energies (so they are unlikely to be formed), while low energy defects are either shallow or introduce energy levels inside the CB or VB.[29,31]

So far, it was shown that perovskites are point-defect tolerant materials. However, it is well known that extended defects (*i.e.,* grain boundaries and interfaces) can occur because of many reasons, *e.g.*, the evaporation of a fraction of organic components of the perovskite during annealing.[31] The dimension and orientation of crystalline grains affect the charge carrier dynamics, since some crystalline growth-directions give rise to electrically charged planes.[31] In particular, it was shown that a difference in V_{oc} of 0.6V has been measured by photoconductive atomic force microscopy, performed on the different facets of the same grain,[46] but it is still not clear if this differences in V_{oc} at the microscopic level can affect the performances of devices (including the presence of transporting layers).[31]

TUNING PEROVSKITE PROPERTIES

One of the most attractive properties of metal halide perovskites is the fact that their band gap can be tuned by changing their chemical composition.[47] **Figure 6** shows the normalized photoluminescence (PL) for a variety of perovskite materials: the peak position (and consequently, the band gap) can be tuned from 3.06 eV ($CsPbCl_3$) to 1.15 eV ($MASn_{0.8}Pb_{0.2}I_3$).[47]

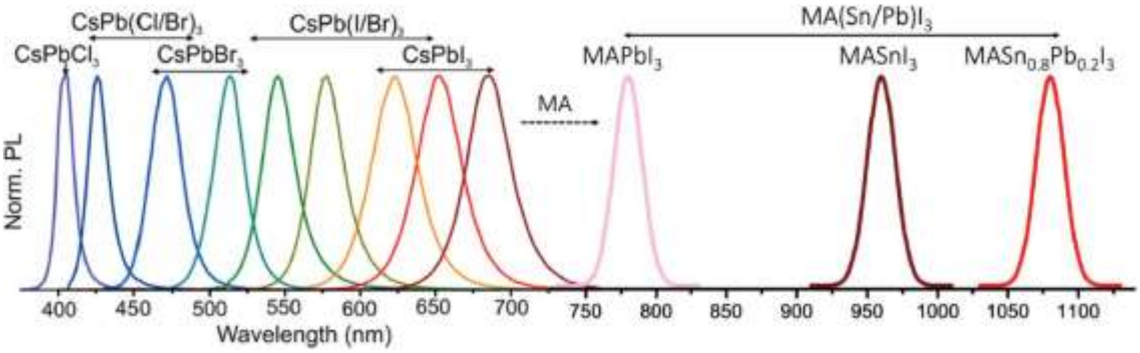

Figure 6: Band gap tunability of perovskite materials. Representative PL spectra of chemically different perovskites, showing that a proper precursors engineering can lead to desired opto-electronic properties (adapted from ref.[47]).

This is achieved by mixing different metal atoms (*i.e.,* Pb, Sn or Ge) and/or halides, since the VB maximum and CB minimum depend on the nature of the B-X bonds.[19] In this way, it is possible to create a plethora of materials with band gaps suitable for single junction SCs (as in the case of $MAPbI_3$) and even for multi-junctions SCs (*i.e.,* devices where materials with different band gaps are stacked together to increase the amount of absorbed solar radiation).[47] However, mixed-halides perovskites suffer from photo-induced phase segregation (*i.e.,* the formation of iodide-rich domains due to halides migration)[48] that causes a decrease of the open-circuit voltage (V_{oc} *i.e.*, the voltage measured at zero net-current flow). In particular, migrations can occur at operating conditions (due to the applied electric field) mainly because of the presence of crystalline defects (*i.e.,* vacancies and interstitial defects).[47,49] During biasing conditions, defects can accumulate at the contacts interfaces, leading to a formation of Debye layers that screen the SC built-in potential.[47] This phenomenon has been related to the hysteresis behaviour of PSCs, *i.e.,* the occurrence of different current density-voltage (J-V) curves, depending on the scan direction (forward and backward).[47,50] Halide segregation can be mitigated by using multiple A-site cations but, according to the composition, the resulting perovskites suffer from a complex ion dynamics and photo-active phase instability, so careful chemical composition engineering is needed. [47]

Indeed, currently multiple cations (Rb, Cs, MA and FA) and halides (Br and I) perovskites have shown the highest PCEs and stabilities.[47,51] Compositions with only few ions would make PSCs fabrication easier, but the resulting structural and optoelectronic properties usually are not optimal for photovoltaic applications. For example, FA- or Cs-based halide perovskites have been prepared and demonstrated as materials for photovoltaics.[23,24,47,52] They can both form a “black” photo-active perovskite phase, but it is metastable and turns (usually in some hours) into a yellow, photo-inactive, phase.[23,47,52] The instability of single- cation-based perovskites (MA-, FA- and Cs) has been faced by using double-, triple- and even quadruple- cations compositions (*i.e.* by mixing Rb, Cs, MA and FA),[47] the triple- and quadruple- cases being the most promising for stabilizing a black, photo-active, phase even at room temperature.[47] Thus, huge efforts have been focused on engineering the perovskite composition.

LIMITS OF PEROVSKITES SOLAR CELLS

The outstanding advances in PSCs led the scientific community to assess the possibility to commercialize them. However, it soon became clear that the PSCs suffer from low stability for many reasons.[53,54] Before discussing them, it is useful to mention that commercial SCs must guarantee 25 years of stability.[53,54] Since testing for 25 years is not either feasible nor practical, accelerated tests have been proposed in which the SCs are subjected to both high temperature and continuous sunlight exposure (in order to reproduce the effect of 25 years-aging).[54] In particular, the International Electrotechnical Commission (IEC) proposed, for thin-film SCs, the IEC 61646 standards where the devices are kept at 85 °C at 1 sun illumination: if after 1000 h of testing the SCs show a decrease of PCE which is smaller than 20%, the test is passed.[54] However, literature results often use different stability tests, so comparisons can be troublesome. For this reason, it is recommendable to describe properly the used stability conditions.

Instability of PSCs is due to many reasons, the main ones being structural, thermal and atmospheric.[53] The first one arises because of the ionic nature of the perovskite materials, since the precursors can organise in space forming different crystalline or amorphous structures that are not suitable for SCs applications.[53] From the structural point of view, perovskite materials must exist in photo-active phases during operational conditions. In fact, tilting of the BX_6 octahedra can induce a variety of structural phases (cubic, tetragonal, trigonal and orthorhombic)[29,55] and, consequently, transitions between them that can deeply influence the resulting charge-carriers dynamics.[29] For example, $MAPbI_3$ shows a cubic structure above ~330 K, a tetragonal phase between ~330 K and ~160 K and finally an orthorhombic phase below ~160 K (**figure 7**).[23,29]

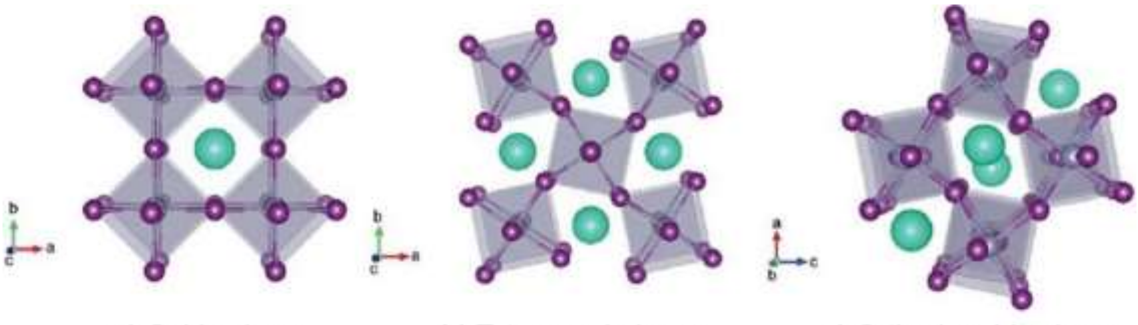

a) Cubic phase **b)** Tetragonal phase **c)** Orthorhombic phase

Figure 7: Structural phases of perovskite materials. (a) cubic phase, (b) tetragonal phase and (c) orthorhombic phase of perovskite materials (adapted from ref.[53]).

While the tetragonal-to-orthorhombic phase transition is not a practical issue (since it occurs at low temperatures *i.e.,* ~160 K) the tetragonal-to-cubic phase transition emerges during operational conditions.[23,29] Although it has been shown that the tetragonal-to-cubic transition gives rise only to small bandgap, carrier lifetime and mobilities differences,[56,57] the presence of the MA^+ cation is of first concern because it can easily lose a proton in humid environments, forming volatile compounds.[52] This process is accelerated by heating, even in inert conditions, which introduces the need for thermal stability.[53] In fact, SCs must stay operative in a wide range of temperatures (from -40 to 85 °C), according to the place where they are used.[53] As concerns $MAPbI_3$, it has been shown that at 85 °C there are strong signs of degradation in inert conditions (*i.e.,* evolution of volatile HI and CH_3NH_2 (MA)) and this process is accelerated in the presence of oxygen or water because of the formation of hydrogen bonds that interfere with the chemical bonds of the organic cations.[58] For this reason, $MAPbI_3$ cannot be used as a material for stable and long term PSCs. At this point, the common sense suggests to consider perovskite compositions where the MA^+ cation is not used. Indeed, it has been shown that fully inorganic perovskites (*i.e.,* $CsPbI_2Br$, showing no sign of decomposition at 180 °C for more than 30 min, while $MAPbI_3$ decomposes in 5 min at the same temperature)[59,60] as well as mixed cations perovskites (*i.e.,* $FA_{0.83}Cs_{0.17}Pb(I_{1-x}Br_x)_3$ stable for 6 h at 130 °C)[61] show great thermal stability.

Temperature is not the only external factor that can influence PSCs performance, with oxygen and moisture being the most detrimental sources of instability.[53] For the $MAPbI_3$ case, it is believed that the oxygen degradation occurs because molecular oxygen turns into superoxide species, by accepting a photo-excited electron, and deprotonate MA^+.[62] As concerns moisture degradation, in $MAPbI_3$ perovskites the MA^+ cation can lose a proton (owing to hydrogen bonding with H_2O) and turn into the volatile MA, leading to the decomposition of the perovskite structure.[53] It is worth noting that moisture instability is experienced in both sunlight and dark conditions, while oxygen degradation is a photo-induced process. In particular, perovskite degradation by oxygen occurs only under sunlight illumination, while water induced degradation arises even in dark conditions.[53] These two sources of instability can be dealt with by using mixed A-cations, as demonstrated for the case of $FA_{0.83}Cs_{0.17}Pb(I_{0.6}Br_{0.4})_3$ (which show a stability of 650 h under sunlight, in ambient conditions, while $MAPbI_3$ degrades in less than 100 h).[63]

The stability of PSCs must be also considered from a device perspective, by judicious choice of the electrodes, since they represent the part of the device which is exposed to all the external sources of instability.[53] In particular, metal electrodes (*i.e.,* Ag, Al and Au) are good shields against oxygen and moisture, because they are dense and impermeable materials.[53] However, metal atoms as well as iodides can diffuse and migrate through the selective extraction layers, forming black metal halides (especially in the case of Ag and Al) which do not act as electrodes (this process is even boosted by applied electric field and high temperatures).[64,65] In particular, it was shown that at 75 °C, Au can penetrate into spiro-OMeTAD.[65] Many strategies have been proposed to overcome this hurdle, such as the use of interlayers between spiro-OMeTAD and Au[65] or the use of different HTM (*i.e.,* PTAA).[51] However, these devices configurations still use Au as electrode, which is not viable for the commercialization of PSCs, so more efforts are needed to implement cheaper electrodes. In this context, Bush *et al.* used ITO as top and bottom electrodes, since it is not reactive and impermeable to both oxygen and moisture.[66] In this work, they show that the resulting $MAPbI_3$-based PSCs are stable against both atmospheric and thermal perturbations. The thermal stability has been explained as due to the ITO top electrode, that is impermeable to HI and MA (discussed previously, when talking about thermal stability of PSCs): an equilibrium arises between sublimation and inclusion of these compounds, slowing down the perovskite degradation. This work showed that a solution to the top electrodes interface can be found by using ITO, but PSCs still need a proper encapsulation to pass the IEC standard tests. In particular, Bush *et al.* showed that $FA_{0.83}Cs_{0.17}Pb(I_{0.83}Br_{0.17})_3$ PSCs, when sealed with commercial procedures (*i.e.*, by using glass as encapsulating layers and ethylene vinyl acetate or surylyn as adhesive binders), can pass the IEC protocol 61215 (1000 h exposure to sunlight, at 85 °C and 85% relative humidity) and actually improve the performances.[67] Although other tests must be performed and passed (such as UV light exposure, temperature cycling, electrical stresses, *etc*.),[53] this result paved the way through a practical solution and assessment to industrial requirements.

The strategies so far discussed deal with the compositional engineering of the perovskite layer and the careful choice of charge extraction layers/electrodes/encapsulations. Another route that can be followed, for improving perovskites performances and stability, is the use of low-dimensional perovskites, which have shown (when combined with regular perovskites) record-value of stability of more than 1 year, paving the way for a possible solution to perovskite device instability.[54]

FROM 3D TO 2D PEROVSKITES

More in details, low-dimensional perovskites, specifically of the Ruddlesden-Popper kind, are characterised by the chemical formula $R_2A_{n-1}B_nX_{3n+1}$, where A, B and X have the same meaning as discussed so far, R is an additional bulky organic cation and n defines the dimensionality of the resulting structure (that can be tuned with a careful control on the precursors stoichiometry).[54,68] As stated previously, Goldschmidt tolerance factor sets a limit to the three-dimension and type of A-site cations that can be used to form a 3D perovskite structure. This is due to the fact that big cations would separate the planes of BX_6 octahedra, disrupting the 3D structure. In 2D perovskites, the R cations act as spacers between the inorganic layers that are, consequently, separated in planes made up by 1 single layer of BX_6 units, so n=1 in 2D perovskites (**figure 8**).[54,69]

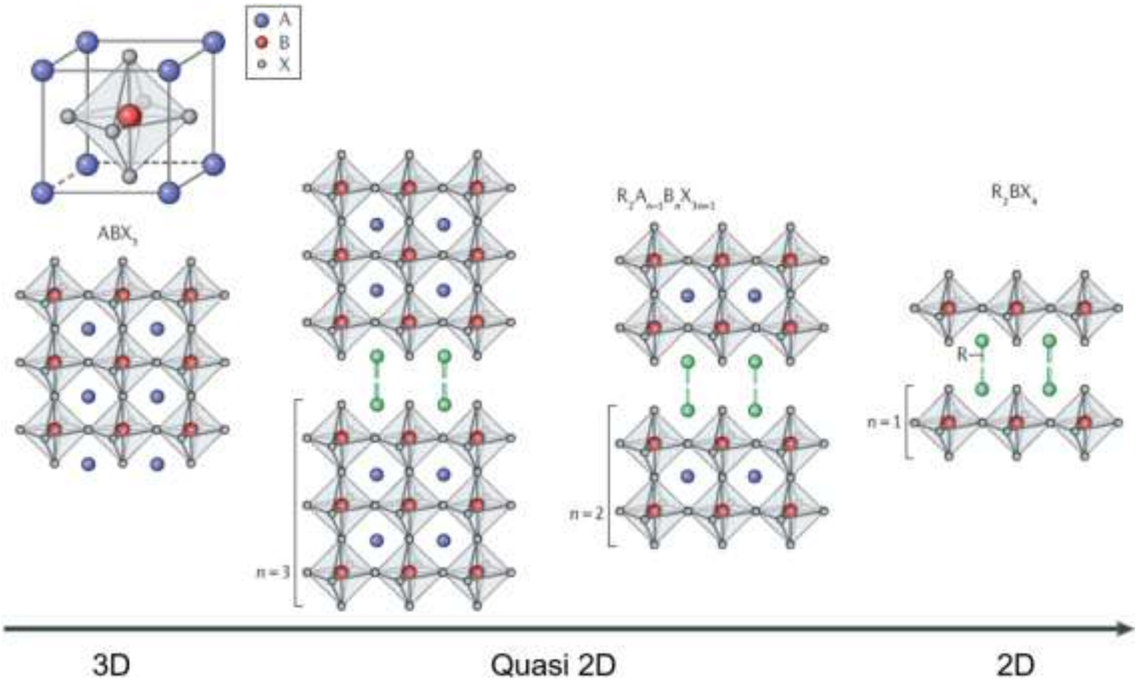

Figure 8: From 3D to 2D perovskites. Structural evolution of the perovskite structure from pure 3D (where the crystal is made up by corner sharing BX_6 octahedra and A-cations in the interstices) to quasi 2D (where the presence of bulky cations leads to the formation of layers with n-BX_6 units) to pure 2D (where every single layer of BX_6 octahedra is alternated by the R cations) (adapted from ref.[54]).

If n > 1, the resulting structure is named quasi-2D (the 3D case correspond to n = ∞). The 2D (and quasi 2D) perovskite structure shown in **figure 8** is named Ruddlesden-Popper structure and is made up by two R molecules, each one interacting with the inorganic layers only on one side, so a “Van der Waals” gap is formed between the two adjacent R cations (**figure 9**).[70,71]

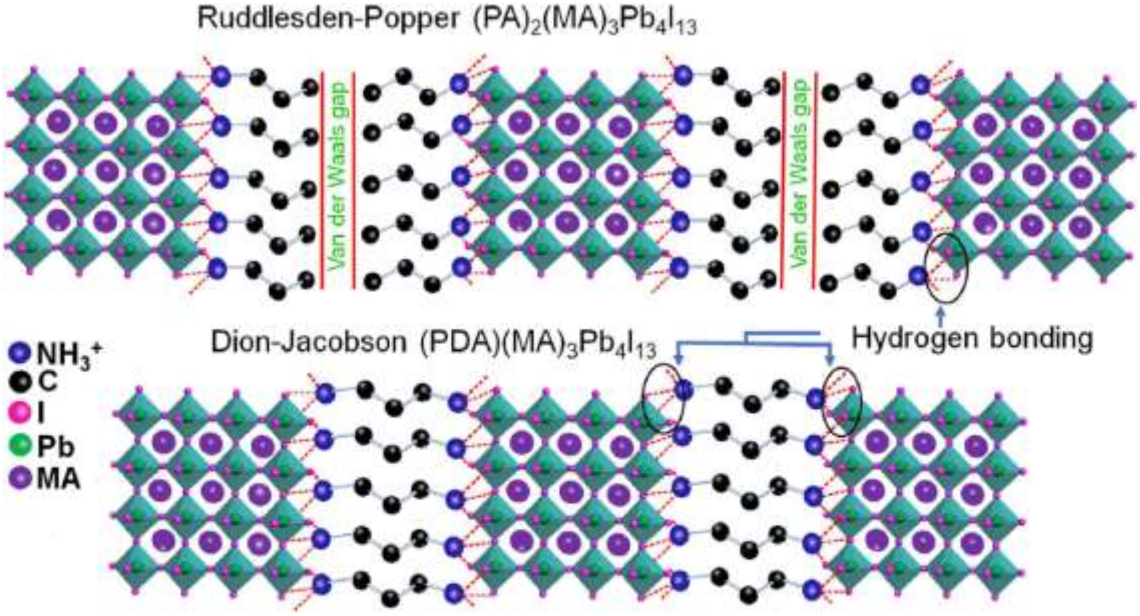

Figure 9: Ruddlesden-Popper and Dion-Jacobson low dimensional perovskites. Schematic representation of the Ruddlesden-Popper (up) and Dion-Jacobson (down) structure of quasi-2D perovskite structure (n=4). PA and PDA represent propylamine and 1,3-propanediamine cations, respectively (taken from ref.[71]).

This gap can be eliminated by using compounds with two amino groups, that can form hydrogen bonds on both ends of the same molecule with the inorganic layers.[71] In this way, the Van der Waals gap is not formed and the resulting structure is referred to as Dion-Jacobson type (**figure 9**), with chemical formula $RA_{n-1}B_nX_{3n+1}$ (*i.e.*, there is only one R bulky cation versus the two present in the Ruddlesden-Popper case).[71]

The interest in low-dimensional perovskites raised because of their enhanced environmental stability, which is a consequence of the hydrophobic nature of the organic cations that can avoid the penetration of water inside the perovskite lattice.[72,73]

In the present work, with the aim to develop efficient and stable solar cells, 2D and quasi-2D perovskites of the Ruddlesden-Popper type have been considered. Many organic cations can be used to form this kind of structure, such as ammonium valeric acid (AVA^+), butylammonium (BA^+), naphthylmethylammonium (NMA^+), phenylethylammonium (PEA^+), phenylmethylammonium (PMA^+), *etc*.[54,69] In fact, without considering the limits raising from the Goldschmidt tolerance factor, a plethora of cations become available for 2D perovskites formation, allowing the tuning of the resulting physical properties.[54]

Indeed, 3D and 2D perovskites are characterised by completely different opto-electronic properties, due to the quantum confinement arising in low dimensional materials.[54] First of all, 2D perovskites band gaps are higher with respect to the 3D counterparts (~2.3 eV in $(PEA)_2PbI_4$, ~1.52 eV in $MAPbI_3$),[54] moreover the structures depicted in **figure 8** and **figure 9** show that quasi 2D and 2D perovskites form quantum wells, because of the insulating nature of the bulky organic cations.[54,68] This structure causes the formation of stable excitons, with E_b as high as hundreds of meV (~200 meV in $(PEA)_2PbI_4$, which is far higher than room temperature thermal energy ~23 meV).[54,68] It is worth mentioning that as the number of inorganic layers increases from pure 2D (n=1) to 3D (n=∞) E_b decreases.[54] According to the choice of precursors and their stoichiometry, the excitonic features can be changed, which can be used for the design of light-emitting devices with on-demand properties (for example, $(PMA)_2PbI_4$ and $(PEA)_2PbI_4$ have been demonstrated as candidates for, respectively, green and violet LEDs).[54] The high exciton binding energy is not the only disadvantage of 2D perovskites for SCs applications. In fact, the crystallization of 2D perovskites solutions usually leads to a preferential orientation of the inorganic layers which is parallel to the substrate.[54] In this way, charge transport is obstructed by the non-conductive R-cations layers, limiting the highest achievable PCE of the resulting devices. To overcome this issue, more research addressing the nucleation mechanism is needed, in particular it was shown that in the case of $(BA)_2(MA)_3Pb_4I_{13}$ vertical stacking has been achieved by a careful optimization of the annealing steps, which lead to inhomogeneous nucleation at the liquid/air interface and a PCE of 7.9%.[74] A further strategy that helps preferential orientation is the engineering of the bulky organic cation. For example, the use of iso-BA^+ cation in $(BA)_2(MA)_3Pb_4I_{13}$ resulted in a SC with a PCE of 8.82%, three times higher than the results obtained by using the isomer n-BA^+ (remarkably, stability of 800 h, at 20 °C and 60% relative humidity has been detected in devices without encapsulation).[75] From these two previous examples, it is clear that low n-values quasi-2D perovskites are not good candidates to achieve high efficiencies.[54] Increasing the number of layers is one of the most promising solution to this hurdle, but affects negatively the stability. For example, in $(PEA)_2(MA)_{n-1}Pb_nBr_{3n+1}$ (with n=60) 15.3% certified efficiency has been measured, but with a stability of 60 and 14 days in, respectively, low humidity environment and 55% relative humidity.[76]

To take advantage of both high stability of 2D perovskites and high efficiency of 3D perovskites, 3D/2D junctions have been proposed.[54] In particular, 3D/2D interfaces were prepared on top of triple cation perovskite ($Cs_{0.1}FA_{0.74}MA_{0.13}PbI_{2.48}Br_{0.39}$) by dynamically spin-coating PEAI in isopropanol.[77] The resulting devices showed a PCE higher than 20% and retained 85% of this initial value, under 1 sun illumination for 800 h, in ambient environment at 50 °C.[77] In another work, AVA^+ was used to create a composite 2D/3D structure ($(AVA)_2PbI_4/MAPbI_3$) in n-i-p architecture, where the AVA^+ cations anchor to the meso-porous TiO_2, create a vertically stacked 2D

$(AVA)_2PbI_4$ perovskite and induce the crystallization of a highly oriented $MAPbI_3$ layer.[78] Monolithic devices with both laboratory-scale dimensions (0.5 cm^2) and large modules (10x10 cm^2) were fabricated and showed a world record stability of more than 1 year (no loss in efficiency was detected for 10000 h, at 1 sun illumination for the whole day, at 55 °C, sealed in ambient atmosphere).[78] Although the module efficiency is ~10%, this work paved the way for the academic and industrial interest in scaling-up technologies for PSCs.

METHODS

PRODUCTION AND CHARACTERIZATION OF MOS_2 AND WS_2 DISPERSIONS

Both MoS_2 and WS_2 dispersions were prepared by LPE in 2-propanol (IPA, Sigma Aldrich). Briefly, 50 mg of bulk crystals (MoS_2 or WS_2, HQ graphene) were sonicated (sonic bath VWR) for 6 h in 50 mL of IPA. The resulting heterogeneous dispersion was centrifuged at 770 g for 30 min (Optima XE-90 ultracentrifuge, Beckman Coulter SW32Ti rotor), to isolate the exfoliated flakes. The lateral size and thickness of the MoS_2 and WS_2 flakes were characterized by TEM and AFM, respectively.

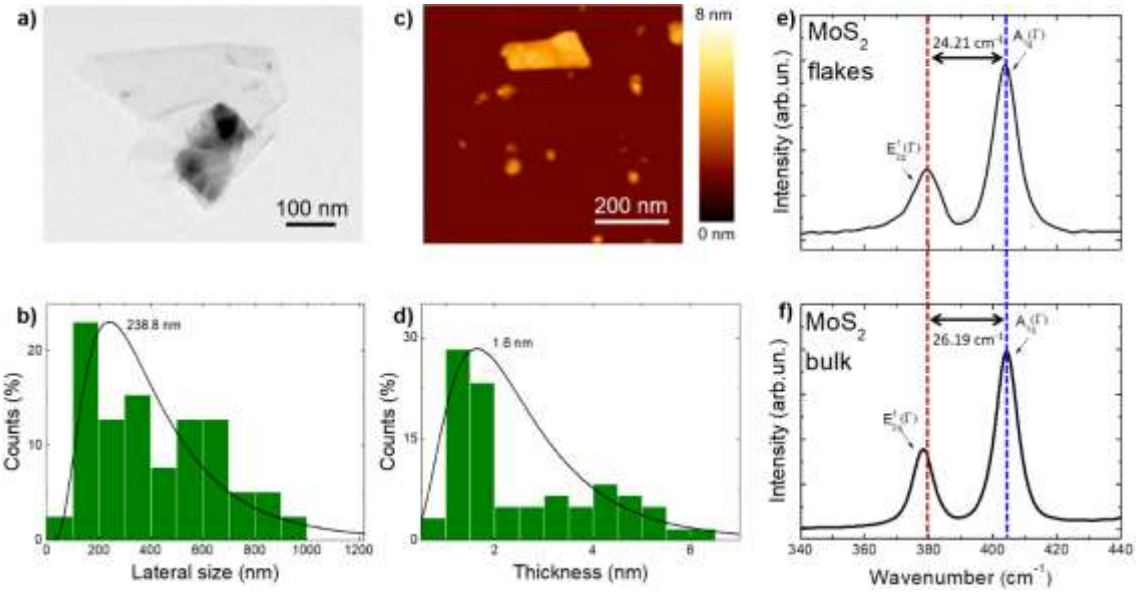

Figure 10: Morphological and structural analysis of the MoS_2 flakes. (a, b) Representative TEM image of MoS_2 flakes (a) and statistical analysis of the lateral size (b). (c, d) AFM image of MoS_2 flakes (c) and statistical analysis of the thickness (d). (e, f) Raman spectra of MoS_2 flakes (e) and MoS_2 bulk (f).

Figure 10a shows a TEM image example of representative MoS_2 flakes. The statistical analysis (performed on 40 flakes) is reported in **figure 10b** and follows a log-normal distribution (typical of fragmented materials),[79] peaking at 238.8 nm. **Figure 10c,d** report, respectively, an AFM image of a representative MoS_2 flake and the thickness statistical analysis (performed on 40 flakes): the data follow a log-normal distribution trend with a 1.58 nm peak. The thickness of the flakes, as well as the presence of defects, can be evaluated through Raman spectroscopy too. **Figure 10e,f** show the Raman spectrum of MoS_2 flakes and bulk, respectively. The $\mathrm{E}^1_{2g}(\Gamma)$ mode is due to the in-plane displacement of Mo atoms, while the $\mathrm{A}_{1g}(\Gamma)$ is associated to the out-of-plane displacement of S atoms.[80] In MoS_2 flakes, the Raman contribution from the $\mathrm{E}^1_{2g}(\Gamma)$ mode is softer (379.2 cm^{-1}) than the bulk counterpart (377.9 cm^{-1}), while the peak associated to the $\mathrm{A}_{1g}(\Gamma)$ mode shows no difference to the bulk case. The frequency difference between these two peaks changes from ~26 cm^{-1} for the bulk to ~24 cm^{-1} in the flakes. This trend is indicative of a reduction of the MoS_2

flakes thickness, as the frequency difference decreases to 19 cm^{-1} for the monolayer case.[81]

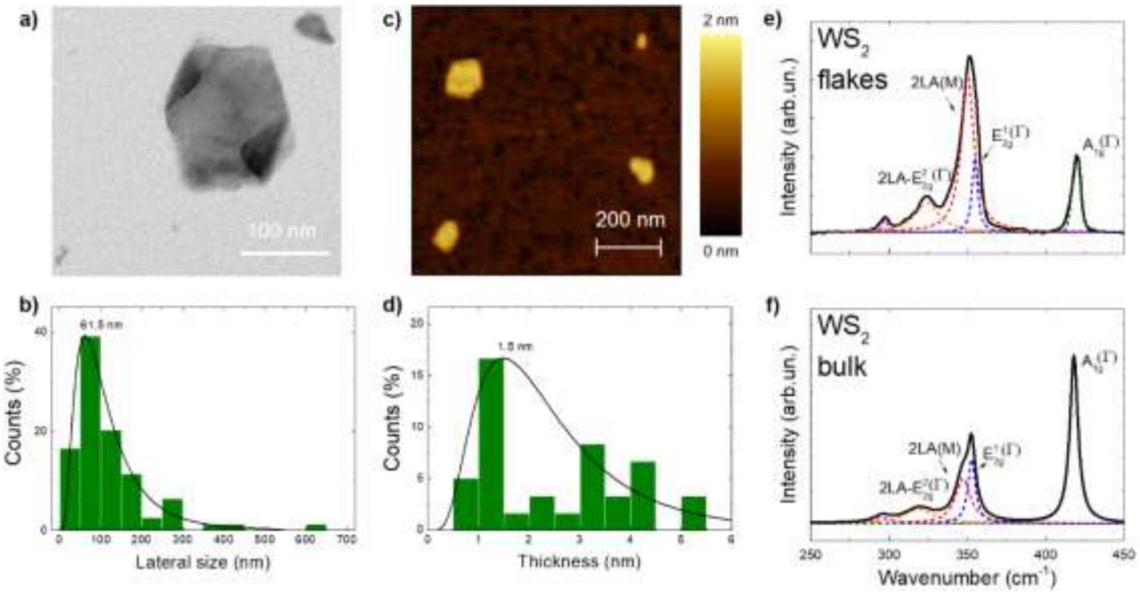

Figure 11: Morphological and structural analysis of the WS_2 flakes. (a, b) Representative TEM image of WS_2 flakes (a) and statistical analysis of the lateral size (b). (c, d) AFM image of WS2 flakes (c) and statistical analysis of the thickness (d). (e, f) Raman spectra of WS_2 flakes (e) and WS_2 bulk (f).

The morphological and structural characterization of WS_2 is reported in **figure 11**. In **figure 11a,b** a TEM image and the lateral size statistical analysis of WS_2 flakes (performed on 40 flakes) are reported. **Figure 11c,d** show an AFM image and the corresponding thickness statistical analysis (using data from 40 flakes). Both statistics follow log-normal distributions with peaks at ~61.5 nm and ~1.5 nm for lateral size and thickness, respectively. To further confirm these results, Raman spectra were measured for both the WS_2 flakes (**figure 11e**) and bulk (**figure 11f**) samples. The main contributions in the Raman spectrum of WS_2 are associated to the $\mathrm{E}^1_{2g}(\Gamma)$, $\mathrm{A}_{1g}(\Gamma)$ (at the Brillouin zone centre, due to in-plane displacement of W and S atoms and to the out-of-plane displacement of S atoms, respectively)[80] and to the longitudinal acoustic mode at the M point of Brillouin zone, 2LA(M).[80] In thin layers, the position of the $\mathrm{E}^1_{2g}(\Gamma)$ associated peak is blue-shifted compared with the bulk case (because of the reduced dielectric screening of the Coulomb interaction).[80] The deconvolution of the Raman spectra shown in **figure 11e,f** allows the determination of this peak position at 354.6 cm^{-1} in the flakes and 352.7 cm^{-1} in the bulk case, confirming the reduced thickness of the WS_2 flakes.

RESULTS AND DISCUSSION

THE USE OF 2D MATERIALS IN PEROVSKITE SOLAR CELLS

INTRODUCTION

With the aim to improve the overall stability and the hole collection of PSCs, we engineered the quasi 2D/HTM and 3D/2D/HTM interfaces by using MoS_2 or WS_2. In fact, 2D materials such as graphene, its derivatives (*i.e.,* graphene oxide, reduced graphene oxide, *etc*.) and TMDCs have already been introduced (as thin layers or as additives in some layers) in both n-i-p and p-i-n PSCs.[82–84] For example, MoS_2 flakes (produced by LPE and deposited by spin coating) were used as interlayer between perovskite ($MAPbI_3$) and spiro-OMeTAD to improve the energy band alignment at the perovskite/HTM interface and to increase the stability of mesoscopic PSCs.[85] As a result, the starting PCE of 13.3% dropped to 12.4%, after 550 h (while the reference devices showed a decrease from 14.2% to 9.3%).[85] The increased stability was demonstrated on both small (0.1 cm^2) and large (1 cm^2) area device. A very high PCE (13.4%) was recently demonstrated in SCs modules (active area 108 cm^2) through careful interfaces engineering of mesoscopic PSCs.[86] Moreover, the device architecture (FTO/c-TiO_2+graphene/m-TiO_2+graphene/triple-cation-perovskite /MoS_2 flakes/spiro-OMeTAD/Au) led even to PCE retention of 75%, under thermal stress at 65 °C, for 1000 h.[86] In another work, reduced graphene oxide was engineered by functionalizing it with (3-mercaptopropyl)trimethoxysilane hybridised with MoS_2 quantum dots.[87] This compound was used as interlayer, in mesoscopic n-i-p PSCs, between $MAPbI_3$ and spiro-OMeTAD and led to devices with an average PCE of 18.76% (17.53% for references without 2D materials) and increased stability over 1000 h of tests (*i.e.*, only an 8.8% reduction of PCE has been detected *vs.* a 24.6% reduction in the references).[87] The use of MoS_2 was successful even in p-i-n structure, where it was shown that interlayers of MoS_2, between PTAA and $MAPbI_3$, increase the efficiencies of large area (0.5 cm^2) devices from 10.64% to 13.17%.[88] Increased stability (at ambient conditions, with 50-60% relative humidity) was reported for encapsulated devices, with an increase of T_{80} (*i.e.*, the time required for a device to retain 80% of its efficiency) from 171 h (for the reference devices) to 568 h.[88]

From the above examples, it is clear that the proper engineering of the SCs interfaces by using 2D materials is a viable option for the commercialization of PSCs. With this in mind, this chapter is devoted to the presentation of the results concerning two projects about the use of low dimensional perovskites (either quasi 2D and 2D) and 2D materials in SCs (to the best of our knowledge, this is the first time that these materials are used together).

The first research focuses on quasi 2D-based devices, while in the second one the perovskite layer is a hybrid 3D/2D material. These results are preliminary, since these projects are still in progress at the time of this thesis submission.

QUASI 2D PEROVSKITES

As discussed in the previous sections, the interest in quasi 2D perovskites raised because of their enhanced environmental stability compared with their 3D counterparts. However, their maximum PCEs is still lower than those of 3D perovskites. Therefore, it is crucial to find some strategies overcoming this hurdle.

This project aimed to use WS_2 flakes to prepare an interlayer between quasi 2D perovskite and spiro-OMeTAD, to improve the hole collection of the quasi 2D perovskite. The choice of WS_2 is due to its VB maximum (-5.48 eV)[89] which is close to the VB maximum of the quasi 2D used in this work: $(PEA)_2(MA)_{39}Pb_{40}I_{121}$ (*i.e.*, n=40), with a VB maximum at -5.23 eV.[90]

The architecture of the devices is shown in **figure 12a**. For their fabrication, FTO glass substrates (Nippon sheet glass) were cut and cleaned with de-ionized water and soap solution (Hellmanex), de-ionized water, acetone, and IPA. Ozone treatment was performed (for 15 min) to take rid of the organic residues after cleaning. The next step was the deposition of a c-TiO_2 layer by spray pyrolysis deposition, at 450 °C, of a titanium di-isopropoxide solution (Sigma-Aldrich) diluted in IPA (0.6 mL: 9 mL). The quasi 2D solution was prepared by dissolving stoichiometric amounts of PEAI, MAI and PbI_2 according to the molecular formula $(PEA)_2(MA)_{39}Pb_{40}I_{121}$, in a 1:1 volume ratio of γ-butyrolactone:dimethyl sulfoxide (DMSO), at an optimised PbI_2 concentration. This solution was deposited, in a nitrogen glove box, with optimized parameters for the spin coating program, anti-solvent treatment and annealing. After this, WS_2 flakes were deposited on top of the active layer by multiple-times spin coating and sequent annealing, after each spin-time, at 100 °C for 1 min (as suggested by other works in the literature[85,88]). The spiro-OMeTAD was deposited on top of the perovskite layer through spin-coating at 4000 rpm for 30 s. The spiro-OMeTAD solution (70 mM) was prepared by dissolving in chlorobenzene 4-tert-butylpyridine (TBP), Li-bis(trifluoromethanesulfonyl)imide (Li-TFSI) in acetonitrile, and Co[*t*-BuPyPz]$_3$[TFSI]$_3$ (FK209) in acetonitrile at a molar ratio of spiro:FK209:Li-TFSI:TBP of 1:0.03:0.5:3.3. The Au metal contact was deposited through thermal evaporation (70 nm).

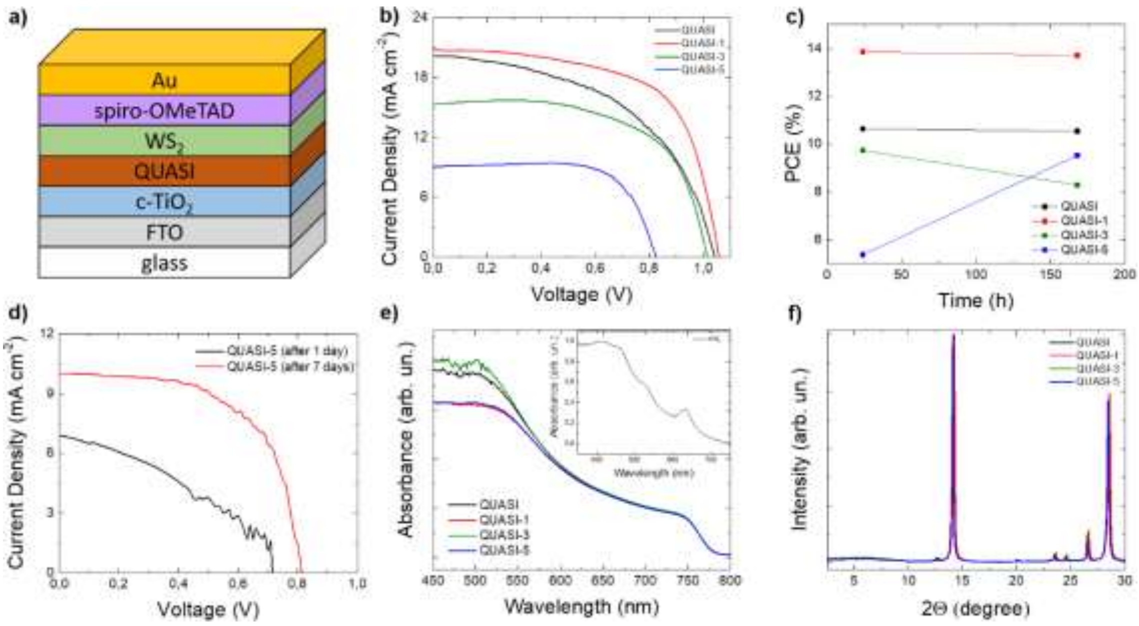

Figure 12: Quasi 2D based PSCs with WS$_2$. (a) Schematic representation of the devices architecture. (b) J-V curves of the best performing devices. (c) Time evolution of the best devices PCEs. (d) Effects of aging on the J-V curve of the worst QUASI-5 device (showing an increase of PCE from 1.77% to 5.37%). (e, f) UV-Vis absorption (e) and XRD (f) spectra of all the discussed quasi 2D devices. The inset to figure (e) shows the absorption spectrum of WS$_2$ flakes dispersion.

The reference devices (*i.e.*, those where WS$_2$ flakes were not deposited) from now on are referred to QUASI, while the devices where WS$_2$ flakes were deposited 1, 3 and 5 times are referred to QUASI-1, QUASI-3 and QUASI-5, respectively. **Table 1** reports the average values concerning the performance parameters of the last produced batch (two weeks before the submission of this work), measured the day after their production, while **figure 12b** shows the comparison of the J-V curves for all the discussed conditions.

	QUASI	QUASI-1	QUASI-3	QUASI-5
J_{SC} (mA cm^{-2})	18.56 ± 1.88	17.51 ± 3.54	14.71 ± 0.85	8.19 ± 1.43
V_{OC} (V)	1.01 ± 0.02	1.03 ± 0.02	0.96 ± 0.10	0.81 ± 0.12
FF (%)	56.53 ± 7.06	61.56 ± 10.35	59.30 ± 6.50	58.25 ± 15.80
PCE (%)	10.60 ± 0.05	10.76 ± 1.85	8.46 ± 1.60	4.00 ± 1.56
Best PCE (%)	10.64	13.86	9.74	5.37

Table 1: Average performance parameters values of QUASI, QUASI-1, QUASI-3 and QUASI-5 devices.

Data in **table 1** show that one-time spin coating of WS_2 flakes, leads to the highest efficiencies as the presence of WS_2 seem to affect positively the devices V_{OC}. However, since the concentration of the WS_2 dispersion is not high (0.18 g L^{-1}), it is possible that only few flakes are left on top of the QUASI surface, leading to no practical difference compared to the reference QUASI (in fact the standard deviation for the QUASI-1 performance parameters are high, so the highest 13.86% was not reproducible in this batch). For what concerns the QUASI-3 and QUASI-5 devices, the measurements of as-produced device evidenced that spin coating WS_2 flakes for more than one time has a detrimental effect on the device performances. After these measurements, the devices were stored in an Ar dry box, in dark conditions, and measured again after one week. The comparison between the PCEs of the best performing devices measured after 1 and 7 days is shown in **figure 12c**. While the QUASI and QUASI-1 devices show a stable efficiency, QUASI-3 is experiencing a slight decrease of PCE (that can be due to some issues related to the device itself) but, more interestingly, QUASI-5 is showing an increase from 5.37% to 9.53% (*i.e.*, ~77% increase). This effect was not observed in any other case (QUASI references included) and was confirmed in other QUASI-5 PSCs. For example, the worst QUASI-5 device showed an increase from 1.77% to 5.57% (*i.e.*, ~200% increase, **figure 12d** reports the comparison of the J-V curves for these two cases). As stated previously, these are preliminary results, so further research is needed to confirm and explain the processes leading to these observations.

UV-Vis absorption and X-Ray Diffraction (XRD) were performed on samples prepared in device configuration (*i.e.*, by depositing the quasi 2D and quasi 2D/WS_2 on top of all the layers used for the PSCs), to assess the structural and optical properties of the perovskite layer (**figure 12e,f**). Both absorption and XRD measurements show that the presence of WS_2 flakes, on top of the quasi 2D, does not affect the structural and optical properties of the perovskite layer. Thus, any effect that will be detected during the following measurements, can be associated only to the presence of the WS_2 layer and not to any induced modification of the quasi 2D properties. Further studies on the interface charge dynamics are ongoing.

3D/2D PEROVSKITES

In this project, dispersions of MoS_2 and WS_2 were used in devices with a 3D/2D perovskite layer. The devices architecture is a standard, mesoporous, n-i-p PSCs with a triple cation active layer. After the preparation of c-TiO_2 (as discussed in the previous section) a m-TiO_2 layer was deposited by spin coating (at 2000 rpm for 20 s) a dispersion of TiO_2 paste (Dyesol 30 NR-D) in ethanol (a sintering process at 500 °C was performed for 20 minutes). The triple cation solution was prepared by mixing FAI (1.04 M), MABr (0.15 M), $PbBr_2$ (0.15 M), PbI_2 (1.19 M) and CsI (0.1 M) in a N,N-dimethylformamide:DMSO = 1:4 solvents volume ratio. The lead excess was used for two reasons: its positive influence on reducing defects in the perovskite film and for reacting with the organic salts used for the formation of 3D/2D interfaces.[77] This solution was spin-coated, in a nitrogen glove box, at 1000 rpm for 10 s and sequentially at 4000 rpm for 30 s. After 15 s from the beginning of the second step, 100 µL of chlorobenzene were poured on the substrates and the resulting films were annealed at 100 °C for 1 h. The 3D/2D interface was prepared by spin coating, at 4000 rpm for 20 s, 100 µL of a BAI isopropanol solution (12 mg mL^{-1}). A layer of 2D perovskite was formed on top of the triple cation layer, giving rise to a 3D/2D structure (as discussed in the previous section, with particular emphasis on the work of ref.[77]), herein named 3D/2D. The devices prepared by using 2D materials dispersions, were produced exactly in the same way as for 3D/2D interfaces, with the exception that the BAI organic salt was mixed with MoS_2 or with WS_2 flakes. Hereafter, these PSCs are named 3D/2D+MoS_2 and 3D/2D+WS_2, respectively (**figure 13a** shows the architecture of the discussed PSCs). After this, spiro-OMeTAD and Au were deposited onto the 3D/2D layer, as discussed in the previous section.

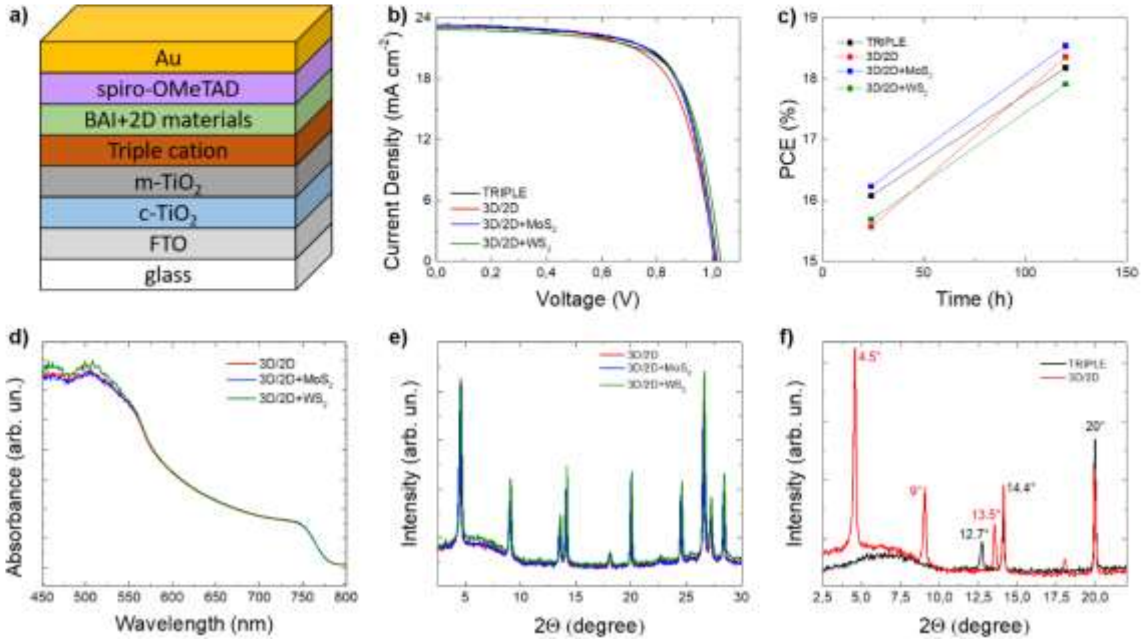

Figure 13: 3D/2D PSCs with MoS$_2$ or WS$_2$. (a) Schematic representation of the devices architecture. (b) J-V curves of the best performing devices. (c) Time evolution of the best devices PCEs. (d, e) UV-Vis absorption (d) and XRD (e) spectra of all the discussed 3D/2D devices configurations. (f) Comparison of the low angle diffraction peaks of TRIPLE and 3D/2D samples.

The aim of this study is to check if the presence of 2D materials can affect the orientation of the 2D perovskite layer and/or improve the hole extraction properties and stability of the resulting devices. **Table 2** reports the average performance values for the investigated PSCs: TRIPLE, 3D/2D, 3D/2D+MoS$_2$ and 3D/2D+WS$_2$ measured the day after their production.

	TRIPLE	3D/2D	3D/2D+MoS$_2$	3D/2D+WS$_2$
J_{SC} (mA cm^{-2})	23.16 ± 0.04	23.13 ± 0.14	22.89 ± 0.36	22.78 ± 0.08
V_{OC} (V)	1.00 ± 0.01	0.98 ± 0.01	1.00 ± 0.01	1.01 ± 0.02
FF (%)	69.60 ± 0.90	66.62 ± 0.10	67.00 ± 1.90	67.84 ± 2.00
PCE (%)	16.18 ± 0.17	15.20 ± 0.34	15.31 ± 0.65	15.64 ± 0.44
Best PCE (%)	16.38	15.57	16.23	16.13

Table 2: Average performance parameters values of TRIPLE, 3D/2D, 3D/2D+MoS$_2$ and 3D/2D+WS$_2$ devices.

From these results, it is evident that the presence of 2D materials flakes gives rise to improved PCE compared to the pure 3D/2D case as consequence of the increase of both V_{oc} and FF. The J-V curves of the best performing devices are shown in **figure 13b**. After these first measurements, the devices were stored in an Ar-filled dry box (in dark conditions) and measured again after 5 days. All the discussed devices showed an increase in their performances, as can be seen in **figure 13c**. The best PSCs, so far, is the 3D/2D+MoS_2, however more measurements are needed to check the aging effects and to understand the processes that can cause these trends. Even for this case, UV-Vis absorption and XRD spectra were measured, to assess the effects of the 2D materials flakes on the optical and structural properties of these perovskites. The samples were prepared on top of the device architecture used in the PSCs. **Figure 13d,e** report these results, confirming that the presence of MoS_2 or WS_2 flakes do not alter the absorbance and structure of the 3D/2D material (all the trends are equal to the 3D/2D reference). The formation of the 3D/2D interface can be demonstrated by checking the low angle diffraction peaks of the TRIPLE and 3D/2D samples (reported in **figure 13f**). In fact, in the TRIPLE case only three main peaks are observed: ~12.7° due to the excess of PbI_2 that is used in the precursor solution; ~14.4° and ~20° ascribed to the formation of the α-phase of $FAPbI_3$.[77] In the 3D/2D spectrum the main peaks are at ~4.5°, ~9° and ~13.5° which are in agreement with the XRD peaks observed for $(BA)_2(MA)Pb_2I_7$ (*i.e.*, for n=2 quasi-2D perovskites).[91] The disappearance of the 12.7° peak is due to the fact that the excess PbI_2 reacts with the spin-coated BAI organic salt, leading to the formation of the layered perovskite interface.[77]

CONCLUSIONS

The results showed and discussed in this chapter are still preliminary and many other characterizations are needed for a thorough understanding of the role of 2D materials in these kind of PSCs. However, it seems clear that the presence of MoS_2 or WS_2 positively influence the performances of the studied devices, confirming already existing literature results for the case of 3D perovskite active layers.

In particular, 2D materials interlayers in quasi 2D PSCs can lead to very stable and efficient SCs. Moreover, the mixture of 2D materials flakes with the organic salts needed for the preparation of the 3D/2D interfaces, can be an interesting way to induce the preferential vertical-growth of the low-dimensional perovskite.

The following weeks will be fundamental to show if these strategies will be successful and, in case of positive outcomes, these will be the first examples of the combination of low dimensional perovskites with 2D materials (to the best of our knowledge).

EXPERIMENTAL SECTION

CHARACTERIZATION OF 2D MATERIALS DISPERSIONS

Raman characterization was carried out with a Renishaw microRaman invia 1000 using a 50× objective (numerical aperture of 0.75), with an excitation wavelength of 514.5 nm and an incident power on the samples of 5 mW. The samples were prepared by drop casting the 2D materials dispersions onto a Si wafer covered with 300 nm thermally grown SiO_2 (LDB Technologies Ltd.). For each sample, 50 spectra were collected. OriginPro 2016 was used to perform the deconvolution and statistics.

Transmission electron microscopy images were taken with a JEM 1011 (JEOL) TEM (thermionic W filament), operating at 100 kV. Morphological and statistical analysis was carried out by using ImageJ software (NIH)[92] and OriginPro 9.1 software (OriginLab)[93], respectively. The samples for the TEM measurements were prepared by drop casting the dispersions of 2D materials onto ultrathin C-film on holey carbon 400 mesh Cu grids (Ted Pella Inc.). The grids were stored under vacuum at room temperature to remove the solvent residues.

A NanoWizard III AFM system (JPK Instruments, Berlin) in intermittent contact mode was used for the AFM measurements. PPP-NCHR cantilevers (Nanosensors, USA) with a nominal tip diameter of 10 nm and a drive frequency of ~320 kHz were used. AFM images were collected with a working set point above 70% of the free oscillation amplitude and a scan rate of 0.7 Hz. The images were collected on an area of 5×5 μm^2 and have a resolution of 512×512 pixels and the corresponding height profiles were analysed with the JPK Data Processing software (JPK Instruments, Germany). A statistical analysis on 90 flakes was carried out on both sets of measurements and the data fitted with a lognormal distribution, which is an established statistic function used for fragmented systems.[94] The statistical analysis was carried out by using Origin 9.1 software. The AFM characterization was performed on drop-casted dispersions of 2D materials onto freshly-cleaved mica sheets (G250-1, Agar Scientific Ltd., Essex, U.K.) and dried under vacuum.

CHARACTERIZATION OF PEROVSKITE LAYERS

The perovskite optical and structural properties were assessed by means of UV-VIS absorption and X- ray diffraction (XRD) respectively. The UV-VIS absorption spectra were measured with a PerkinElmer Lambda 950S spectrometer, in the range 800-350 nm. The XRD measurements were performed using Bruker D8 Advance diffractometer from 2θ = 2° to 51°.

POWER CONVERSION EFFICIENCY MEASUREMENTS

Photovoltaic performances were measured with a commercial solar simulator (Oriel, 450 W, Xenon, AAA class) at 1 sun (*i.e.*, 100 mW cm^{-2}), after performing a calibration with a Si reference cell (KG5, Newport equipped with an IR-cutoff filter). The J–V curves were measured by using a voltage scan rate of 50 mV s^{-1} on an active area of 0.16 cm^{-2}.

REFERENCES

1. Perez, R. & Perez, M. A Fundamental Look At Supply Side Energy Reserves For The Planet. *Int. Energy Agency SHC Program. Sol. Updat.* (2015).
2. Perez, R. & Perez, M. A Fundamental Look At Supply Side Energy Reserves For The Planet. *IEA-SHCP-Newsletter* **50**, (2009).
3. Jager, K. *et al. Solar Energy Fundamentals, Technology and Systems*. (UIT Cambridge, 2014). doi:10.1007/SpringerReference_29746
4. Grancini, G. A new era for solar energy: hybrid perovskite rocks. *Photoniques* 24–31 (2019). doi:10.1051/photon/2019s424
5. Ansari, M. I. H., Qurashi, A. & Nazeeruddin, M. K. Frontiers, opportunities, and challenges in perovskite solar cells: A critical review. *J. Photochem. Photobiol. C Photochem. Rev.* **35**, 1–24 (2018).
6. Chapin, D. M., Fuller, C. S. & Pearson, G. L. A new silicon p-n junction photocell for converting solar radiation into electrical power [3]. *J. Appl. Phys.* **25**, 676 (1954).
7. Luceño-Sánchez, J. A., Díez-Pascual, A. M. & Capilla, R. P. Materials for photovoltaics: State of art and recent

developments. *Int. J. Mol. Sci.* **20**, 976 (2019).

8. Nayak, P. K., Mahesh, S., Snaith, H. J. & Cahen, D. Photovoltaic solar cell technologies: analysing the state of the art. *Nat. Rev. Mater.* **4**, 269–285 (2019).
9. National Renewable Energy Laboratory. Available at: https://www.nrel.gov/pv/cell-efficiency.html.
10. Binder, H. *Lexikon der chemischen Elemente*. (Hirzel Verlag, 1999).
11. Tanaka, A. Toxicity of indium arsenide, gallium arsenide, and aluminium gallium arsenide. *Toxicol. Appl. Pharmacol.* **198**, 405–411 (2004).
12. Shockley, W. & Queisser, H. J. Detailed balance limit of efficiency of p-n junction solar cells. *J. Appl. Phys.* **32**, 510–519 (1961).
13. Hardin, B. E., Snaith, H. J. & McGehee, M. D. The renaissance of dye-sensitized solar cells. *Nat. Photonics* **6**, 162–169 (2012).
14. Nazeeruddin, M. K., Baranoff, E. & Grätzel, M. Dye-sensitized solar cells: A brief overview. *Sol. Energy* **85**, 1172–1178 (2011).
15. Snaith, H. J. Perovskites: The emergence of a new era for low-cost, high-efficiency solar cells. *J. Phys. Chem. Lett.* **4**, 3623–3630 (2013).
16. Kamat, P. V. Quantum dot solar cells. The next big thing in photovoltaics. *J. Phys. Chem. Lett.* **4**, 908–918 (2013).
17. Kojima, A., Teshima, K., Shirai, Y. & Miyasaka, T. Organometal halide perovskites as visible-light sensitizers for photovoltaic cells. *J. Am. Chem. Soc.* **131**, 6050 (2009).
18. Im, J. H., Lee, C. R., Lee, J. W., Park, S. W. & Park, N. G. 6.5% efficient perovskite quantum-dot-sensitized solar cell. *Nanoscale* **3**, 4088–4093 (2011).
19. Gao, P. *et al.* Organohalide lead perovskites for photovoltaic applications. *Energy Environ. Sci.* **7**, 2448–2463 (2014).
20. *Unconventional Thin Film Photovoltaics*. (Royal Society of Chemistry, 2016). doi:10.1039/9781782624066
21. Kim, H. S. *et al.* Lead iodide perovskite sensitized all-solid-state submicron thin film mesoscopic solar cell with efficiency

exceeding 9%. *Sci. Rep.* **2**, 591 (2012).

22. Lee, M. M., Teuscher, J., Miyasaka, T., Murakami, T. N. & Snaith, H. J. Efficient hybrid solar cells based on meso-superstructured organometal halide perovskites. *Science (80-.).* **338**, 643–647 (2012).

23. Correa-Baena, J. P. *et al.* The rapid evolution of highly efficient perovskite solar cells. *Energy Environ. Sci.* **10**, 710–727 (2017).

24. Correa-Baena, J. P. *et al.* Promises and challenges of perovskite solar cells. *Science (80-.).* **358**, 739–744 (2017).

25. Saliba, M. *et al.* How to Make over 20% Efficient Perovskite Solar Cells in Regular (n-i-p) and Inverted (p-i-n) Architectures. *Chem. Mater.* **30**, 4193–4201 (2018).

26. Green, M. A. & Ho-Baillie, A. Perovskite Solar Cells: The Birth of a New Era in Photovoltaics. *ACS Energy Lett.* **2**, 822–830 (2017).

27. Grätzel, M. The rise of highly efficient and stable perovskite solar cells. *Acc. Chem. Res.* **50**, 487–491 (2017).

28. De Graef, M. & Mc Henry, M. *Structure of materials: an introduction to crystallography, diffraction and symmetry*. (Cambridge University Press, 2007).

29. Herz, L. M. Charge-Carrier Dynamics in Organic-Inorganic Metal Halide Perovskites. *Annu. Rev. Phys. Chem.* **67**, 65–89 (2016).

30. Goldschmidt, V. M. Die Gesetze der Krystallochemie. *Naturwissenschaften* **21**, 477–485 (1926).

31. Huang, J., Yuan, Y., Shao, Y. & Yan, Y. Understanding the physical properties of hybrid perovskites for photovoltaic applications. *Nat. Rev. Mater.* **2**, 17042 (2017).

32. Jensen, N., Hausner, R. M., Bergmann, R. B., Werner, J. H. & Rau, U. Optimization and characterization of amorphous/crystalline silicon heterojunction solar cells. *Prog. Photovoltaics Res. Appl.* **10**, 1–14 (2002).

33. Xiao, Z. *et al.* Solvent Annealing of Perovskite-Induced Crystal Growth for Photovoltaic-Device Efficiency Enhancement. *Adv. Mater.* **26**, 6503–6509 (2014).

34. Giebink, N. C., Wiederrecht, G. P., Wasielewski, M. R. &

Forrest, S. R. Thermodynamic efficiency limit of excitonic solar cells. *Phys. Rev. B - Condens. Matter Mater. Phys.* **83**, 195326 (2011).

35. Fehrenbach, G. W., Schäfer, W. & Ulbrich, R. G. Excitonic versus plasma screening in highly excited gallium arsenide. *J. Lumin.* **30**, 154 (1985).
36. Shaklee, K. L. & Nahory, R. E. Valley-Orbit Splitting of Free Excitons? the Absorption Edge of Si. *Phys. Rev. Lett.* **24**, 942 (1970).
37. D'Innocenzo, V. *et al.* Excitons versus free charges in organo-lead tri-halide perovskites. *Nat. Commun.* **5**, 3586 (2014).
38. Dong, Q. *et al.* Electron-hole diffusion lengths > 175 μm in solution-grown CH 3 NH 3 PbI 3 single crystals. *Science (80-.).* **347**, 967–970 (2015).
39. Nah, S. *et al.* Spatially segregated free-carrier and exciton populations in individual lead halide perovskite grains. *Nat. Photonics* **11**, 285–288 (2017).
40. Johnston, M. B. & Herz, L. M. Hybrid Perovskites for Photovoltaics: Charge-Carrier Recombination, Diffusion, and Radiative Efficiencies. *Acc. Chem. Res.* **49**, 146–154 (2016).
41. Langevin, P. The recombination and mobilities of ions in gases. *Ann. Chim. Phys.* **28**, 433–530 (1903).
42. Wehrenfennig, C., Liu, M., Snaith, H. J., Johnston, M. B. & Herz, L. M. Charge-carrier dynamics in vapour-deposited films of the organolead halide perovskite CH3NH3PbI3-xClx. *Energy Environ. Sci.* **7**, 2269–2275 (2014).
43. Wehrenfennig, C., Eperon, G. E., Johnston, M. B., Snaith, H. J. & Herz, L. M. High charge carrier mobilities and lifetimes in organolead trihalide perovskites. *Adv. Mater.* **26**, 1584–1589 (2014).
44. Pivrikas, A. *et al.* Bimolecular recombination coefficient as a sensitive testing parameter for low-mobility solar-cell materials. *Phys. Rev. Lett.* **94**, 176806 (2005).
45. Adriaenssens, G. J. & Arkhipov, V. I. Non-Langevin recombination in disordered materials with random potential distributions. *Solid State Commun.* **103**, 541–543 (1997).
46. Leblebici, S. Y. *et al.* Facet-dependent photovoltaic efficiency

variations in single grains of hybrid halide perovskite. *Nat. Energy* **1**, 16093 (2016).

47. Saliba, M., Correa-Baena, J. P., Grätzel, M., Hagfeldt, A. & Abate, A. Perovskite Solar Cells: From the Atomic Level to Film Quality and Device Performance. *Angew. Chemie - Int. Ed.* **57**, 2554–2569 (2018).
48. Hoke, E. T. *et al.* Reversible photo-induced trap formation in mixed-halide hybrid perovskites for photovoltaics. *Chem. Sci.* **6**, 613–617 (2015).
49. Yuan, Y. & Huang, J. Ion Migration in Organometal Trihalide Perovskite and Its Impact on Photovoltaic Efficiency and Stability. *Acc. Chem. Res.* **49**, 286–293 (2016).
50. Xing, J. *et al.* Ultrafast ion migration in hybrid perovskite polycrystalline thin films under light and suppression in single crystals. *Phys. Chem. Chem. Phys.* **18**, 30484–30490 (2016).
51. Saliba, M. *et al.* Incorporation of rubidium cations into perovskite solar cells improves photovoltaic performance. *Science (80-.).* **354**, 206–209 (2016).
52. Voznyy, O. Black and Stable: A Path to All-Inorganic Halide Perovskite Solar Cells. *Joule* **2**, 1215–1216 (2018).
53. Leijtens, T. *et al.* Towards enabling stable lead halide perovskite solar cells; Interplay between structural, environmental, and thermal stability. *J. Mater. Chem. A* **5**, 11483 (2017).
54. Grancini, G. & Nazeeruddin, M. K. Dimensional tailoring of hybrid perovskites for photovoltaics. *Nat. Rev. Mater.* **1**, (2019).
55. Glazer, A. M. The classification of tilted octahedra in perovskites. *Acta Crystallogr. Sect. B Struct. Crystallogr. Cryst. Chem.* **28**, 3384–3391 (1972).
56. Quarti, C. *et al.* Structural and optical properties of methylammonium lead iodide across the tetragonal to cubic phase transition: Implications for perovskite solar cells. *Energy Environ. Sci.* **9**, 155–163 (2016).
57. Milot, R. L., Eperon, G. E., Snaith, H. J., Johnston, M. B. & Herz, L. M. Temperature-Dependent Charge-Carrier Dynamics in CH3NH3PbI3 Perovskite Thin Films. *Adv. Funct. Mater.* **25**, 6218–6227 (2015).

58. Conings, B. *et al.* Intrinsic Thermal Instability of Methylammonium Lead Trihalide Perovskite. *Adv. Energy Mater.* **5**, 1500477 (2015).

59. Beal, R. E. *et al.* Cesium lead halide perovskites with improved stability for tandem solar cells. *J. Phys. Chem. Lett.* **7**, 746–751 (2016).

60. Sutton, R. J. *et al.* Bandgap-Tunable Cesium Lead Halide Perovskites with High Thermal Stability for Efficient Solar Cells. *Adv. Energy Mater.* **6**, 1502458 (2016).

61. McMeekin, D. P. *et al.* A mixed-cation lead mixed-halide perovskite absorber for tandem solar cells. *Science (80-.).* **351**, 151–155 (2016).

62. Aristidou, N. *et al.* The Role of Oxygen in the Degradation of Methylammonium Lead Trihalide Perovskite Photoactive Layers. *Angew. Chemie - Int. Ed.* **54**, 8208–8212 (2015).

63. Wang, Z. *et al.* Efficient and Air-Stable Mixed-Cation Lead Mixed-Halide Perovskite Solar Cells with n-Doped Organic Electron Extraction Layers. *Adv. Mater.* **29**, 1604186 (2017).

64. Leijtens, T. *et al.* Overcoming ultraviolet light instability of sensitized TiO2 with meso-superstructured organometal tri-halide perovskite solar cells. *Nat. Commun.* **4**, 2885 (2013).

65. Domanski, K. *et al.* Not All That Glitters Is Gold: Metal-Migration-Induced Degradation in Perovskite Solar Cells. *ACS Nano* **10**, 6306–6314 (2016).

66. Bush, K. A. *et al.* Thermal and Environmental Stability of Semi-Transparent Perovskite Solar Cells for Tandems Enabled by a Solution-Processed Nanoparticle Buffer Layer and Sputtered ITO Electrode. *Adv. Mater.* **28**, 3937–3943 (2016).

67. Bush, K. A. *et al.* 23.6%-efficient monolithic perovskite/silicon tandem solar cells with improved stability. *Nat. Energy* **2**, 17009 (2017).

68. Yan, J., Qiu, W., Wu, G., Heremans, P. & Chen, H. Recent progress in 2D/quasi-2D layered metal halide perovskites for solar cells. *J. Mater. Chem. A* **6**, 11063 (2018).

69. Mao, L. *et al.* Hybrid Dion-Jacobson 2D Lead Iodide Perovskites. *J. Am. Chem. Soc.* **140**, 3775–3783 (2018).

70. Mitzi, D. B. Synthesis, structure, and properties of organic-

inorganic perovskites and related materials. *Prog. Inorg. Chem.* **48**, 1–121 (2007).

71. Ahmad, S. *et al.* Dion-Jacobson Phase 2D Layered Perovskites for Solar Cells with Ultrahigh Stability. *Joule* **3**, 794–806 (2019).

72. Smith, I. C., Hoke, E. T., Solis-Ibarra, D., McGehee, M. D. & Karunadasa, H. I. A Layered Hybrid Perovskite Solar-Cell Absorber with Enhanced Moisture Stability. *Angew. Chemie - Int. Ed.* **53**, 11232–11235 (2014).

73. Cao, D. H., Stoumpos, C. C., Farha, O. K., Hupp, J. T. & Kanatzidis, M. G. 2D Homologous Perovskites as Light-Absorbing Materials for Solar Cell Applications. *J. Am. Chem. Soc.* **137**, 7843–7850 (2015).

74. Chen, A. Z. *et al.* Origin of vertical orientation in two-dimensional metal halide perovskites and its effect on photovoltaic performance. *Nat. Commun.* **9**, 1336 (2018).

75. Chen, Y. *et al.* Tailoring Organic Cation of 2D Air-Stable Organometal Halide Perovskites for Highly Efficient Planar Solar Cells. *Adv. Energy Mater.* **7**, 1700162 (2017).

76. Quan, L. N. *et al.* Ligand-Stabilized Reduced-Dimensionality Perovskites. *J. Am. Chem. Soc.* **138**, 2649–2655 (2016).

77. Cho, K. T. *et al.* Selective growth of layered perovskites for stable and efficient photovoltaics. *Energy Environ. Sci.* **11**, 952–959 (2018).

78. Grancini, G. *et al.* One-Year stable perovskite solar cells by 2D/3D interface engineering. *Nat. Commun.* **8**, 15684 (2017).

79. Kouroupis-Agalou, K. *et al.* Fragmentation and exfoliation of 2-dimensional materials: a statistical approach. *Nanoscale* **6**, 5926–5933 (2014).

80. Saito, R., Tatsumi, Y., Huang, S., Ling, X. & Dresselhaus, M. S. Raman spectroscopy of transition metal dichalcogenides. *J. Phys. Condens. Matter* **28**, 353002 (2016).

81. Lee, C. *et al.* Anomalous lattice vibrations of single- and few-layer MoS2. *ACS Nano* **4**, 2695–2700 (2010).

82. Acik, M. & Darling, S. B. Graphene in perovskite solar cells: Device design, characterization and implementation. *J. Mater. Chem. A* **4**, 6185–6235 (2016).

83. Kakavelakis, G., Kymakis, E. & Petridis, K. 2D Materials

Beyond Graphene for Metal Halide Perovskite Solar Cells. *Adv. Mater. Interfaces* **5**, 1800339 (2018).

84. Petridis, C., Kakavelakis, G. & Kymakis, E. Renaissance of graphene-related materials in photovoltaics due to the emergence of metal halide perovskite solar cells. *Energy Environ. Sci.* **11**, 1030–1061 (2018).

85. Capasso, A. *et al.* Few-Layer MoS2 Flakes as Active Buffer Layer for Stable Perovskite Solar Cells. *Adv. Energy Mater.* **6**, 1600920 (2016).

86. Agresti, A. *et al.* Two-dimensional (2D) Material Interface Engineering for Efficient Perovskite Large-area Modules. *ACS Energy Lett.* **4**, 1862–1871 (2019).

87. Najafi, L. *et al.* MoS2 Quantum Dot/Graphene Hybrids for Advanced Interface Engineering of a CH3NH3PbI3 Perovskite Solar Cell with an Efficiency of over 20%. *ACS Nano* **12**, 10736–10754 (2018).

88. Kakavelakis, G. *et al.* Extending the Continuous Operating Lifetime of Perovskite Solar Cells with a Molybdenum Disulfide Hole Extraction Interlayer. *Adv. Energy Mater.* **8**, 1702287 (2018).

89. Duan, X., Wang, C., Pan, A., Yu, R. & Duan, X. Two-dimensional transition metal dichalcogenides as atomically thin semiconductors: Opportunities and challenges. *Chem. Soc. Rev.* **44**, 8859–8876 (2015).

90. Yuan, M. *et al.* Perovskite energy funnels for efficient light-emitting diodes. *Nat. Nanotechnol.* **11**, 872 (2016).

91. Stoumpos, C. C. *et al.* Ruddlesden-Popper Hybrid Lead Iodide Perovskite 2D Homologous Semiconductors. *Chem. Mater.* **28**, 2852–2867 (2016).

92. Schneider, C. A., Rasband, W. S. & Eliceiri, K. W. NIH Image to ImageJ: 25 years of image analysis. *Nat. Methods* **9**, 671 (2012).

93. Seifert, E. OriginPro 9.1: Scientific Data Analysis and Graphing Software—Software Review. *J. Chem. Inf. Model.* **54**, 1552 (2014).

94. Kouroupis-Agalou, K. *et al.* Fragmentation and exfoliation of 2-dimensional materials: A statistical approach. *Nanoscale* **6**, 5926–5933 (2014).

CONCLUSIONS

The research work presented in this thesis shows that the properties of 2D materials can be exploited for the design of high-performance devices for energy storage and generation.

We demonstrated that the use of single-/few-layer graphene (SLG/FLG) flakes in mesoporous activated carbon (AC) films positively impact the performance of commercial-like electrochemical double layer capacitors (EDLCs) (*i.e.*, EDLCs with high active material mass loading of ~10 mg cm^{-2}). In particular, our results show that the ions of 1 M tetraethylammonium tetrafluoroborate in propylene carbonate (an electrolyte used in commercially available EDLCs) efficiently slide over the SLG/FLG flakes. Consequently, the incorporation of SLG/FLG into high specific surface area AC-based nanoporous structures enhances the electrochemical performances of EDLCs. This work shows that efficient ion transport depends on the nanotribological properties of electrolytes over electrodes surfaces, highlighting that interfaces phenomena and studies must be considered for the design of novel concept for high performance EDLCs.

Moreover, we showed that wet-jet milling produced graphene flakes (WJM-G) can be used for the fabrication of high-areal performance electrodes for EDLCs. When mixed with commercial single-/double-walled carbon nanotubes (SDWCNTs) to avoid flakes restacking, the hybrid WJM-G/SDWCNTs electrodes show areal capacitance, energy and power that are comparable with literature results. The main advantages of our devices are: the scalability of the wet-jet milling production of graphene flakes, the ease and scalable fabrication of our EDLCs (*i.e.*, by means of facile vacuum filtration of the WJM-G/SDWCNTs dispersions), the possibility to achieve high mass loading (up to ~30.4 mg cm^{-2}, with consequently higher performances) and the possibility to produce EDLCs with quasi-solid-electrolytes. These results show that the large scale production of our devices is feasible and can find practical applications in the field of wearable electronics.

Finally, we used dispersions of MoS_2 and WS_2 flakes (produced by liquid phase exfoliation) in low dimensional perovskites for photovoltaic applications. In low dimensional perovskites the structure is changed, with respect to the 3D case, by the presence of bulky organic cations that separates the inorganic planes. These kind of materials are more stable than the 3D counterparts (*i.e.*, they are more tolerant to oxygen and moisture), but the performances of the resulting devices are lower (always with respect to the 3D case). With the aim to improve the performances of low dimensional perovskites, we implemented 2D materials in this kind of devices. These results are still preliminary and more characterization are needed (at the time of this thesis submission), yet our first findings show that the presence of MoS_2 or WS_2 positively affects the solar cells performances.

In conclusion, the proper exploitation of 2D materials properties can boost the performances of both energy storage and generation devices. Moreover, the introduction of scalable techniques for the production of these materials (like the wet-jet milling) is paving the way for a real large-scale spreading of these disruptive technologies. However, there is still the need for a thorough understanding of the physical properties of these systems, as we showed for the case of the nano-tribological properties of graphene flakes. For this reason, I will devote the next years of my career to get more insight in this fascinating and promising scientific fields.

PUBLICATIONS LIST

- **“Ion sliding” on graphene: novel concept to boost supercapacitor performance**, S. Bellani, B. Martin-Garcia, R. Oropesa-Nuñez, **V. Romano**, L. Najafi, C. Demirci, M. Prato, A. E. Del Rio Castillo, L. Marasco, E. Mantero, G. D’Angelo, F. Bonaccorso, *Nanoscale Horizons (2019).*
- **Flexible graphene-carbon nanotube electrochemical double layer capacitors with ultrahigh areal performance**, **V. Romano**, B. Martín-García, S. Bellani, L. Marasco, J. K. Panda, R. Oropesa-Nuñez, L. Najafi, A. E. Del Rio Castillo, M. Prato, E. Mantero, G. D’Angelo, F. Bonaccorso, *ChemPlusChem (2019), 84.*
- **Extending the colloidal transition metal dichalcogenide library to ReS_2 nanosheets for application in gas sensing and electrocatalysis**, B. Martín-García, D. Spirito, S. Bellani, M. Prato, **V. Romano**, A. Polovitsyn, L. Najafi, A. Ansaldo, G. D’Angelo, V. Pellegrini, R. Krahne, I. Moreels, F. Bonaccorso *(submitted).*
- **Vibrational collapse of boroxol rings in compacted B_2O_3 glasses: a study of Raman scattering and low temperature specific heat,** G. Carini Jr, G. Carini, G. D'Angelo, M. Federico, **V. Romano**, *Materials Research Express (2018), 5, 055202.*
- **Boroxol ring modification driven by plastic deformations of compacted B_2O_3 glasses**, G. Carini Jr, G. Carini, G. D'Angelo, M. Federico, **V. Romano**, *Journal of Non-Crystalline Solids (2018), 492, 102.*
- **Raman investigation of laser-induced structural defects of graphite oxide films**, **V. Romano**, L. Torrisi, M. Cutroneo, V. Havranek, G. D'Angelo, *EPJ Web of Conferences (2018), 167, 04011.*
- **Atomic packing and low energy vibrations in B_2O_3glasses, compacted under GPa pressures**, G. Carini Jr, G. Carini, G. D'Angelo, M. Federico, **V. Romano**, *AAPP Atti della Accademia Peloritana dei Pericolanti, Classe di Scienze Fisiche, Matematiche e Naturali (2017), 95, 3.*

CONFERENCE CONTRIBUTIONS

- **Towards industrial production of hybrid graphene/carbon nanotubes supercapacitors with high areal performance**, **V. Romano**, S. Bellani, B. Martin-Garcia, L. Najafi, A. E. Del Rio Castillo, M. Prato, G. D'Angelo, F. Bonaccorso, *GrapheneMalaysia2018,* Ministry of International Trade and Industry, Kuala Lumpur, Malaysia, 29-30 October 2018 (oral presentation).
- **An industrial scalable approach for graphene/carbon nanotubes hybrid flexible supercapacitors**, **V. Romano**, S. Bellani, B. Martin-Garcia, L. Najafi, A. E. Del Rio Castillo, M. Prato, G. D'Angelo, F. Bonaccorso, *RPGR2018 (Recent Progress in Graphene & 2D Materials Research 2018),* Gran Bravo Guilin Hotel, Guilin, China, 22-25 October 2018 (oral presentation).
- **Graphene and carbon-nanotubes for advanced flexible supercapacitor**, **V. Romano**, S. Bellani, B. Martin-Garcia, L. Najafi, A. E. Del Rio Castillo, M. Prato, G. D'Angelo, F. Bonaccorso, *Graphene2018,* Maritim Hotel, Dresden, Germany, 26-29 June 2018 (oral presentation).
- **Low frequency Raman scattering and low temperature heat capacity of densified B2O3 glasses**, G. Carini Jr, G. Carini, G. D'Angelo, M. Federico, **V. Romano**, *Ninth International Conference on Borate Glasses, Crystals and Melts* St. Anne's College, Oxford, United Kingdom, 24 - 26 July 2017 (oral presentation).
- **Raman investigation of laser-induced structural defects of graphene oxide**, **V. Romano**, L. Torrisi, M. Cutroneo, V. Havranek, G. D'Angelo *Plasma Physics by Laser and Applications - PPLA2017* University of Messina, Italy, 5 - 7 July, 2017 (poster presentation).